Hubbard Model Approach to X-ray Spectroscopy

Towfiq Ahmed

A dissertation
submitted in partial fulfillment of the
requirements for the degree of

Doctor of Philosophy

University of Washington

2012

Reading Committee:

John J. Rehr, Chair

Gerald T. Seidler

Anton Andreev

Program Authorized to Offer Degree:
UW Department of Physics

University of Washington

Abstract

Hubbard Model Approach to X-ray Spectroscopy

Towfiq Ahmed

Chair of the Supervisory Committee:
Professor John J. Rehr
Department of Physics

We have implemented a Hubbard model based first-principles approach for real-space calculations of x-ray spectroscopy, which allows one to study excited state electronic structure of correlated systems. Theoretical understanding of many electronic features in d and f electron systems remains beyond the scope of conventional density functional theory (DFT). In this work our main effort is to go beyond the local density approximation (LDA) by incorporating the Hubbard model within the real-space multiple-scattering Green's function (RSGF) formalism. Historically, the first theoretical description of correlated systems was published by Sir Neville Mott and others in 1937. They realized that the insulating gap and antiferromagnetism in the transition metal oxides are mainly caused by the strong on-site Coulomb interaction of the localized unfilled $3d$ orbitals. Even with the recent progress of first principles methods (e.g. DFT) and model Hamiltonian approaches (e.g., Hubbard-Anderson model), the electronic description of many of these systems remains a non-trivial combination of both.

X-ray absorption near edge spectra (XANES) and x-ray emission spectra (XES) are very powerful spectroscopic probes for many electronic features near Fermi energy (E_F), which are caused by the on-site Coulomb interaction of localized electrons. In this work we focus on three different cases of many-body effects due to the interaction of localized d electrons. Here, for the first time, we have applied the Hubbard model in the real-space multiple scattering (RSGF) formalism for the calculation of x-ray spectra of Mott insulators (e.g., NiO and MnO). Secondly, we have implemented in our RSGF approach a doping dependent self-energy that was constructed from a single-band Hubbard

model for the over doped high-T_c cuprate $La_{2-x}Sr_xCuO_4$. Finally our RSGF calculation of XANES is calculated with the spectral function from Lee and Hedin's charge transfer satellite model. For all these cases our calculated x-ray spectra yield reasonable agreement with experiment. The above work has been implemented as an extension into the FEFF9 code, and we have also included notes for the new and modified key features of this development.

Aside from the x-ray spectroscopy of correlated systems, we also present our calculation of the ground state local electronic structure of DNA nucleotides on graphene, and the transmission currents through graphene nanopores. Our calculation and analysis provide theoretical guidelines for developing DNA sequencing techniques using scanning tunneling spectroscopy (STS) and nanopore experiment. Evolved as a secondary focus of this thesis, we have added an additional chapter discussing our calculation of DNA-graphene hybrids.

TABLE OF CONTENTS

LIST OF FIGURES

LIST OF TABLES

GLOSSARY

XAS: X-ray absorption spectrum.

XES: X-ray emission spectrum.

XANES: X-ray absorption near edge structure.

DOS: Density of states.

LDOS: L(Angular momentum) projected density of states.

RPA: Random phase approximation.

CRPA: constrained random phase approximation.

RSGF: Real-space Green's function.

MS: Multiple-scattering.

FMS: Full multiple-scattering.

LDA: Local density approximation.

LSDA: Local spin density approximation.

DFT: Density functional theory.

ACKNOWLEDGMENTS

For the completion of this thesis, I am indebted to many people including my committee members, my friends, my family members and my wife.

First I would like to express my deepest gratitude to my advisor, Professor John J. Rehr, for his excellent guidance, caring, patience, and providing me with an excellent atmosphere for doing research. I would then give special thanks to Dr. Joshua Kas for guiding my research for the past several yeras and helping me to develop my background in various techniques of condensed matter physics. I learnt lot from our countless hours of physics discussion. Many thanks to Dr. Alexander Balatsky from LANL for his constant support and guidence in much of the work in my thesis. I would also like to thank all my committee members including Dr. Gerald T. Seidler, Dr. M.P. Anantram, Dr. Marcel denNijs, Dr. Alejandro Garcia, annd particularly Dr. Anton Andreev for willing to participate in my final defense committee at the last moment.

I would like to thank Prof. Arun Bansil from Northeastern University for his insightful guidence and for giving me the opportunity to collaborate with his Group. Special thanks will go to Dr. Tanmoy Das, who as a good friend, was always willing to help and give his best suggestions. Thank you Dr. Fernando Vila and John Vinson for helping me with stimulating discussion whenever I had trouble with various computation and physics problems. It would have been a lonely office without you. My gratitude goes to all the other members of Rehr Group for their friendly support and help. I would also like to thank my mother, three elder sisters, and elder brother. They were always supporting and encouraging me with their best wishes from the furthest end of the planet.

Finally, I would like to thank my wife, Mumu Mahruba Mahbub. She was always there cheering me up and stood by me through the good times and bad.

DEDICATION

I would like to dedicate this work to my mother Fahmida Hossain and to my wife Mumu Mahbub who constantly love and support me in each and every step of my life.

Chapter 1

INTRODUCTION

Research in the area of correlated systems has progressed significantly over the last thirty years. Due to the recent advances in experimental techniques and computing resources, it is now possible to study a series of exotic materials including heavy fermions, copper-based high temperature superconductors and colossal magnetoresistance. With the development of second generation synchrotron radiation, high resolution x-ray spectroscopy of these systems became possible, and plethora of exciting experimental data became available for theoretical understanding. A growing need to explain the underlying physics has driven a significant effort to develop theoretical and computational tools beyond the conventional electronic-structure codes.

There are two main ways one can study ground state properties and excitation spectra of many-electron systems. In the first approach one constructs a parameter-dependent model hamiltonian where the parameter(s) is fitted with some previously measured experimental data, and the second one is a parameter free first principle approach. The most successful of all the first-principle approaches is Density Functional Theory (DFT) within the local density approximation (LDA). Despite its enormous success in simple metals and molecular systems, the limitation of LDA is clearly visible for systems with partially filled d or f shells, e.g. transition-metal or rare-earth compounds.

There have been several attempts to improve over LDA such as self-interaction correction (SIC), GW approximation, LDA+U, dynamical mean-field theory (DMFT) etc. In the present work, a first-principles Hubbard model approach will be followed within a RSGF multiple-scattering frame work.

1.1 Historical Background

Despite its relatively recent popularity, the history of strongly correlated systems pre-dates much of the modern development of many-body quantum theory. One of the early successes of quantum mechanics was indeed the development of single particle band-structure theory which was able to

describe most of the simple metals and a handful of regular insulators. It was about the same time when interest in metal-insulator transition increased leading to the realization of a new class of materials. In 1937 de Boer and Verway [2] first pointed out the special case of NiO, a transparent non-metal which should be metallic according to the single-particle band-structure theory. It was Peierls who, for the first time, proposed the possibility of the strong Coulomb correlation as the underlying cause of the insulating phase in these systems.

In a series of seminal papers from 1935 to 1949, using a crystalline array of hydrogen-like atoms with varying lattice constant a, Sir Neville Mott was able to show and classify a class of insulators, now known as Mott insulators [3, 4]. In such systems, the screened potential around each positive charge is given by

$$V(r) = -\frac{e^2}{r}e^{qr}, \tag{1.1}$$

where the screening constant q was calculated using Thomas-Fermi model [4, 5]. In this description, the value of q was just enough to trap an electron. With varying q, all trapped electrons in the system go through a transition where all of them eventually become free. Thus a formal, yet simple metal to insulator transition was proposed for the first time. In 1951 Slater provided a description [6, 7] where the anti-ferromagnetic lattices are responsible for the split d-bands in NiO or similar systems. But such systems were later found to remain non-metallic even above Nèel temperature where the AFM ordering vanishes [4].

A next step development came from Hubbard in 1964 with a model in which the on-site Coulomb interaction was included while long-range forces are neglected [8, 9]. With large values of the lattice constant a, this model was able to explain the appearance of antiferromagnetic phases and band splitting as Slater claimed earlier.

In recent years Lars Hedin and others have shown [10, 11] that an efficient and consistent treatment of many-body effects are essential for dealing with strong-correlation phenomena. Despite the enormous success of the quasi-particle GW formalism in semiconducting systems, insulators with strong Coulomb interaction still remains a challenge.

Some of the of the most successful modern developments for ground state properties of correlated systems are the LDA+U by Anisimov *et al.* [12, 13], SIC method by Perdew *et al.* [14], and hybrid functional approach e.g. HSE functional [15]. For excitation properties, TDDFT [16]

and configuration interaction CI [17] are still limited to smaller systems. Recent development in dynamical mean field theory (DMFT) [18] seems promising although computationally expensive.

1.2 Goal of the Dissertation

Almost all efforts to integrate strong correlation effects with first principles methods end up being either computationally very expensive or parameter dependent, e.g., relying on Hubbard U and exchange J terms. Currently there are a number of ground-state electronic structure codes available that can incorporate a Hubbard model correction, but the majority of them fit the parameter U to obtain the experimental band gap. In the presence of strong electron-electron interactions, the narrow band at the Fermi energy splits into upper and lower Hubbard band and a insulating gap is formed. Thus, to understand the physics near the Fermi energy of such systems, a good description of the unoccupied states is essential.

In order to reproduce some of the signature features in the XANES and density of states (DOS) of Mott insulators, in this thesis we have implemented a rotationally invariant real-space Hubbard model on top of our real-space multiple-scattering method. This correctly accounts for the onsite strong Coulomb interaction of the localized d-orbital electrons, and our calculations show good agreement with experimentally observed features. Most of the developments presented in this thesis are within the RSGF framework of the FEFF9 program. As a quasi-particle excited state electronic-structure code, FEFF9 calculates occupied and unoccupied electronic states as well as various x-ray spectrum in the presence of the core-hole. Here also we calculate the dominant Hubbard parameter U within the scope of FEFF9 code. As the main purpose of this work, our development thus computationally reproduces, from first-principles, the electronic structure and spectral features present in the x-ray spectra of Mott-Hubbard insulators due to strong onsite Coulomb interaction of localized $3d$ electrons.

Many correlated-electron systems including the high-T_c cuprates, show doping dependent spectral features in their near edge x-ray spectra. As the doping concentration increases, the spectral features due to strong Coulomb interaction vanishes in many such systems, e.g., $Nd_{2-x}Ce_xCuO_4$ (NCCO) and $La_{2-x}Sr_xCuO_4$ (LSCO). To account for such changes in the correlation strength with varying doping concentration, a quasi-particle self-energy was originally developed by Bansil *et al.*

[19] using a single-band Hubbard model. As the next topic of this thesis, we have implemented this self-energy in our RSGF code FEFF, and calculated the doping dependent O K-edge XANES in over-doped LSCO which are in good accord with experiment.

Another interesting property of correlated systems is the many-body charge-transfer excitations. The signatures of such excitation are often present in the x-ray spectroscopy, and are generally identified as the shake-up or shake-down satellites. In this thesis we have also studied some of the satellite features present in the Cu K-edge XANES of Nd_2CuO_4 and La_2CuO_4. Following the prescription of Lee *et al.* [20], we constructed a charge transfer (CT) spectral function. Our RSGF calculation of XANES convoluted with the CT spectral function yields good agreement with the experiment by Kosugi *et al.* [21]

As a secondary interest, we have also applied our first-principles calculation of the local electronic structure using ground-state DFT and conductance using non-equilibrium Green's function (NEGF) technique for the DNA nucleotides on graphene. Our computation, although not directly connected to the problem of correlated systems, provides theoretical guidelines for scanning tunneling spectroscopy (STS) and nano-pore sequencing experiment in the ongoing effort to develop cheaper and accurate DNA fingerprinting techniques.

1.3 Overview of the Dissertation

The chapters in this thesis are organized as follows: In chapter 1 we briefly make historical remarks on some of the key developments in our understanding of strongly correlated systems. This chapter also includes the goal of this work, our key observations, and a quick review of x-ray absorption and emission spectroscopy. The discussion in chapter 2 provides a review of all the background concept and theories needed for the rest of the thesis. Starting with the real-space Green's function and multiple scattering formalism of x-ray spectroscopy, we briefly discuss some of the key features of Hubbard model and high temperature superconductivity. The discussion in chapter 3 and 4 are based on our previously published papers [22, 23]. chapter 3 discusses our rotationally invariant Hubbard model and its implementation in the real-space multiple-scattering code FEFF9. Here we also briefly discuss our method for the calculation of the Hubbard parameter U. In this chapter we show our calculation of XANES and DOS of transition metal oxides (NiO, MnO) and High

T_c cuprate (LSCO), and compare with experiment. The work presented in chapter 4 stems from a collaboration between the Rehr Group at University of Washington and the Bansil group at Northeastern University. In this chapter we discuss the key features of a doping dependent self-energy which is developed at Northeastern University. We apply this self-energy to our RSGF code FEFF9, and presented our calculation of O K-edge XANES in over-doped LSCO. chapter 6 is dedicated to our ground state calculation of DNA nucleotides on graphene and electron transport calculation through graphene nano-pores.

In chapter 7 we give concluding remarks and briefly discuss future directions. Finally we give a detailed description of our computer program in appendix-A that has been developed and added to FEFF9 as an integrated part of this work. Some supplementary materials for chapter 6 are given in appendix B.

1.4 Units and Convention

In this thesis atomic units are employed for all physical quantities, i.e., $m_e = 1$, $|e| = 1$, $\hbar = 1$, where m_e is the electron mass, e is the electron charge, $\hbar$ is Plank's constant divided by 2π. The atomic unit of length is the bohr, $a_0 = \hbar^2/m_e e^2 \approx 0.529\text{Å}$. The atomic unit of cross section is $a_0^2 \approx 28.0$ Mb, where a barn (b) equals $10^{-28} m^2$. The atomic unit of energy is the Hartree, $E_h = m_e e^4/\hbar^2 \approx 27.2\,\text{eV}$.

In this thesis most of our calculated results are LDOS (angular momentum projected density of states) and K-edge XANES (x-ray absorption near edge structure) spectra. In FEFF calculations the XANES spectrum output is normalized within 50 eV of the threshold (edge) energy. In order to compare with experiments we have scaled the spectrum and hence the y-axis has arbitrary units.

1.5 Review of x-ray spectroscopy

1.5.1 x-ray absorption

For the purpose of this thesis we now briefly discuss a few fundamental concepts of x-ray absorption (XAS) and x-ray emission (XES) spectra. In XAS, the light with intensity I_0 hits the sample with thickness l, and according the Beer-Lambert law

$$I = I_0 e^{-\mu(E) l}. \tag{1.2}$$

This equation can be re-written for the *absorption coefficient* as,

$$\mu(E) = -(dI/dl)/I. \tag{1.3}$$

This coefficient is also related to the scattering cross-section of the absorbing center inside the material as

$$\mu(E) = \sigma_{tot}(E)\, n_a, \tag{1.4}$$

where n_a is the density of scattering atoms in the sample.

The naming convention of the edge in spectroscopy depends on the type of core-level excitation, e.g., for the K edge, x-ray excites a 1s electron. The excited electron then fills an unoccupied p state following the dipole selection rule $\triangle l = \pm 1$. Thus the x-ray absorption, and more precisely the x-ray near edge absorption spectrum (XANES) maps out the unoccupied density of states near the Fermi energy. In this process the photoelectron sees the effects of the screened core-hole which it leaves behind, and the spectrum is broadened by the life time of the core-hole. The absorption spectrum can be further broadened by the extrinsic and intrinsic losses which are discussed by Luke Campbell in the context of RSGF method [24].

1.5.2 x-ray emission spectroscopy

In the context of our RSGF code, XES refers to the x-ray emission spectroscopy. In practice, one can think of XES as an inverse process of XAS where the occupied states below the Fermi energy fill out an existing hole according to the dipole selection rule. Thus XES maps out the occupied density of states, including those near the Fermi energy. In this process the energy broadening is negligible since the hole, which was left behind by the electron, is very close to the Fermi energy and has a much longer life time.

Chapter 2

BACKGROUND THEORY

In this chapter we review the background theory which is relevant to our work presented in this thesis. In general, our development of computational methods for calculating x-ray spectroscopy of correlated systems, is built on real-space Green's function (RSGF) theory and a Hubbard model with an *ab initio* determination of U and a many-pole approximation to the GW self-energy. The multiple scattering formalism of RSGF method is formally equivalent to the much celebrated density functional theory in many aspects. Both approaches are extendable to a quasiparticle description by incorporating a GW like approximation. Here we briefly review the GW approximation and DFT and their limitation in the regime of highly localized Coulomb correlation. This is where the Hubbard model enters into the picture, and it is briefly reviewed in this chapter.

2.1 Real-space Green's function theory

2.1.1 Single-particle Green function

The theoretical description of the excitation of a core-level electron by an x-ray requires a framework that links the N particle with the $(N \pm 1)$ particle systems. The Green's function technique is one of the useful methods that enables one not only to calculate the ground state energies as in density functional theory but also attack the problems of excitation and ionization energies, transition matrix elements, absorption coefficients, dynamical polarizabilities, and elastic and inelastic cross-sections. Such techniques are discussed in various many-body physics text books, e.g., Fetter and Walecka [25]. Here we summarize some of these background theories by mostly following the language and convention of Hedin and others [10, 11, 26, 27]. The Green's function $iG^e(\mathbf{r}t, \mathbf{r}'t')$ is defined [11, 26] as the probability amplitude for the propagation of an electron from $(\mathbf{r}', t')$ to $(\mathbf{r}, t)$ in a many electron system where the Hamiltonian can be expressed as

$$\hat{H} = \sum_i \left[-\frac{1}{2}\nabla_i^2 + V_{ext}(\mathbf{r}_i) \right] + \frac{1}{2}\sum_{i \neq j} v_{ee}(\mathbf{r}_i, \mathbf{r}_j). \tag{2.1}$$

Here $V_{ext}(\mathbf{r})$ is the potential by the atomic nuclei, $v_{ee}(\mathbf{r}, \mathbf{r}') = 1/(4\pi\varepsilon_o|\mathbf{r}, \mathbf{r}'|)$ is the electron-electron interaction, ε_o is the dielectric constant, and $\hbar = m_e = 1$.

The time-ordered (causal) Green's function G^c is defined as an expectation value with respect to the many-electron state $|N\rangle$ [26] is

$$G^c(\mathbf{r}t, \mathbf{r}'t') = -i \left\langle \Psi_0^N \left| \hat{T} \left[\hat{\psi}(\mathbf{r}t) \hat{\psi}^\dagger(\mathbf{r}'t') \right] \right| \Psi_0^N \right\rangle, \tag{2.2}$$

where the $\hat{T}$ is time ordering operator. Depending on t and t', the above equation can be written as

$$G^c(\mathbf{r}t, \mathbf{r}'t') = G^e(\mathbf{r}t, \mathbf{r}'t') - G^h(\mathbf{r}t, \mathbf{r}'t'), \tag{2.3}$$

where $\psi(\mathbf{r}t)$ and $\psi^\dagger(\mathbf{r}'t')$ are the electron annihilation and creation field operators at time t and t', respectively, on the N-electron ground state. $G^e(\mathbf{r}t, \mathbf{r}'t')$ and $G^h(\mathbf{r}t, \mathbf{r}'t')$ are the Green's function for electron ($t > t'$) and hole ($t < t'$) propagators in N+1 and N-1 electron system respectively. $G^e(\mathbf{r}t, \mathbf{r}'t')$ can be expressed as,

$$G^e(\mathbf{r}t, \mathbf{r}'t') = -\frac{1}{\hbar} \left\langle \Psi_0^N \left| \hat{\psi}(\mathbf{r}t) \hat{\psi}^\dagger(\mathbf{r}'t') \right| \Psi_0^N \right\rangle \theta(t - t'), \tag{2.4}$$

where $\theta(t - t')$ is the Heaviside step function that can take value 1 or 0 based on $t > t'$ or $t < t'$. In this causal Green's function, the hole propagator is

$$G^h(\mathbf{r}'t', \mathbf{r}t) = -\frac{1}{\hbar} \left\langle \Psi_0^N \left| \hat{\psi}^\dagger(\mathbf{r}'t') \hat{\psi}(\mathbf{r}t) \right| \Psi_0^N \right\rangle \theta(t' - t), \tag{2.5}$$

Although the causal Green's function is mathematically convenient and particularly useful for Feynman's diagram techniques [27], a physically more meaningful Green's function is *retarded* Green's function $G^r(\mathbf{r}t, \mathbf{r}'t')$ that can be used to calculate the linear response of a system to an external field [25, 27]. The density of states is also proportional to the imaginary part of the single-particle retarded Green's function. The Fourier transformation of the retarded Green's function $G^r(\mathbf{r}t, \mathbf{r}'t')$ is

$$G^r(\mathbf{k}, \omega) = -i\theta(t - t') \left\langle \Psi_o \left| \left[c_k(t), c_k^\dagger(t') \right] \right| \Psi_o \right\rangle. \tag{2.6}$$

This Green's function is also known as the retarded Green's function of second kind where the electron Green's function defined in eq.2.4 is sometimes referred as retarded first kind Green's

function. In RSGF formalism we determine the real-space version of this retarded Green's function of second kind $G^r(\mathbf{r}t,\mathbf{r}'t')$.

2.1.2 Spectral function

Starting with the causal Green's function, we first address how Green's functions relate to exited state quasi-particle energy states. In order to obtain the Lehman representation of the causal Green's function, following Hedin [10] the quasi-particle amplitudes are defined as

$$f_i^{N-1}(\mathbf{r}) = \langle N-1, i|\hat{\psi}(\mathbf{r})|N\rangle\,, \tag{2.7}$$

and

$$f_i^{N+1}(\mathbf{r}) = \langle N|\hat{\psi}(\mathbf{r})|N+1, i\rangle\,. \tag{2.8}$$

Here, $\varepsilon_i^{N-1} = E_0^N - E_i^{N-1}$ and $\varepsilon_i^{N+1} = E_i^{N+1} - E_0^N$. Now using $t-t' = \tau$, the Fourier transform of the Green's function can be written in terms of the above amplitudes [26],

$$G(\mathbf{r},\mathbf{r}',\omega) = \sum_i \frac{f_i^{N+1}(\mathbf{r})\, f_i^{N+1*}(\mathbf{r}')}{\hbar\omega - \varepsilon_i^{N+1} + i\eta} + \sum_i \frac{f_i^{N-1}(\mathbf{r})\, f_i^{N-1*}(\mathbf{r}')}{\hbar\omega - \varepsilon_i^{N-1} - i\eta}. \tag{2.9}$$

We see that the above expression has poles at true many-particle excitation energies $\varepsilon_i^{N\pm1}$. In the independent particle picture f_i^{N+1} is the unoccupied and f_i^{N-1} is the occupied single-particle state with corresponding energies of $\varepsilon_i^{N\pm1}$. In this representation the spectral function $A(\omega) = \left|\frac{1}{\pi} ImG(\omega)\right|$ in a finite system now becomes,

$$A(\mathbf{r},\mathbf{r}',\omega) = \sum_i f_i^{N+1}(\mathbf{r})\, f_i^{N+1*}(\mathbf{r}')\delta(\omega - \varepsilon_i^{N+1}) + \sum_i f_i^{N-1}(\mathbf{r})\, f_i^{N-1*}(\mathbf{r}')\delta(\omega - \varepsilon_i^{N-1}). \tag{2.10}$$

Here the first term can be expressed as $A^+(\mathbf{r},\mathbf{r}',\omega)$ and the second term as $A^-(\mathbf{r},\mathbf{r}',\omega)$.

The Fourier transformed retarded Green's function $G^r(\mathbf{k},\omega)$ can be written in terms of these spectral functions

$$G^r(\mathbf{k},\omega) = \int_0^\infty d\omega' \left[\frac{A^+(\mathbf{k},\omega)}{\omega - \omega' - \mu + i\delta} + \frac{A^-(\mathbf{k},\omega)}{\omega + \omega' - \mu + i\delta}\right]. \tag{2.11}$$

Generally one calculates the causal Green's function using Feynman's diagrams or other perturbation techniques which gives $A^+(\mathbf{k},\omega)$ and $A^-(\mathbf{k},\omega)$. Using these spectral functions one then

calculate the retarded Green's function. But in our RSGF approach we calculate the real-space retarded Green's function $G^r(r,r',\omega)$ directly using multiple-scattering formalism. This method will be briefly discussed in the next section, and a detailed description can be found in ref. [28, 29].

2.1.3 Excited State Electronic structure from Green's Function

Green's function methods are particularly useful for excited state electronic structure calculation. In this approach physical quantities of interest are expressed in terms of the quasi-particle Green's function $G(\mathbf{r},\mathbf{r}',E)$. For example, the physical quantity measured in XAS for photons of polarization $\hat{\varepsilon}$ and energy ω is the x-ray absorption coefficient $\mu(\omega)$ which can be expressed as

$$\mu(\omega) \propto -\frac{2}{\pi}\mathrm{Im}\left\langle \phi_c|\,\hat{\varepsilon}\cdot\mathbf{r}\,G(\mathbf{r},\mathbf{r}',\omega+E_c)\,\hat{\varepsilon}\cdot\mathbf{r}'|\phi_c\right\rangle, \tag{2.12}$$

where E_c is the core electron energy and $|\phi_c\rangle$ is the core state wave function. The FEFF9 code also calculates closely related quantities such as the spin and angular momentum projected density of states (lDOS) $\rho_{l\sigma}^{(n)}(E)$ at site n,

$$\rho_{l\sigma}^{(n)}(E) = -\frac{1}{\pi}\mathrm{Im}\sum_m \int_0^{R_n} G_{L,L}^{\sigma,\sigma}(r,r,E)\,r^2\,dr, \tag{2.13}$$

where R_n is the Norman radius around the nth atom [29], which is analogous to the Wigner-Seitz radius of neutral spheres. The coefficients $G_{L,L'}^{\sigma,\sigma'}$ characterize the expansion of the Green's function $G(\mathbf{r},\mathbf{r}',E)$ in spherical harmonics,

$$G(\mathbf{r},\mathbf{r}',E) = \sum_{L,L',\sigma} Y_L(\hat{\mathbf{r}})\,G_{L,L'}^{\sigma,\sigma}(r,r',E)\,Y_{L'}^*(\hat{\mathbf{r}}'), \tag{2.14}$$

where $L=(l,m)$ denotes both orbital and azimuthal quantum numbers. In these formulae, the quasi-particle Green's function for an excited electron at energy E is given formally (matrix-indices suppressed) by

$$G(E) = [E - H - \Sigma(E)]^{-1}, \tag{2.15}$$

where H is the Hartree Hamiltonian

$$H = \frac{p^2}{2} + V, \tag{2.16}$$

and V is the Hartree-potential. For convenience in our calculations, the Hamiltonian is re-expressed in terms of a Kohn-Sham Hamiltonian $H^{\mathrm{KS}} = H + V_{\mathrm{xc}}$ where V_{xc} is a ground state exchange-correlation functional[30], and the self-energy is replaced by a modified self-energy $\Sigma(E) - V_{\mathrm{xc}}$

which is set to zero at the Fermi-energy $E = E_F$. In this thesis we use the von Barth-Hedin LSDA functional $V_{\rm xc}[n(\mathbf{r}), m(\mathbf{r})]$ [30], where $n(\mathbf{r}) = n_\uparrow + n_\downarrow$ is the total electron density and $m(\mathbf{r}) = n_\uparrow - n_\downarrow$ is the spin polarization density. In practice, it is useful to decompose the total Green's function $G(E)$ as

$$G(E) = G^c(E) + G^{sc}(E), \tag{2.17}$$

where $G^c(E)$ is the contribution from the central (absorbing) atom and $G^{sc}(E)$ is the scattering part. The multiple scattering formalism is briefly discussed in the following section.

In the FEFF code a typical calculation of the electronic structure (ground or excited state) starts with a self-consistent calculation of the electron density and Kohn-Sham potentials [29]. Once the self-consistent potential is obtained, the Green's function is constructed and used to calculate XAS and other quantities of interest. Of particular interest in this paper is the spin-dependent density matrix for the n-th site

$$n^{\sigma\sigma'}_{nlm,nlm'} = -\frac{1}{\pi}\int^{E_F} dE \int_{cell} \mathrm{Im}\, G^{\sigma\sigma'}_{nlm,nlm'}(\mathbf{r},\mathbf{r},E)\, d^3r, \tag{2.18}$$

where n denotes the cell defined by the Norman sphere centered about the n^{th} atom, $\mathbf{r}, \mathbf{r}'$ are relative to the center of the cell R_n, and σ is the spin-index, and we explicitly designate the azimuthal quantum numbers m and m'.

2.2 Multiple-scattering formalism for x-ray spectroscopy

As in Eq. (2.13), The total Green's function is treated in two different parts, G^c and G^{sc}. To calculate these two parts we only need to know the free electron Green's function G^0 and the scattering matrix t_i where

$$t_i = v_i + v_i G^0 t_i. \tag{2.19}$$

The RSGF code FEFF uses the muffin-tin approximation for potential where $V = \sum_i v_i$ inside the muffin-tin radius and $V = 0$ in the interstitial region. Here the index i is summed over all muffin-tin sites in the cluster. The free electron propagator G^0 is defined as

$$G^0(\mathbf{r},\mathbf{r}',E) = -\frac{2k}{4\pi}\frac{e^{ik|\mathbf{r}-\mathbf{r}'|}}{k|\mathbf{r}-\mathbf{r}'|}, \tag{2.20}$$

where $k = \sqrt{2(E - V_{mt})}$ and V_{mt} stands for potential at the muffin-tin radius.

The central atom Green's function $G^c = G^0 + G^0 t_c G^0$ from Eq. (2.13) can be written as a combination of regular and irregular solution of Schrödinger's equation,

$$G^c = -2k \sum_i \left[R_l(r_<,k) N_l(r_>,k) + i R_l(r,k) R_l(r',k) \right] \sum_m Y_l^{m*}(\hat{r}) Y_l^m(\hat{r'}) \tag{2.21}$$

Using Dyson's expansion the scattering part of the Green's function can be repackaged as

$$G^{sc} = G^c \left[\sum_{c \neq i \neq c} t_i + \sum_{c \neq i \neq j \neq c} t_i G^0 t_j + \sum_{c \neq i \neq j \neq k \neq c} \right] G^c, \tag{2.22}$$

where the sum starts and ends at the absorbing atom.

Full multiple scattering (FMS) calculations can be carried out by matrix inversion [28], i.e., with $G^{sc} = [1 - G^0 T]^{-1} G^0$, where T is the scattering T-matrix, which is represented in an angular-momentum and site basis: $T = t^{\sigma}_{nL} \delta_{L,L'} \delta_{n,n'} \delta_{\sigma,\sigma'}$. Finally, t^{σ}_{nL} is the single site scattering t-matrix, which is related to partial wave phase shifts,

$$t^{\sigma}_{nL} = e^{i\delta^{\sigma}_{nL}} \sin(\delta^{\sigma}_{nL}). \tag{2.23}$$

The full multiple scattering is considered "full" only within the given cluster size. For a more detailed description of the multiple scattering RSGF method see Gonis *et al.* [28], and Rehr *et al.* [29, 31].

2.3 Density Functional Theory and GW Approximation

Although quasi-particle Green's function theory is very efficient for excited states, in the ground-state regime such approaches are completely equivalent to the effective single-particle density functional theory (DFT). Additionally, there are various similar techniques in both theories, such as the treatment of missing correlation by a quasi-particle GW self-energy in the Green's function method and improved exchange-correlation potentials in DFT. Also, treating strongly correlated systems with localized electrons by implementing Hubbard model [8] or Anderson impurity model [32] in both theories have some common strategies. Although in our RSGF multiple-scattering theory no final state wave functions are calculated, in contrast with DFT, considering all these similarities in their many-body extensions it might be worth reviewing some basic concepts and approximations of DFT.

2.3.1 Fundamentals of DFT

Perhaps the most celebrated and successful post Hartree-Fock theory to study many-body ground state is the density functional theory (DFT). Although currently the work-horse of DFT is the well known Kohn-Sham self-consistent formalism [33] with different kinds of exchange-correlation functionals, the historical development of DFT follows primarily from the construction of Hohenberg-Kohn theorem [34], Mermin functional [35], and finally LDA description of Kohn-Sham theory [33]. The discussion here will mostly follow from some of these references and summarize the central concept of DFT.

In the **Hohenberg-Kohn theory**, one realizes the strength of the density functionals from the two theorems: i) Ground state density $n_0(\mathbf{r})$ uniquely determines any external potential $V_{ext}(\mathbf{r})$ in a system of interacting particles, and *therefore, all properties of the system are completely determined from the ground state density*; and ii) the density $n(\mathbf{r})$ that minimizes the energy functional $E[n]$ is the exact ground state density $n_0(\mathbf{r})$.

The proofs of these extremely powerful theorems are available in many texts and papers [34], and will not be discussed in details here. The energy functional is generally written as

$$E_{\rm HK}[n] = T[n] + E_{int}[n] + \int d^3r V_{ext}(\mathbf{r}) n(\mathbf{r}) + E_N, \tag{2.24}$$

where the first two terms are called *universal functional* F_{HK},

$$F_{\rm HK}[n] = T[n] + E_{int}[n]. \tag{2.25}$$

This is universal since in the presence of V_{ext} this kinetic $T[n]$ and internal interaction $E_{int}[n]$ is same for any interacting system and can be determined from $n_0(\mathbf{r})$ in principle.

Despite the appeal and robustness of this theory, no prescription was suggested to solve the many-body problem, e.g., from $V_{ext} \rightarrow \Psi(\mathbf{r}) \rightarrow n_0(\mathbf{r}) \rightarrow E_{min}[n_0]$. Shortly after Hohenberg-Kohn paper, in 1965, David Mermin constructed a density functional theory based on finite temperature ensemble theory [35]. Using a trial density matrix $\hat{\rho}$, he showed that the grand partition function is given by,

$$\Omega[\hat{\rho}] = Tr\left[\hat{\rho}(\hat{H} - \mu\hat{N}) + \frac{1}{\beta} ln\hat{\rho}\right], \tag{2.26}$$

where the minimum is achieved by the equilibrium density $\hat{\rho_0}$,

$$\Omega_{min} = \Omega[\hat{\rho_0}] = -lnTre^{-\beta(\hat{H}-\mu\hat{N})}. \tag{2.27}$$

Just like Hohenbeg-Kohn theory, the energy in Mermin theory depends upon the external potential only through the term $\int V_{ext}(\mathbf{r})n(\mathbf{r})$. Although this finite temperature theory is more powerful than the ground state HK theory since it does not only determine the total energy, but the entropy, specific heat, etc. as functionals of $\hat{\rho_0}$, but it was much more difficult to construct for practical purpose [36].

Finally, in the same year 1965, the most computable and celebrated construct of DFT was proposed by the ground breaking work of Walter Kohn and Lu Jeu Sham [34]. The many-body exact Hohenberg-Kohn energy functional $E_{HK}[n]$ was realized as an effective single particle Hamiltonian and a Schrödinger like equation , also known as the Kohn-Sham equation. To see this development, the Hohenberg-Kohn energy functional (Eq. 2.20) can be re-expressed as Kohn-Sham energy functional E_{KS},

$$E_{\mathrm{KS}}[n] = T_s[n] + \int d\mathbf{r} V_{\mathrm{ext}}(\mathbf{r})n(\mathbf{r}) + E_{\mathrm{H}}[n] + E_N + E_{\mathrm{xc}}[n]. \tag{2.28}$$

Here T_s is the independent-particle kinetic energy,

$$T_s = -\frac{1}{2}\sum_{\sigma,i=1}^{N^\sigma} \left\langle \psi_i^\sigma \left| \nabla^2 \right| \psi_i^\sigma \right\rangle = \frac{1}{2}\sum_{\sigma,i=1}^{N^\sigma} \left|\nabla\psi_i^\sigma\right|^2. \tag{2.29}$$

By taking a variation with respect to $n(\mathbf{r})$, the Kohn-Sham equation is obtained as,

$$\left(-\frac{1}{2}\nabla^2 + v_{\mathrm{eff}}^\sigma(\mathbf{r})\right)\psi_i^\sigma(\mathbf{r}) = \varepsilon_i\psi_i^\sigma(\mathbf{r}), \tag{2.30}$$

where the $\psi_i^\sigma(\mathbf{r})$ are the Kohn-Sham orbitals and the single-particle effective potential

$$v_{\mathrm{eff}}(\mathbf{r}) = v_{\mathrm{ext}}(\mathbf{r}) + v_{\mathrm{H}}(\mathbf{r}) + v_{\mathrm{xc}}^\sigma(\mathbf{r}). \tag{2.31}$$

Here all the terms including $v_{\mathrm{H}}(\mathbf{r}) = \int n(\mathbf{r})/\left|\mathbf{r}-\mathbf{r}'\right| d\mathbf{r}'$ are known except for the last term $v_{\mathrm{xc}}(\mathbf{r}) = \delta E_{\mathrm{xc}}[n(\mathbf{r})]/\delta n(\mathbf{r})$, which is also known as the exchange-correlation (XC) term. It is the exchange and correlation term (v_{xc}) whose correct determination has been the central challenge since the formulation of Kohn-Sham theory. In principle v_{xc} should incorporate all the correlation physics that is missing from the single-determinant Hartree-Fock theory. In practice, many variations of exchange-correlation potentials are constructed from free electron gas (FEG) approximation, e.g., LDA, GGA,

LSDA and their hybrids. Such formulations are highly successful in many finite systems and *sp*-solids with delocalized electrons. But they are limited in their descriptio of the electronic structure in systems with localized electrons, mostly due to the inherent itinerant nature of the FEG approach. More on this will be discussed in chapter 3.

2.3.2 Local spin density approximation LSDA

In LSDA [30] one sets the functional dependence of $\varepsilon_{\rm xc}(n(\mathbf{r},\sigma)$ to be that of a homogenous electron gas. The term *'local'* in LSDA implies that at a small volume dV around $\mathbf{r}$, the local energy density becomes that of the homogenous electron gas, or $\varepsilon_{\rm xc} \longrightarrow \varepsilon_{\rm xc}^{HEG}$. Thus,

$$\delta E_{\rm xc}[n] = \sum_{\sigma} \int d\mathbf{r} \left[\varepsilon_{\rm xc}^{HEG} + n \frac{\delta \varepsilon_{\rm xc}^{HEG}}{\delta n^{\sigma}} \right]_{\mathbf{r},\sigma} \delta n(\mathbf{r},\sigma), \tag{2.32}$$

and the potential becomes

$$v_{\rm xc}^{\sigma}(\mathbf{r}) = \left[\varepsilon_{\rm xc}^{HEG} + n \frac{\delta \varepsilon_{\rm xc}^{HEG}}{\delta n^{\sigma}} \right]_{\mathbf{r},\sigma}. \tag{2.33}$$

The LSDA exchange terms are exactly

$$v_x^{\sigma} = \frac{4}{3} \varepsilon_x^{HEG}(n(\mathbf{r},\sigma)), \tag{2.34}$$

but LDA correlation term v_c^{σ} is not so trivial and can not be calculated exactly. Several estimations were given by other authors, e.g., Hedin-Lundqvist [10], Ceperley and Alder [37], etc. For spin polarized systems, the LSDA can be formulated in terms of either two spin densities $n^{\uparrow}(\mathbf{r})$ and $n^{\downarrow}(\mathbf{r})$, or the total density $n(\mathbf{r}) = n^{\uparrow}(\mathbf{r}) + n^{\downarrow}(\mathbf{r})$ and the fractional spin polarization $m(\mathbf{r})$ following von Barth-Hedin prescription [30],

$$m(\mathbf{r}) = \frac{n^{\uparrow}(\mathbf{r}) - n^{\downarrow}(\mathbf{r})}{n^{\uparrow}(\mathbf{r}) + n^{\downarrow}(\mathbf{r})}. \tag{2.35}$$

For unpolarized systems, the LDA is found simply by setting $n^{\uparrow}(\mathbf{r}) = n^{\downarrow}(\mathbf{r}) = n(\mathbf{r})/2$.

In our RSGF method the potential is calculated self-consistently in a spin-averaged manner regardless of the polarization of the system. Once the potential is converged, $\Delta V_{\rm xc}(n(\mathbf{r}), m(\mathbf{r}))$ is implemented using von Barth-Hedin prescription in a single shot approach.

Although our Green's function approach only incorporates LSDA in a single step, some of the limitations of FEG thus becomes inevitable. For localized systems with d or f electrons, we needed to go beyond LSDA and this will be the primary topic of this thesis.

2.3.3 Orbital-dependent functionals for SIC and LDA+U

Minimizing the LDA energy functional with respect to density in an unrestricted manner tends to overly delocalize the electron orbitals or wrongly localize inappropriate states. Many systems with delocalized *s* or *p* valence electrons were found to work well with LSDA functionals. But the situation becomes severe for correlated systems and various methods have been developed to incorporate strong correlation. Among the most successful of these are SIC [38] and LDA+*U* [12].

SIC stands for "self interaction corrections" and is not needed in the Hartree-Fock theory since the self-interaction in the Hartree term V_{H} is exactly canceled by the exchange term V_x. But this is not automatically done in the LDA approximation of E_{xc}. For strongly correlated systems where the electron-electron Coulomb interaction is non-negligible due to the localized orbitals, this error can bring severe consequences. In extended systems, the exchange-correlation term is constructed by subtracting the self-interaction term. There have been several studies using SIC-LSDA within DFT [14] and Green's function [39] framework that show significant improvement in the description of magnetism and magnetic ordering in transition metal oxides, high T_c cuprates, and rare earth compounds.

In contrast to SIC, LDA+*U* adds an explicit orbital dependent term in the Hamiltonian where appropriate double counting terms are subtracted. Such a construction is motivated from the Hubbard model [8, 9] where the onsite Coulomb interaction is very strong due to the presence of localized orbitals. The term *U* can be obtained from the screened electron-electron interaction within *d* or *f* orbitals. In real systems it is often a very difficult task to calculate screening from first-principles. Thus *U* has often been taken as a fitting parameter with respect to experimental results on the magnetic moment or the band-gap of correlated systems.

The prototype systems are the transition metal oxides, e.g., NiO, MnO, and CoO which are anti ferromagnetic insulators but incorrectly predicted as metals by conventional DFT. On the other hand, an arbitrariness of LDA+*U* comes from the double counting term which is often not very easy to determine in a mean-field theory such as LSDA. Another shortcoming of this approach is the absence of a good screening model which often leads one to rely on a parametric determination of *U*.

2.3.4 GWA self energy model for excited states

The discussion in this section is mostly following Hedin *et al.* [10] and Aryasetiawan *et al.* [40]. Whether it is in a Green's function based multiple-scattering approach or in a wave-function based DFT approach, the GW approximation is the one of the earliest and most generally accurate development for calculating the quasi-particle energies. This is formally the first term in the perturbative expansion of the electron self-energy in powers of screened interaction W, and was first applied to the electron gas by Hedin [10]. The quasi-particle equation can be written as

$$\left(-\frac{1}{2}\nabla^2 + v_{ext}(\mathbf{r}) + v_{Hartree}(\mathbf{r}) + \int d\mathbf{r}'\Sigma^{\sigma}(\mathbf{r}',\mathbf{r},\omega)\right)\psi_i^{\sigma}(\mathbf{r}) = \varepsilon_i\psi_i^{\sigma}(\mathbf{r}). \tag{2.36}$$

The GWA is formally given by

$$\Sigma(\mathbf{r}',\mathbf{r},\omega) = \frac{i}{2\pi}\int_{-\infty}^{\infty} d\omega' G(\mathbf{r}',\mathbf{r},\omega+\omega')W(\mathbf{r}',\mathbf{r},\omega')e^{i\delta\omega'}, \tag{2.37}$$

where the $W(\mathbf{r}',\mathbf{r},\omega)$ is the screened Coulomb interaction with dielectric function $\varepsilon(\mathbf{r}',\mathbf{r},\omega)$. A detailed discussion of the GWA is beyond the scope of this thesis, but here we will mention that a robust implementation of the GWA can be made in both DFT and Green's function based approaches. In the language of DFT, the self-energy $\Sigma^{\sigma}(\mathbf{r}',\mathbf{r},\omega)$ is a non-local and energy dependent extension of the static and local exchange-correlation potential $V^{\sigma}(\mathbf{r})$. It was also formally shown by Gunnarsson *et al.* [41] that for localized systems, such as transition metal oxides or actinide compounds, the LDA+U is an approximation to the GWA.

2.4 Theory of localized electrons and strong correlation

2.4.1 Hubbard Model

Several properties of strongly correlated systems are best described by three parameters, the ratio between the electron-electron Coulomb repulsion and the ratio U/t, average electron occupancy n, and the dimensionless temperature T/t. The interplay between these parameters has most successfully been captured by the Hubbard model. Despite its simplicity, the Hubbard model has been acknowledged as the paradigm of strong correlation physics, and, even after 40 years of intense investigation, many of these Hubbard model systems remain the topic of heated debate.

The Hubbard model [8] typically starts with a simple looking Hamiltonian,

$$\hat{H} = -t \sum_{\langle ij \rangle} a^{\dagger}_{i\sigma} a_{j\sigma} + U \sum_{i} \hat{n_{i\uparrow}} \hat{n_{i\downarrow}}, \tag{2.38}$$

where $\langle i\,j \rangle$ are to denote the neighboring sites, t is the hopping matrix term, and U is the on-site Coulomb or Hubbard interaction.

In systems where $U/t \ll 1$, the hopping dominates over on-site Coulomb interaction. This happens when t is very large due to significant overlap between the orbitals on different sites. With these orbitals, the Hubbard model then approaches a metal-like description of itinerant electrons. On the other hand when $U/t \gg 1$ in a half-filled system, hopping is suppressed and double occupancies due to a transition from a neighbouring site is inhibited by the energy cost U. Thus, the onsite Coulomb interaction between the localized electrons drives the system from the metal phase to the insulating phase.

The most interesting aspect of Hubbard model comes from its integration with electronic structure theory such as DFT so one can study more realistic systems. Many of the transition metal oxides and the parent compounds of High T_c cuprates are now realized as insulators with correlation gaps, and are formally called Mott-Hubbard insulators.

2.4.2 Antiferromagnetism and Mott transition

Experimentally the low temperature Mott-Hubbard insulators are always found to be accompanied by an antiferromagnetic phase [42, 43]. This is also the case for NiO, MnO and $La_{2-x}Sr_xCuO_4$. The correlation between their insulating phase and magnetism is explained by a mechanism called "super exchange" and can be understood within the Hubbard model systems. Here we will try to gain an intuitive understanding of this phenomenon.

The discussion in this chapter follows from the text by Alexander Altland [43]. In the strong-coupling limit U is much larger than t (e.g., $U \gg t$) in Hubbard model. When $t \approx 0$ there will be exactly one electron at every lattice site corresponding to the ground state of the entire system. Through fluctuation, anti-parallel electrons between two neighboring sites can hybridize by making a transition to an intermediate virtual state in which one site becomes doubly occupied. This virtual state has energy U above the ground state. This state decays quickly by hopping the electrons on to neighboring site and reducing the overall energy. Thus the system remains an antiferromagneitc

insulator with half-filled lower Hubbard band and fully unoccupied upper Hubbard band. Such strong coupling Hubbard systems are often described with a **t-J** Hamiltonian [43],

$$\hat{H}_{t-J} = -t \sum_{\langle mn \rangle} a^{\dagger}_{m\sigma} a_{n\sigma} + J \sum_{\langle mn \rangle} \hat{\mathbf{S}_m} \cdot \hat{\mathbf{S}}_n, \tag{2.39}$$

where the second term can be easily recognized from Hisenberg model, and $J \sim t^2/U$.

With doping the Mott-Hubbard insulators become very difficult to explain. The removal of electrons introduces vacancies in the lower Hubbard band which can then propagate through the lattice. Doping dependent phenomena in LSCO has created significant interest in the recent years [19, 44–46]. The parent compound La_2CuO_4 is build of layers of CuO_2 separated by rare earth ion lanthanum. At half-filling the Cu sites adopt a $3d^9$ configuration. In this system the Fermi energy lies in the middle of $d^{x^2-y^2}$ orbital of copper. In a simple band picture, this single band is exactly half-filled and therefore metallic. However, strong Coulomb interaction drives the cuprate system to be an anti-ferromagnetic Mott-Hubbard insulator [42]. In $La_{2-x}Sr_xCuO_4$ however, the lower Hubbard band is introduced with charge carriers. Thus with increasing doping concentration, the Hubbard gap collapses and the unconventional superconducting phase evolves. The mechanism is believed to be due to the exchange of antiferromagnetic spin fluctuations. This explanation is still not conclusive and the subject of great controversy and speculation. In chapter 4 we will study the overdoped phase of LSCO based on a single band Hubbard model with a doping dependent self-energy.

Chapter 3

HUBBARD MODEL CORRECTIONS IN REAL-SPACE X-RAY SPECTROSCOPY THEORY

We have implemented the Hubbard model in real-space multiple scattering Green's function (RSGF) calculations of x-ray spectra based on a rotationally invariant LDA+*U* formalism. We have also estimated values of the Hubbard parameter *U* using the constrained RPA method that was originally developed by Yoshinari Takimoto [47] and Joshua J. Kas, and details can be found in Ref.[23]. For this development we followed cRPA approach as prescribed by Aryasetiawan *et al.* [48]. Our treatment also includes a model self-energy which incorporates the interaction of the photo-electron with excitations such as plasmon; this model is based on an electron gas Green's function and a many-pole model of the screened Coulomb interaction *W*. This combined treatment leads to an efficient approach to account for correlation on localized as well as delocalized electrons, and its effects on x-ray spectra. Moreover, the RSGF formalism is also applicable to general aperiodic systems including nano-particles, molecules, and surfaces. Results are presented for the spin and angular momentum projected density of states of MnO, NiO, and $La_{2-x}Sr_xCuO_4$ (LSCO), for the K-edge x-ray spectra of O atoms in MnO and NiO, and the unoccupied electronic states and O K-edge spectra of undoped LSCO. The method is found to yield reasonable agreement with experiment. We have reported our findings to Physical Review B [23].

3.0.3 Outline of this chapter

After a brief introduction in section 3.2, we discuss Anisimov's prescription [13, 49] of LDA+*U* formalism in section 3.3. Our implementation of LDA+*U* in RSGF code FEFF9 is discussed in the later part of this section, namely section 3.3.2. The determination of the Hubbard parameter *U* and the many-pole approximation of the quasi-particle self-energy are briefly discussed in sections 3.4 and 3.5. Finally our LDA+*U* implemented RSGF calculation are presented and analyzed in sections 3.6 - 3.8.

3.0.4 Key Observation

With a cRPA calculated Hubbard parameter U, our LDA+U correction correctly accounts for the correlation gap in Mott insulators, e.g., NiO, MnO, and La_2CuO_4. The agreement with experiment is significantly improved with LDA+U for the calculated XANES and XES of the O K edge in these systems.

3.1 Introduction

Density functional theory (DFT) together with quasi-particle corrections has been remarkably successful in describing the electronic structure and band-gaps of weakly interacting s-p bonded systems. For such systems, quasi-particle corrections are often well described in terms of Hedin's GW self-energy [10, 50], where G refers to the one-particle Green's function and W the screened Coulomb interaction. Such corrections are especially important in treatments of excited states, e.g., in various x-ray spectra. However, the GW approach is generally inadequate to describe the band gap and other electronic properties in materials with well localized $3d$ or $4f$ electrons [12, 51]. On the other hand, the strong Coulomb interactions in these systems are often approximated using a Hubbard-model [12], in which the on-site electron-electron repulsion is represented by the spin- and orbital-occupancy dependent potential parameterized by "Hubbard parameters" U and J. Combining the local density approximation (LDA) of DFT with the Hubbard model leads to the LDA+U method. In practice, the Hubbard correction is added to the original Kohn-Sham LDA Hamiltonian while an approximate mean-field term is subtracted to avoid double-counting [49]. Formally the Hubbard interaction can be regarded as a static approximation to the self-energy of correlated systems [1]. In calculations of excited state properties, however, one also needs dynamic self-energy effects due to delocalized excitations, i.e., plasmon etc., which can be approximated by model GW calculations. A related approach has been proposed by Jiang *et al.* [1, 52], where a GW self-energy is calculated from an LDA+U starting point and the infamous double counting terms largely cancel. Their approach also yields good approximations for the band-gap of several d and f electron systems [1, 52]. In another prescription, Bansil *et al* developed a self-consistent GW+U scheme based on the tight-binding approximation and a single-band Hubbard model [53, 54]. Their method is found to qualitatively explain several pre-edge spectral features in high T_c cuprates [22, 55].

The approach developed here is based on the LDA+U formalism of Anisimov *et al.* [49], together with a many-pole model self-energy, that treats all excitations as plasmonic in nature. This model is not expected to contribute appreciably to the correlation effects on localized states, so we simply add the two contributions to form an effective self-energy correction $\Delta\Sigma^U(E)$. The implementation of our Hubbard-corrected self-energy into the real-space multiple scattering Green's function formalism is relatively straightforward, and yields an efficient approach which is applicable to both weakly and strongly-correlated materials. Our RSGF/$\Delta\Sigma^U$ approach is advantageous for calculations of x-ray spectra over a broad spectrum, especially since it does not rely on structural symmetry or periodicity requirements.

Using this extension of our RSGF codes, we investigate the effects of correlation on the angular momentum projected density of states (lDOS), the x-ray absorption spectra (XAS), and the x-ray emission spectra (XES) of several materials. Other codes which can incorporate Hubbard corrections to excited state spectra include WIEN2K [56], SPRKKR [57], and Quantum ESPRESSO [58]. Our implementation of the Hubbard correction is similar to that in SPRKKR, although in that code U is taken as a parameter [57]. We also estimate U using the constrained RPA method implemented in our RSGF codes. Calculations of the Hubbard U have also been carried out by others, using both constrained LDA (cLDA [59–64]), and constrained RPA (cRPA [65, 66]) approaches. Both of these methods have been systematically compared by Aryasetiawan *et al.* [48].

Our RSGF/$\Delta\Sigma^U$ method is tested on several d-electron systems including MnO, NiO, and the undoped high T_c cuprate $La_{2-x}Sr_xCuO_4$ (LSCO). In these materials, the electronic structure and band gaps are strongly influenced by the Hubbard interaction. We find that our approach yields reasonable agreement with bulk-sensitive probes such as XES and XAS which are used to measure band gaps between occupied and unoccupied states [67]. We compare our results with related calculations for MnO and NiO using the GW@LDA+U treatment of Jiang *et al.* [1]. Treatments of Ti oxide compounds using LDA+U within the multiple scattering formalism have also been reported by Krüger [68], although, in that work a gap in the d-states was forced by splitting the occupied and unoccupied states by an experimental gap correction.

3.2 Hubbard model in Real-space Green's function Theory

3.2.1 LDA+U Formalism

As is well known, LDA in DFT is often not adequate to describe systems with localized electrons. The main problem comes from the fact that the energy functional and its derivative are both continuous under the LDA approximation where the well known derivation by Perdew *et al.* [69] showed that in an exact DFT the derivative of total energy E with respect to the number of electrons N should have discontinuities at integer values of N:

$$\frac{\partial E}{\partial N} = E(M) - E(M-1),\ M-1 < N < M = E(M+1) - E(M),\ M < N < M+1 \tag{3.1}$$

As a result, $V(\vec{r}) = \delta E[n(\vec{r})]/\delta n(\vec{r})$ will also have discontinuities at integer values of N for exact DFT. The absence of this potential jump in LDA DFT is thus responsible for the failure in describing the band gap of Mott insulators such as transition metal and rare-earth compounds as shown by Gunnarsson and Schonhammer [70].

In Anderson's impurity model [32] electrons are separated in two subsystems: localized d or f electrons where the $d-d$ interactions are added by $\sum_{i\neq j} n_i n_j$ in a model Hamiltonian and delocalized s and p electrons which is described by orbital independent one-electron LDA potential. In the localized or Hubbard space the total d-d energy is $UN(N-1)/2$ and should be subtracted from the total LDA energy $E^{LDA}(N)$ in order to avoid double counting. Thus Anisimov *et al.* [13] showed that ignoring exchange interaction and non-sphericity of $d-d$ interaction, the energy functional,

$$E = E_{LDA} - UN(N-1)/2 + \frac{1}{2}\sum_{i\neq j} n_i n_j \tag{3.2}$$

Taking the derivative of E with respect to $n(\vec{r})$ one obtains the potential $V(\vec{r})$,

$$V_i(\vec{r}) = V_{LDA}(\vec{r}) + U\,(\frac{1}{2} - n_i) \tag{3.3}$$

This clearly shows the discontinuous behavior of the potential depending on $n_i = 0$ or 1. A similar equation is also obtained for the single-particle eigen value,

$$\varepsilon^i = \frac{\partial E}{\partial n_i} = \varepsilon^i_{LDA} + U\,(\frac{1}{2} - n_i) \tag{3.4}$$

From the above equation, the highest occupied state ($n_i = 1$) shifts by $-U/2$ and lowest unoccupied state ($n_j = 0$) shifts by $+U/2$ creating a gap of size U. This oversimplified argument shows how

the potential jump causes the energy gap although it ignores non-sphericity of d-d interaction and exchange interaction.

Following Anisimov we will now start with an exact expression for the Hubbard model Energy functional and eventually derive a simplified and suitable expression for real-space Green's function theory.

$$E^{LDA+U}[n^{\sigma}(\vec{r}),\{n^{\sigma}\}] = E^{LDA}[n^{\sigma}(\vec{r})] + E^{U}[\{n^{\sigma}\}] - E_{dc}[\{n^{\sigma}\}], \tag{3.5}$$

where $n^{\sigma}(\vec{r})$ is the charge density and $\{n^{\sigma}\}$ is the density matrix. E^{U} is the Hubbard term,

$$E^{U}[\{n^{\sigma}\}] = \frac{1}{2}\sum_{mm'm''m'''\sigma}\{U_{mm',m''m'''}n^{\sigma}_{mm'}n^{-\sigma}_{m''m'''} + (U_{mm'm''m'''} - J_{mm'm'''m''})n^{\sigma}_{mm'}n^{\sigma}_{m''m'''}\}, \tag{3.6}$$

where the direct term $U_{mm'm''m'''} =< m,m'|V_{ee}|m'',m''' >$ and exchange term $J_{mm'm'''m''} =< m,m'|V_{ee}|m''',m'' >$. The double counting term in Eqn.5 for orbital independent LDA potential is

$$E_{dc}[\{n^{\sigma}\}] = \frac{1}{2}UN(N-1) - \frac{1}{2}J[N^{\uparrow}(N^{\uparrow}-1) + N^{\downarrow}(N^{\downarrow}-1)] \tag{3.7}$$

Here the total number of localized electrons $N = N^{\uparrow} + N^{\downarrow}$.

First approximation: If the localized electrons are of atomic type, the density matrix and Hubbard parameters can be approximated [13] as,

$$n^{\sigma}_{m}m' = n^{\sigma}_{m}\delta_{mm'}U_{mm'} =< mm'|V_{ee}|mm' > J_{mm'} =< mm'|V_{ee}|m'm > \tag{3.8}$$

Here we are ignoring the off-diagonal terms of the density matrix $n^{\sigma}_{mm'}$. Using the above expressions the simplified Hubbard term in the energy functional becomes

$$E^{U} = \frac{1}{2}\sum_{mm'\sigma}U_{mm'}n^{\sigma}_{m}n^{-\sigma}_{m'} + \frac{1}{2}\sum_{mm'\sigma}(U_{mm'} - J_{mm'})n^{\sigma}_{m}n^{\sigma}_{m'} \tag{3.9}$$

Using E^{U} and E_{dc} in the total energy functional $E[n(\vec{r}),\{n\}]$ we can now obtain $V(\vec{r}) = \delta E/\delta n(\vec{r})$.

Second Approximation: Following Anisimov and Sawatzky [13] we can do a further simplification by ignoring the non-sphericity of d-d interaction $U_{mm'} \rightarrow U$ and $J_{mm'} \rightarrow J$. With this approximation the total energy functional becomes,

$$\begin{aligned} E = E^{LDA} &+ \frac{1}{2}\sum_{m,m',\sigma}U(n^{\sigma}_{m} - n^{o})(n^{-\sigma}_{m'} - n^{o}) \\ &+ \frac{1}{2}\sum_{m,m'\neq m,\sigma}(U-J)(n^{\sigma}_{m} - n^{o})(n^{\sigma}_{m'} - n^{o}) \end{aligned} \tag{3.10}$$

Here double counting term E_{dc} is included by n^o where $n^o = n_d/10$ and $n_d = \sum_{m\sigma} n^\sigma_m$. The spin and orbital dependent potential thus becomes,

$$V^\sigma_{lm}(\vec{r}) = V^{LDA}(\vec{r}) + U\sum_{m'}(n^{-\sigma}_{lm'} - n_o) + (U-J)\sum_{m'\neq m}(n^\sigma_{lm'} - n_o) \tag{3.11}$$

3.2.2 Rotationally Invariant Implementation in Multiple-scattering Theory

Our construction of $V^U_{lm\sigma}(E)$ is adapted from the LDA+U approach of Anisimov *et al.* [49]. In their approach one starts with the total energy functional of the system and adds a Hubbard correction to account for the Coulomb interaction between localized, strongly correlated electrons. It is generally assumed [71] that a similar mean-field term should exist in LDA or other DFT approaches which must be subtracted from the energy functional to avoid double counting,

$$\begin{aligned} E^U[n^\sigma(\vec{r}), \mathbf{n}^\sigma] &= E^{LDA}[n^\sigma(\vec{r})] \\ &+ E^U[\mathbf{n}^\sigma] - E_{dc}[\mathbf{n}^\sigma], \end{aligned} \tag{3.12}$$

where $n^\sigma(\vec{r})$ is the charge density, $\mathbf{n}^\sigma$ the density matrix, E^U the Hubbard interaction, and E_{dc} the double counting term. The Hubbard term depends on the density matrix $n^{\sigma\sigma'}_{ilm,ilm'}$, and on-site Coulomb interactions between the localized electrons.

For systems where the localized electrons are atomic-like, the density matrix can sometimes be approximated [13] as

$$n^\sigma_{mm'} = n^\sigma_m \delta_{mm'}. \tag{3.13}$$

This spherical approximation is often not reasonable for many systems including TMOs, and good agreement for the band gap is found only when the non-sphericity of d-d interaction as well as the off-diagonal terms of $n_{mm'}$ are taken into account [13]. In order to implement basis independent formalism of LDA+U, we diagonalize the density matrix $\mathbf{n}^\sigma$ by a unitary transformation from the $|lm\rangle$ to $|l\alpha\rangle$ basis for 3d states,

$$\tau * \{n^\sigma_{lmm'}\} * \tau^{-1} = \{n^\sigma_{l\alpha}\}. \tag{3.14}$$

The total energy functional can then be written as

$$\begin{aligned} E &= E^{LDA} + \frac{1}{2}\sum_{\alpha,\alpha',\sigma} U(n_\alpha^\sigma - n^o)(n_{\alpha'}^{-\sigma} - n^o) \\ &+ \frac{1}{2}\sum_{\alpha,\alpha'\neq\alpha,\sigma} (U-J)(n_\alpha^\sigma - n^o)(n_{\alpha'}^\sigma - n^o). \end{aligned} \tag{3.15}$$

Here the double counting term E_{dc} is represented by n^o where $n^o = n_d/10$, and $n_d = \sum_{\alpha\sigma} n_\alpha^\sigma$. Using $V(\vec{r}) = \delta E/\delta n_\sigma(\vec{r})$, a simplified expression for the total LDA+U potential is finally obtained [13], i.e.,

$$V^{LDA+U}(\vec{r}) = V^{LDA}(\vec{r}) + V^U_{l\alpha\sigma}, \tag{3.16}$$

where

$$V^U_{l\alpha\sigma} = U\sum_{\alpha'}(n_{l\alpha'}^{-\sigma} - n^o) + (U-J)\sum_{\alpha'\neq\alpha}(n_{l\alpha'}^\sigma - n^o). \tag{3.17}$$

In a single-step spin-dependent calculation using the von Barth-Hedin LSDA functional, we first obtain $n_{l\alpha}^\sigma$. In this prescription, a prior knowledge of spin polarization of i-th atom $m_i = n_i^\uparrow - n_i^\downarrow$ is required. For Mn, Ni, and Cu we used m = 5, 2, and 1 respectively using Hund's multiplicity rule [72, 73] for free atoms which is often a good approximation for such systems.

The occupancy of the spin-up and -down states within the d-orbitals are thus determined in this single-step LSDA approach. Our calculations of spin-orbital occupancies of Mn and Ni d-states using this scheme are listed in Tables I and II. Thus we essentially start with a spin dependent ground state calculation and introduce spin and orbital dependence using Anisimov's prescription of Hubbard model. This LDA+U prescription is found to provide good agreement between the theory and experiment for the XAS of the TM compounds investigated here, although the self-consistent LDA+U treatment may be more desirable in other cases. The exchange parameter J is typically much smaller than U and variations were found [12] to be small over the transition metals; thus we have used J=0.9 eV for all cases. Using Eq. (12), (17), (18), and (21), we then correct our self-consistent potential and obtain a new potential $V(\mathbf{r},E)$.

Then using the above Hubbard corrected Hamiltonian, the wave functions $R_{l\alpha}(\mathbf{r},E)$ and $H_{l\alpha}(\mathbf{r},E)$ are recalculated as solutions of the Schrödinger equation inside the muffin-tin spheres. The orbital dependent phase shifts $\delta_{l\alpha}^\sigma(E)$ are obtained by matching to the free solutions (spherical Bessel functions) at the muffin-tin, and the scattering t-matrices are found,

$$t_{l\alpha}^\sigma = e^{i\delta_{l\alpha}^\sigma}\sin(\delta_{l\alpha}^\sigma). \tag{3.18}$$

Finally the multiple-scattering equations are resolved with these t-matrices yielding the the total Green's function $G = G^c + G^{sc}$, which now includes the Hubbard-U correction. With the addition of the state dependent Hubbard correction, the potential of Eq. (12) can correctly account for the well known discontinuity [13, 69] in exact DFT exchange-correlation potentials. However, such a term is absent from the conventional LDA and GGA approaches, rendering them incapable of including such

3.3 *ab initio* ***Hubbard parameters using constrained RPA***

A fully screened Coulomb interaction is given by,

$$W = [1 - vP]^{-1} v \tag{3.19}$$

Where P is the noninteracting polarization function,

$$\begin{aligned} P(\mathbf{r}, \mathbf{r}', \omega) = \sum_{i}^{occ} \sum_{j}^{unocc} & \psi_i(\mathbf{r}) \psi_i^*(\mathbf{r}') \psi_j^*(\mathbf{r}) \psi_j^*(\mathbf{r}') \\ & \times \left[\frac{1}{\omega - \varepsilon_j + \varepsilon_i + i0^+} - \frac{1}{\omega + \varepsilon_j - \varepsilon_i - i0^+} \right], \end{aligned} \tag{3.20}$$

where ψ_i, ε_i are the eigen states and eigen values of the system.

In a constrained RPA model one splits the polarization space into a localized (d-d polarization) P_d and rest of the system P_r $P = P_d + P_r$. P_d includes only d-d transition where $\{i, j\} \in \{\psi_d\}$. Now from the above equation ,

$$\begin{aligned} W = \frac{v}{1 - vP} &= \frac{v}{1 - vP_d - vP_r} \\ &= \frac{v}{(1 - vP_r)(1 - (1 - vP_r)^{-1} vP_d)} \\ &= \frac{U(\omega)}{1 - U(\omega) P_d} \end{aligned} \tag{3.21}$$

Where $U(\omega)$ is defined as

$$U(\omega) = \frac{v}{1 - vP_r(\omega)} \tag{3.22}$$

This frequency dependent $U(\omega)$ is the Coulomb interaction between d-d electrons screened by the rest of the system. One notices that $U(\omega)$ is also $\mathbf{r}, \mathbf{r}'$ dependent through the polarization function $P_r(\mathbf{r}, \mathbf{r}', \omega)$ If we take the static limit ($\omega = 0$) the U term is calculated as,

$$U = \int d^3r \, d^3r \, |\phi_{3d}(\mathbf{r})|^2 U(\mathbf{r}, \mathbf{r}') \, |\phi_{3d}(\mathbf{r}')|^2 \tag{3.23}$$

A numerical implementation of this method is currently under progress.

In our cRPA formulation [48] of the Hubbard parameter U we start with the standard expression of the RPA screened Coulomb interaction given by

$$W = \varepsilon^{RPA}(\mathbf{r},\mathbf{r}',\omega)^{-1} v, \tag{3.24}$$

where the RPA dielectric constant is

$$\varepsilon^{RPA}(\mathbf{r},\mathbf{r}',\omega) = 1 - v\chi^0(\mathbf{r},\mathbf{r}',\omega). \tag{3.25}$$

and the non-interacting response function is

$$\begin{aligned}\chi^0(\mathbf{r},\mathbf{r}',\omega) = \sum_i^{occ}\sum_j^{unocc} \psi_i(\mathbf{r})\psi_i^*(\mathbf{r}')\psi_j^*(\mathbf{r})\psi_j(\mathbf{r}') \\ \times\left[\frac{1}{\omega-\varepsilon_j+\varepsilon_i+i0^+} - \frac{1}{\omega+\varepsilon_j-\varepsilon_i-i0^+}\right].\end{aligned} \tag{3.26}$$

For correlated materials with narrow $3d$ or $4f$ bands, the response function can be divided into $\chi^0 = \chi_d^0 + \chi_r^0$. Here χ_d^0 contains only $3d-3d$ interaction, and can be obtained by limiting the summation to $i,j \in \psi_d$, and χ_r^0 is the response due to the remainder of the states. The effective Coulomb interaction in the narrow $3d$ bands can thus be identified [66] with the Hubbard parameter U:

$$U(\mathbf{r},\mathbf{r}',\omega) = [1 - v\chi_r^0(\mathbf{r},\mathbf{r}',\omega)]^{-1} v, \tag{3.27}$$

In the static limit ($\omega = 0$), we retain only the components of the effective interaction on the same atomic site by

$$U = \int_0^{R_n} d^3r d^3r' \left|\phi_{3d}(\mathbf{r})\right|^2 U(\mathbf{r},\mathbf{r}') \left|\phi_{3d}(\mathbf{r}')\right|^2, \tag{3.28}$$

where ϕ_{3d} is the localized $3d$ orbital of the embedded n-th atom with muffin-tin radius R_n. Following Stott and Zaremba [74], we write the $\chi^0(\mathbf{r},\mathbf{r}',\omega=0)$ in terms of the retarded single particle Green's function, i.e.,

$$\chi^0(\mathbf{r},\mathbf{r}',\omega=0) = -2\,\mathrm{Im}\int_{-\infty}^{E_\mathrm{F}} \frac{d\omega}{\pi} G^+(\mathbf{r},\mathbf{r}',\omega)G^+(\mathbf{r}',\mathbf{r},\omega). \tag{3.29}$$

This allows us to use our RSGF framework to calculate the response functions and thus the Hubbard interaction. Since the interactions in question are limited in spacial extent around a single atomic site, we make the approximation that the Coulomb interaction may be replaced by its spherical

average about that site, i.e., $v(\mathbf{r}-\mathbf{r}') = 1/r_>$, where $\boldsymbol{r}, \boldsymbol{r'}$ are relative to the center of the atomic site. In addition we neglect the angular momentum off-diagonal elements of the Green's function. This gives the following simple expression for the spherically averaged non-interacting response function,

$$\chi^0(r,r',\omega=0) = -2\,\mathrm{Im}\int_{-\infty}^{E_\mathrm{F}} \frac{d\omega}{\pi} \times \sum_L G^+_{LL}(\boldsymbol{r},\boldsymbol{r'},\omega) G^+_{LL}(\boldsymbol{r'},\boldsymbol{r},\omega). \tag{3.30}$$

We then find the RPA response function by inverting in real space. Within these same approximations, we may calculate the response function χ^0_r defined above by omitting the angular momentum states of interest (d- or f-states) from the sum in the above equation within a cutoff radius R_c. For example to find U for the d-states, we use the response function

$$\chi^0_r(r,r',\omega=0) = -2\,\mathrm{Im}\int_{-\infty}^{E_\mathrm{F}} \frac{d\omega}{\pi} \times \left[\sum_{L\neq d} G^+_{LL}(\boldsymbol{r},\boldsymbol{r'},\omega) G^+_{LL}(\boldsymbol{r'},\boldsymbol{r},\omega) \; + \; G^+_{dd}(\boldsymbol{r},\boldsymbol{r'},\omega) G^+_{dd}(\boldsymbol{r'},\boldsymbol{r},\omega)\Theta(r-R_c)\Theta(r'-R_c)\right], \tag{3.31}$$

where $\Theta(r)$ is a smooth cutoff function which goes to zero at $r = R_c$. Finally, U is found according to Eq. (3.27) and (3.28). These RSGF calculations have been used to find the RPA screened core-hole potential in calculations of XAS, and give reasonable results when compared to other theories (i.e., final state rule or Bethe Salpeter) and experiment [75]. We find that a cutoff radius $R_c = 1.5R_n$ gives reasonable values of U when compared to other calculations, and consistent band gaps when compared to experiment. Fig. 3.1 shows a comparison of our cRPA results for U with the cRPA and cLDA results of Aryasetiwan *et al.* [48]. Overall, the values are in reasonable agreement, and differences can be attributed to the choice of localized states and the approximations in the treatment of screening in our method.

3.4 Electron self-energy

Quasi-particle effects are key to an accurate treatment of excited state spectra [76], and hence require a good approximation for the electron self-energy for extended states. Current approximations for

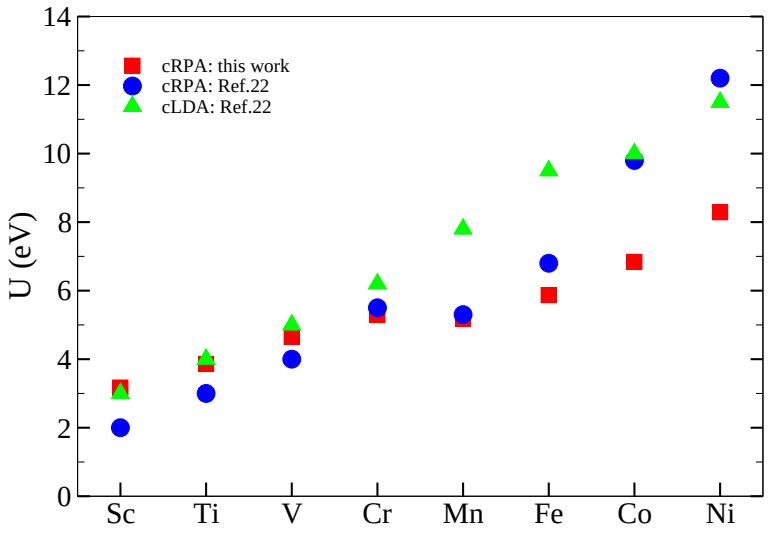

Figure 3.1: (Color online) Results of our cRPA calculations of U (red squares) for the 3d transition metals compared with the cRPA (blue circles) and cLDA (green triangles) calculations of Aryasetiawan [48]

.

the self-energy typically begin with Hedin's GW approximation (GWA) [10], which is formally given by

$$\Sigma^{GW} = iGW, \tag{3.32}$$

where G is the one electron Green's function, $W = \varepsilon^{-1}v$, is the screened-Coulomb interaction, and v the bare-Coulomb interaction. The FEFF9 code uses several approximations for the self-energy with the aim of providing efficient calculations of the energy dependent shift and broadening of spectral features over a wide energy range. The default, which is appropriate at high energies, is the Hedin-Lundqvist plasmon-pole model [10, 77], based on the homogeneous electron gas and a single-pole approximation to the dielectric function, which works well at energies above the plasmon energy ω_p. An extension which improves the self energy at lower energies is a many-pole model (MPSE), where the the dielectric function is represented as a weighted sum of poles matched to

calculations of the loss function in the long wavelength limit [78]. Efficiency is retained by assuming a simple plasmon dispersion relation for all poles in the representation of the dielectric function, and by using an electron gas Green's function. Thus our MPSE calculations are performed in a two step process: (i) The first step is to obtain a suitable approximation to the energy loss function $L(\omega) = -\mathrm{Im}[\varepsilon(\mathbf{q}=0,\omega)^{-1}]$; and (ii) The second is to extend the $q=0$ result to finite momentum transfer by representing it as a weighted sum of poles, which together conserve the overall oscillator strength,

$$L(q,\omega)^{-1} = -\mathrm{Im}[\varepsilon(q,\omega)^{-1}] = \pi \sum_i g_i \omega_i^2 \delta[\omega^2 - \omega_i(q)^2]. \tag{3.33}$$

Using this representation, and the electron gas approximation for the Green's function, the self-energy is a simple weighted sum of dynamic electron gas plasmon pole self energies, and a Hartree-Fock exchange term

$$\begin{aligned} \Sigma^{MP}(k,E) &= \Sigma_d(k,E) + \Sigma_{HF}(k), \\ \Sigma_d(k,E) &= \sum_i g_i \Sigma_d(k,E;\omega_i). \end{aligned} \tag{3.34}$$

The above formula is used to calculate an average quasi-particle correction $\Delta\Sigma^{MP}(k(E),E;\rho_{int})$, where the density used in the model is averaged over the interstitial (outside the muffin tins). More details of the MPSE model can be found in Kas *et al.* [78]

Although these models significantly improve quasi-particle calculations of unoccupied states at intermediate energies, they do not necessarily yield accurate band-gap corrections, and they do not have an appreciable effect on the localized states near the Fermi energy. Formally the two effects can be added by assuming that the Hubbard corrections are equivalent to the static Coulomb-hole/screened exchange (COHSEX) approximation for the localized states [1], and then treating only the dynamic self-energy corrections to the localized states with the model self-energy, i.e.,

$$\Sigma \approx \Sigma_{\mathrm{COHSEX}} + [\Sigma^{\mathrm{MPSE}} - \Sigma^{\mathrm{MPSE}}_{\mathrm{COHSEX}}]. \tag{3.35}$$

Here the first term is approximated using the Hubbard model while the second is calculated using our many-pole model. Delocalized states are treated with the many-pole model alone. However, since our many-pole model gives only small quasi-particle corrections to the localized states, we have neglected the last term $\Sigma^{\mathrm{MPSE}}_{\mathrm{COHSEX}}$ in our calculations. Thus in our implementation of the Hubbard

corrected self-energy, an effective spin and orbital dependent total correction $\Delta\Sigma^U$(E) is constructed as a simple addition of the plasmon-pole or many-pole self energy correction $\Delta\Sigma(E)$ and a Hubbard correction V^U_{lm} with calculated U, in order to correct the localized states near the Fermi level. Although such a construction can be done using self-consistent methods [79], here we use only a single-step calculation. Thus we define our total self-energy correction $\Delta\Sigma^U$ as

$$V(\mathbf{r},E) = V^{LDA}_{\sigma}(\mathbf{r}) + \Sigma^U(E), \tag{3.36}$$

$$\Delta\Sigma^U_{lm\sigma}(E) = V^U_{lm\sigma} + \Delta\Sigma^{MP}(E), \tag{3.37}$$

where each term has double counting subtracted. The orbital and spin-dependent Hubbard contribution to the potential $V^U_{lm\sigma}$ is calculated as described in the next section. We stress that the above prescription is an approximation; formally [52] one might expect some double-counting between the Hubbard terms and the many-pole self-energy. However, the effect of $\Sigma^{MP}(E)$ is most important at energies comparable to plasmon excitations while the behavior near the band-gaps is dominated by the Hubbard terms.

3.5 Density of States

3.5.1 Transition metal oxides: NiO and MnO

Transition metal oxides (TMOs) such as MnO and NiO are considered to be prototypes of strongly correlated Mott type insulators, with localized and partially filled *d*-electrons at the metal sites. These TMOs have NaCl like crystal structures, (Cubic O^5_h symmetry, and f_{m3m} space group). Below their respective Nèel temperatures, they all exhibit a rhombohedral distortion due to antiferromagnetic (AF) ordering, which is also known as exchange anisotropy [80]. We also examined the effects of such crystal distortions but they had negligible influence on the spectral features of interest here. In the following subsections we present results for the total and angular momentum projected DOS of MnO and NiO for a few values of U. For both compounds, the O K-edge XAS and XES are also calculated and compared with experimental results.

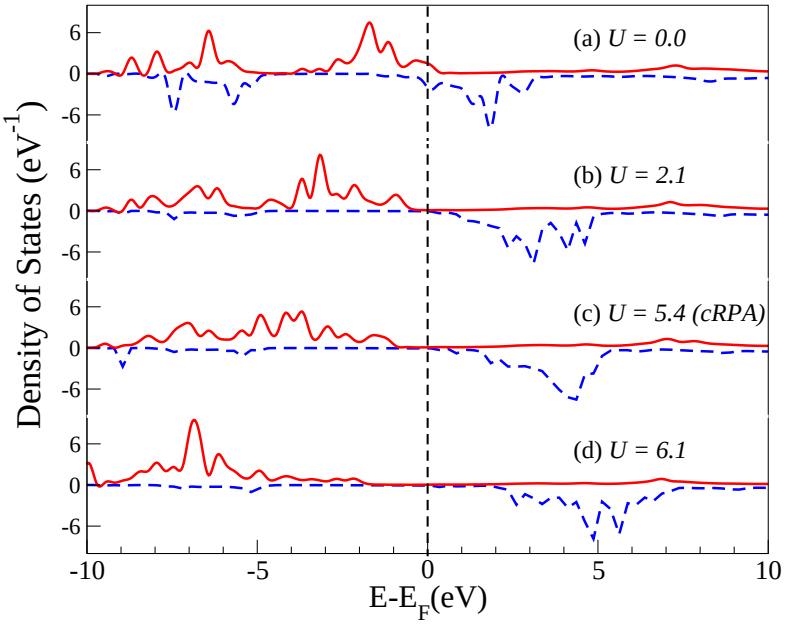

Figure 3.2: (Color online) U dependence on total DOS of MnO with spin up (solid red) and spin down (dashed blue) for different values of U: (a) LDA (U=0), (b) $U = 2.1$ eV, (c) $U = 5.4$ eV (cRPA), and (d) $U = 6.1$ eV; the vertical dashed line is at the Fermi energy.

MnO

In order to compare with room temperature experiment [67], we used an undistorted MnO crystal with $a = b = c = 4.4316$ Å and $\alpha = \beta = 90.624^\circ$ [81]. In this paper, we do not consider periodic magnetic effects; however, the single site moments are implicitly taken into account in our Σ^U(E) implementation. Our calculated cRPA U for MnO was found to be 5.4 eV.

In our FMS RSGF calculations for MnO, we used a cluster of 250 atoms, which was adequate to converge the spectrum, and a smaller cluster of 60 atoms for the self-consistent muffin-tin potentials.

For this system we calculated the O K-edge XES and XAS and the spin and angular momentum projected DOS about the Mn and O sites with and without Hubbard corrections. Fig. 3.2 shows a comparison of our calculated total ground state spin-resolved DOS of MnO to that calculated with different values of U including its cRPA value.

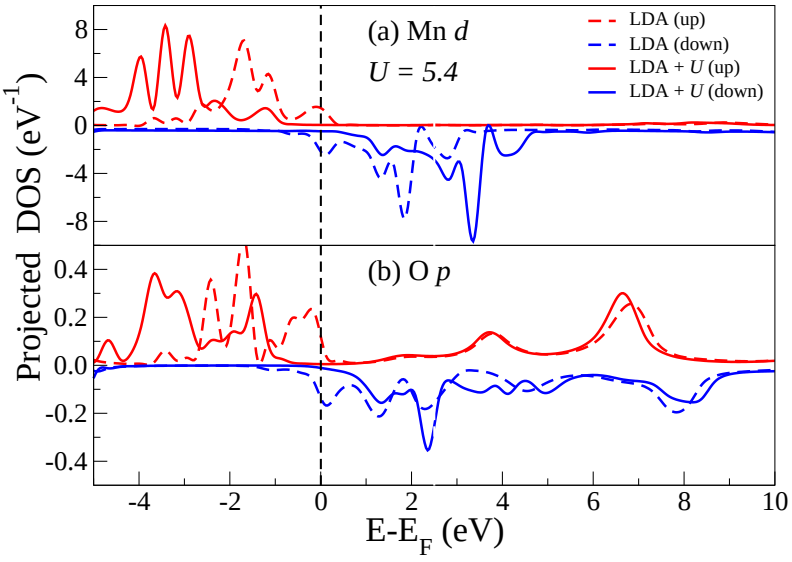

Figure 3.3: (Color online) Angular momentum projected l-DOS for Mn and O in MnO with $U = 0.0$ eV (dashed lines) and cRPA $U = 5.4$ eV (solid lines); Spin up and down DOS are above and below the horizontal axis correspondingly: (a) Mn d-DOS , and (b) O p-DOS; the vertical dashed line is at the Fermi energy.

While a calculation with a MPSE underestimates an insulating gap (dashed blue line in Fig. 3.2(a)), a gap close to that observed in experiment is obtained using our calculated Hubbard correction with $U = 5.4$ eV. When this Hubbard correction is applied to Mn d-states, the unoccupied spin down states are shifted by +1.6 eV, as seen in Fig. 3.3(a). The O p-states (Fig. 3.3(b)) near E_F are strongly hybridized with Mn d-states (Fig. 3.3(a)); thus a gap is also seen in the O p-DOS. However, the O p-states around 6-8 eV only hybridize with Mn s-p-states (not shown) and are not affected by the Hubbard correction. In Table (I) we present the spin-orbital occupancies of the localized Mn d-states and the corresponding Hubbard correction for $U = 5.4$ and $J = 0.9$ eV.

In order to compare with room-temperature experiments [67] we have accounted for the rhombohedral distortion of NiO crystal along the [111] direction [83, 84]. Our methods for calculating electronic structures of NiO are similar to those for MnO, except for the input NiO crystal struc-

Table 3.1: Mn d-state parameters ($U = 5.4$ eV; $J = 0.9$ eV)

l	α	$n_{l\alpha}$	$n^{\uparrow}_{l\alpha}$	$n^{\downarrow}_{l\alpha}$	$V^{\uparrow}_{l\alpha}$(eV)	$V^{\downarrow}_{l\alpha}$(eV)
2	α_1	0.94	0.85	0.09	-0.32	3.11
2	α_2	0.90	0.81	0.09	-0.29	3.11
2	α_3	0.93	0.83	0.10	-0.30	3.12
2	α_4	1.10	0.99	0.11	-1.00	3.12
2	α_5	1.09	0.98	0.11	-1.00	3.15

Table 3.2: Ni d-state parameters ($U = 8.0$ eV; $J = 0.9$ eV)

l	α	$n_{l\alpha}$	$n^{\uparrow}_{l\alpha}$	$n^{\downarrow}_{l\alpha}$	$V^{\uparrow}_{l\alpha}$(eV)	$V^{\downarrow}_{l\alpha}$(eV)
2	α_1	1.21	0.91	0.30	-0.72	3.95
2	α_2	1.30	0.95	0.35	-1.40	4.02
2	α_3	1.86	0.95	0.91	-1.40	-0.52
2	α_4	1.86	0.95	0.91	-1.40	-0.52
2	α_5	1.88	0.96	0.92	-1.43	-0.53

ture, where we have used a slightly distorted crystal with $a = b = 4.168$ Å, $c = 4.166$ Å, and $\alpha = \beta = 90.055^{\circ}, \gamma = 90.082^{\circ}$. With the Hubbard correction, the best agreement with the experimental XAS was again obtained with our calculated U = 8.0 eV. Fig. 3.4 shows the gap opening in the spin projected total DOS of NiO for other values of U beside cRPA U.

The O p-states in NiO are also strongly hybridized with localized Ni d-states as in MnO. The spin-orbital occupancies and corresponding Hubbard potential for the Ni d-states are listed in Table II. The results are presented in Fig. 3.5.

We have also compared in Fig. 3.6 our total DOS for MnO calculated with our cRPA U = 5.4 and J = 0.9 eV, with that of Ref. [1] calculated with $U = 5.4$ and $J = 0.0$.

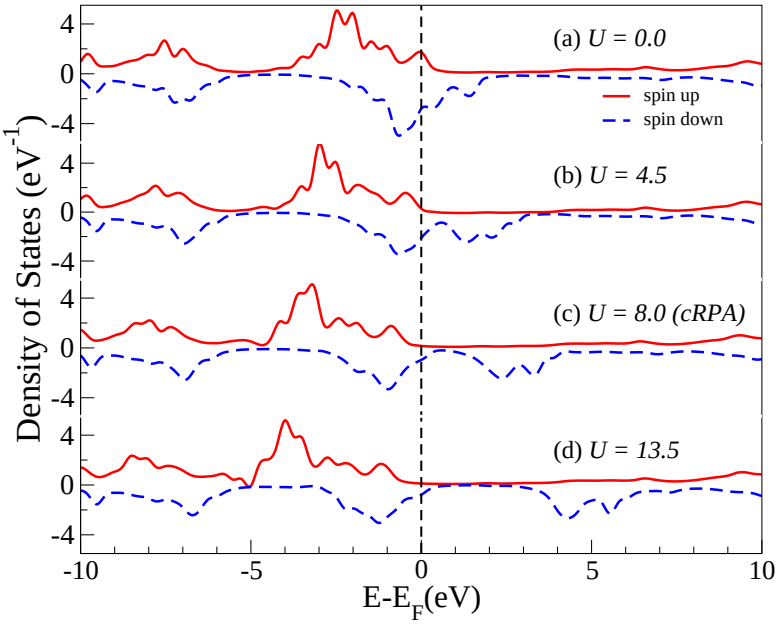

Figure 3.4: U dependence on total DOS of NiO with spin up (solid red) and spin down (dashed blue) for different values of U: (a) $U = 0$ eV, (b) $U = 4.5$ eV, (c) $U = 8.0$ eV (cRPA), and (d) $U = 13.5$ eV; the vertical dashed line is at the Fermi energy.

Despite differences in methodology and the fact that the gap Δ can only be determined approximately with a finite cluster RSGF approach, both methods are in reasonable agreement.

3.5.2 High T_c Cuprate: LSCO

Understanding the doping dependence of high T_c cuprates has become an interesting challenge in recent years. LSCO ($La_{2-x}Sr_xCuO_4$), which is a prototype of hole-doped cuprates, exhibits metallic and paramagnetic behavior at high doping [22], and becomes an AF insulator when undoped. Between these limits, the system goes through a superconducting phase at the doping concentration of about $x = 0.15$. A good description of the electronic structure in its insulating phase is important to understand the exotic doping dependent phase transformations in such systems.

In the over-doped region with $x > 0.2$, LSCO becomes paramagnetic, and is well described by a self-energy approximation constructed from a single band Hubbard model [22]. A Fermi-liquid

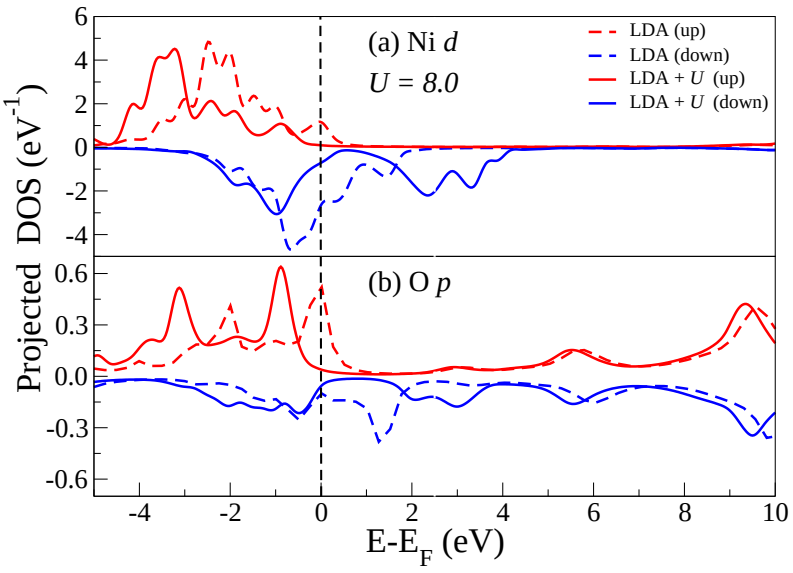

Figure 3.5: Angular momentum projected l-DOS for Ni and O in NiO with $U = 0.0$ eV (dashed line), and $U = 8.0$ eV (solid line); Spin up an down DOS are above and below the horizontal axis correspondingly: (a) Ni d-DOS (b) O p-DOS; the vertical dashed line is at the Fermi energy.

description thus becomes more appropriate for such systems. As doping is reduced, correlation effects due to localized states become more important, and the implementation of Hubbard U to the d electrons on the Cu sites is seen to open a gap. A gap correction using $\Sigma^U(E)$ on the partial d-DOS of Cu and p-DOS of O is shown in Fig. 3.7 and Fig. 3.8.

3.6 X-ray spectroscopy

3.6.1 MnO and NiO

Bulk sensitive XES and XAS for TM oxides often provide a good assessment of the band gap in insulators [67]. In Fig. 3.9 we compare our Σ^U calculation of the O K-edge XAS and XES in MnO with experiment [67]. Fig. 3.9 shows the result of our spin resolved FMS calculation obtained with both Hubbard and MPSE corrections (b), compared to results with no Hubbard correction (a), and experiment (c). The XAS calculation was done in the presence of a screened core-hole at the absorb-

Table 3.3: Calculated Hubbard parameter U and gap Δ of MnO, NiO, and LSCO.

Materials	MnO	NiO	LSCO
U (this work)	5.4	8.0	10.0
U (Ref. [1])	4.7	5.2	
U (Ref. [12])	6.9	8.0	
Δ (this work)	3.9	4.4	1.4
Δ (Ref. [1])	2.6	3.8	
Δ (Expt. [67, 82])	4.1	4.3	1.8

ing O atom in MnO while for XES no core-hole was included; these approximations are consistent with the final-state- and initial-state rules for XAS and XES respectively. Our Hubbard corrected self-energy blue shifts the first excitation at around 534 eV, while the rest of the unoccupied states, including the main peak at 540 eV, are unchanged. In XES, the highest occupied state moves down by 3 eV which is now on the other side of the second vertical dashed line in Fig. 3.9. These distinct, opposite shifts of the highest occupied and first unoccupied states are due to the strong hybridization of O *p*-states with the localized Mn *d* states. This can also be identified in Fig. 3.3(b) as the lower (LHB) and upper Hubbard bands (UHB) at around -2 and 2 eV.

For NiO our GW plasmon-pole calculation in Fig. 3.10(a) exhibits considerable overlap between the O K-edge XAS and XES spectra, due to the underestimated insulating gap. However, the introduction of the Hubbard interaction ($U = 8.0$ eV) increases the gap, causing the pre-peaks of both the XAS and XES to split further apart, as shown in Fig. 3.10(c). For comparison, we also show a WIEN2K LDA+U calculation in Fig. 3.10(a) for the O K-edge EELS in NiO [85].

Aligning the first peak of this calculation with experiment [Fig. 3.10(d)], we observe an underestimation of the high energy peaks at around 544 eV. These peaks can be attributed to O *p*-states which are strongly hybridized with Ni *s*- and *p*-states. Similar behavior has been found in NiO [1, 86], and other TM compounds [85, 87]. We attempted to improve these results by using a GW

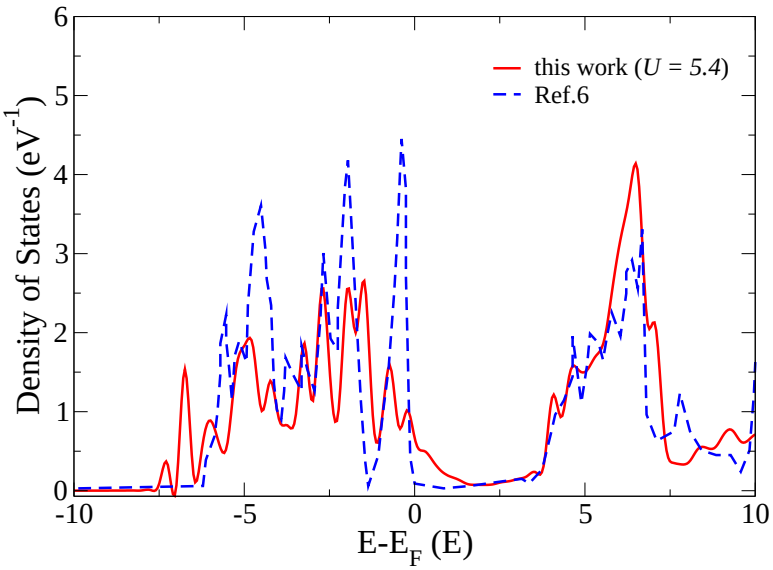

Figure 3.6: MnO total DOS with our RSGF cRPA calculated U = 5.4 and J = 0.9, and GW@LDA+U calculations [1] with U = 5.4 J = 0.0 (dashed blue line); the vertical dashed line is at the Fermi energy.

MPSE [78] for NiO, while applying the Hubbard correction to the Ni d-states. This MPSE model includes a more realistic treatment of inelastic losses than the plasmon pole model, and yields improved agreement with experiment, as seen in Fig. 3.10(c). These results demonstrate that an accurate treatment of the delocalized s-p-states can also be important in such systems. Thus in order to achieve good agreement between theoretical and experimental spectral features, a systematic consideration of excited state properties including both localized- and delocalized states is important.

3.6.2 High T_c cuprate: LSCO

In Table III we compare our cRPA calculated U and estimated XAS-XES gap Δ with gap values reported by others. Our values of U for MnO and NiO are in reasonable accord with experiment and roughly comparable to those of Ref. citePatrick2010,Anis91. Likewise our calculated values of Δ are in good agreement with experiment for MnO and NiO, but underestimated by 0.5 eV for LSCO.

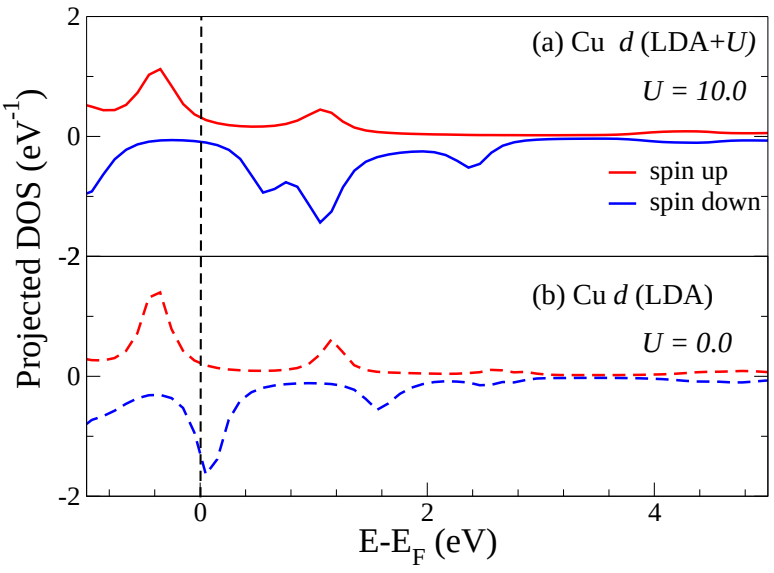

Figure 3.7: (a) Cu spin up(solid red) and down(solid blue) d-DOS of LSCO with cRPA calculated value $U = 10.0$; (b) Cu spin up and down d-DOS for $U = 0.0$ (dashed red and blue). The vertical dashed line is at the Fermi energy.

For LSCO our O K-edge XAS for $\Sigma^{MP}(E)$ and Σ^{U} with U = 10.0 eV are compared with experimental results in Fig. 3.11. Our result with cRPA calculated U agrees well with the undoped LSCO experiment, while the over-doped LSCO system is reasonably reproduced by a GW MPSE calculation alone (U = 0). This result is not surprising, since in the absence of the Hubbard term, the LDA does not predict a correlation gap. As a result the system is predicted to be metallic, mimicking the over-doped ($x \approx 0.3$) paramagnetic phase of $La_{1-x}Sr_xCuO_4$. A complete description of the doping dependence of spectral features from over-doped ($x = 0.3$) to undoped ($x = 0.0$), requires a dynamical self-energy correction that incorporates pseudo-gap, superconducting, and Fermi-liquid physics [44].

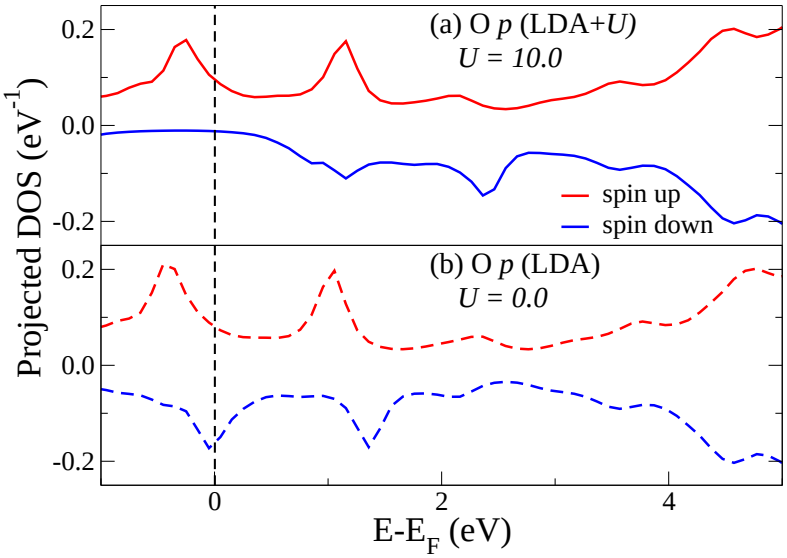

Figure 3.8: (a) O spin up (solid red) and down (solid blue) p-DOS of LSCO with cRPA $U = 10.0$; (b) O spin up (dashed red) and down (dashed blue) p-DOS with $U = 0.0$. The vertical dashed line is at the Fermi energy.

3.7 Conclusion

We have implemented Hubbard model corrections within an LDA+U approach, using a rotationally invariant formalism and an extension of the RSGF method for calculations of excited state electronic structure and x-ray spectra of correlated materials. Our approach also builds in a model GW self-energy. Both Hubbard-model and dynamic self-energy effects are incorporated in an effective self-energy correction $\Delta\Sigma^U$. The Hubbard parameter U is estimated using the cRPA method, again within the RSGF formalism. The additional GW self-energy is approximated by a many-pole model based on the electron gas Green's function and the loss function in the long-wavelength limit. These considerations lead to a RSGF/$\Delta\Sigma^U$ approach which provides an efficient way to account for correlation effects on x-ray spectra of complex materials. The approach is advantageous for aperiodic systems since it does not rely on symmetry or periodicity. The method was tested on several cor-

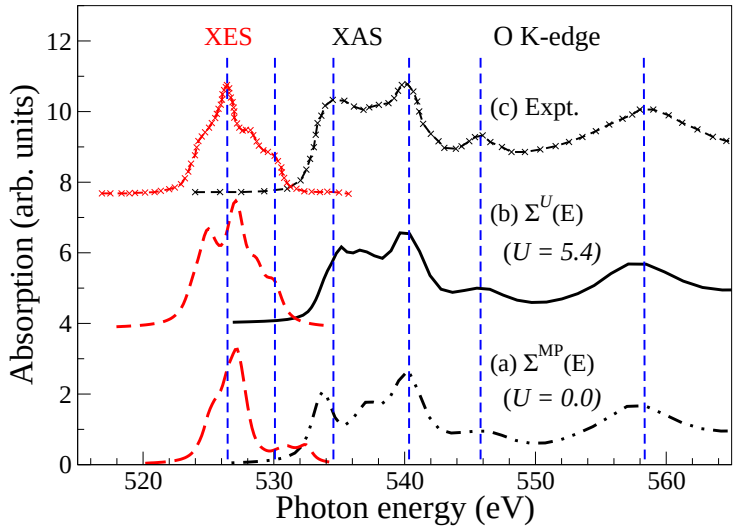

Figure 3.9: O K-edge XAS (black) and XES (red) in MnO. (a) QP FEFF calculation using our MPSE model $\Sigma^{MP}(E)$, (b) $\Sigma^{U}(E)$ with $U = 5.4$, and (c) experiment [67]. The vertical dashed lines are a guide to the eye.

related materials and found to yield reasonable agreement for the observed experimental band gap as well as the XAS and XES of MnO and NiO. However, the agreement with experiment is less accurate for more complex systems such as LSCO. This suggests the need in such systems for a more comprehensive treatment of superconducting and pseudo-gap physics that incorporates doping dependence in the under-doped regime [44, 53]. Overall, however, our method explains the key features of the excited state electronic structure and spectra of many strongly correlated systems, and in particular the correlation gap. Finally we note that our approach is limited to the quasi-particle approximation and Hubbard model corrections, while inelastic many-body effects such as satellites and charge-transfer excitations are currently neglected.

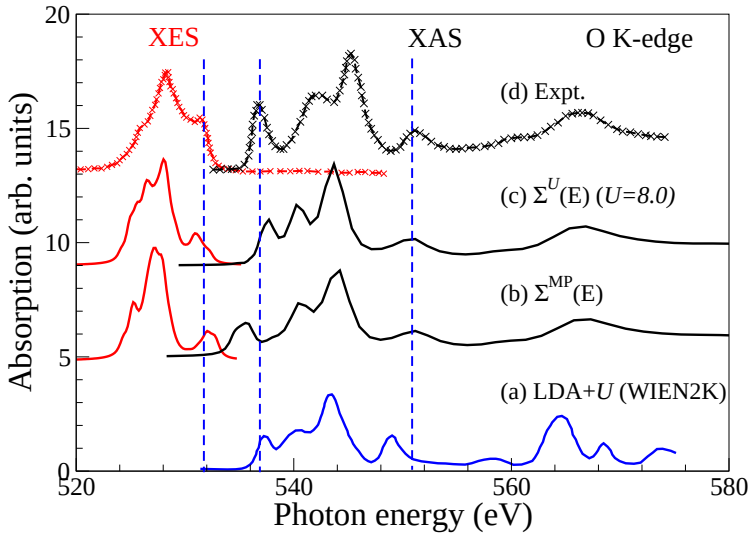

Figure 3.10: NiO O K-edge XAS (black) and XES (red) experiment vs theory: (a) LDA+U calculation [85] for O 1s EELS using WIEN2K; (b) FEFF GW plasmon-pole (PP) self-energy; (c) FEFF $\Sigma^U(E)$ with *ab initio* Hubbard correction with cRPA $U = 8.0$ eV; and (d) Experiment [67]. The vertical dashed lines are a guide to the eye.

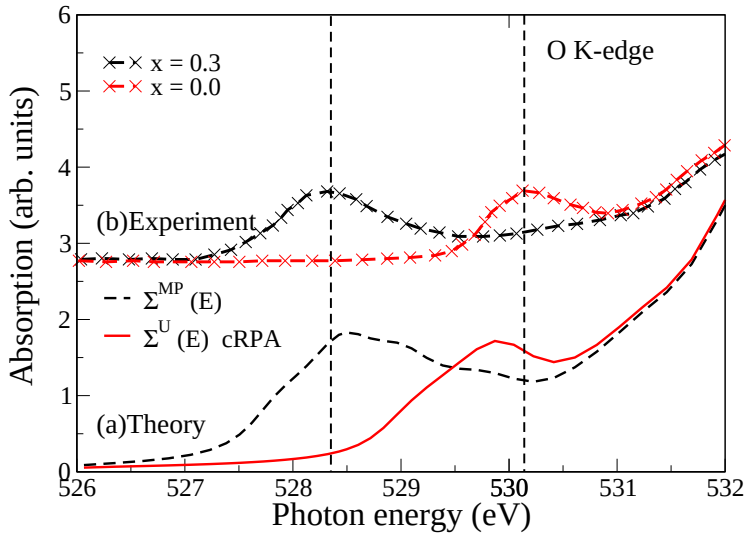

Figure 3.11: O K-edge XAS for LSCO: (a) our $\Sigma^U(E)$ calculation with cRPA $U = 10.0$ (red) and GW only (black); (b) experimental K-edge XAS for undoped ($x = 0.0$, red) and over-doped ($x = 0.3$, black) LSCO, and the vertical dashed lines are a guide to the eye.

Chapter 4

X-RAY ABSORPTION NEAR-EDGE SPECTRA OF OVERDOPED LSCO

In this chapter we present results for realistic modeling of the x-ray absorption near edge structure (XANES) of the overdoped high-T_c superconductor $La_{2-x}Sr_xCuO_4$ in the hole doping range x = 0.20-0.30. Our computations are based on a real-space Green's function approach in which strong-correlation effects are taken into account in terms of a doping-dependent self-energy. The predicted O K-edge XANES is found to be in good accord with the corresponding experimental results in this overdoped regime. We find that the low energy spectra are dominated by the contribution of O atoms in the cuprate planes, with little contribution from apical O atoms, and are well-described by a fully screened core-hole. The work presented in this chapter is published in Physical Review B[22].

4.0.1 Outline of this chapter

Starting with a general introduction in section 4.2 we discussed the background theory in section 4.3. In subsection 4.3.1 we briefly discussed the RSGF code FEFF and our implementation of a doping dependent self-energy. This self-energy was constructed by Bansil *et al.* [19]. Some fundamental aspects of this construction is discussed in subsection 4.3.2. We discuss our results and compare with experiment in section 4.4.

4.0.2 Key observation

Our RSGF calculation with the implemented doping dependent self-energy correction qualitatively reproduces the trend of the pre-edge feature in overdoped LSCO as found experimentally by Peets *et al.* [88].

4.1 Introduction

In their undoped parent compounds, high-T_c cuprate superconductors are antiferromagnetic insulators which are characterized by a gap driven by strong electron correlations. For this reason these materials are commonly referred to as Mott insulators. Strong correlation effects weaken with increased electron or hole doping, eventually yielding a metallic state. In $La_{2-x}Sr_xCuO_4$ (LSCO), for example, at a hole doping level of x $\sim$ 0.16, a paramagnetic state emerges and the material appears to recover Fermi liquid properties. However, despite over two decades of intense experimental and theoretical effort, the underlying principles governing how a Mott insulator transitions into a Fermi-liquid with doping are still not well understood [46]. The answer seems to be hidden within the mechanisms through which the quasiparticle spectral weight passes from the insulating Mott-Hubbard bands to the in-gap states near the Fermi level. In electron doped cuprates, the Mott gap and the associated lower Hubbard band can be directly probed by photoemission spectroscopy. In the hole doped cuprates, on the other hand, this gap lies above the Fermi energy, so that techniques sensitive to empty states within a few eV above the Fermi energy must be deployed. Accordingly, light scattering techniques have been used, including optical, resonant inelastic x-ray scattering (RIXS), and x-ray absorption near edge spectroscopy (XANES) which probes the density of states (DOS) of empty states above the Fermi energy via excitations from core levels [46, 89, 90].

The purpose of this study is to model the XANES spectrum of LSCO realistically, as an exemplar hole-doped cuprate, and to compare and contrast our theoretical predictions with available experimental data. The analysis is carried out using a real-space Green's function (RSGF) approach as implemented in the FEFF9 code [76, 91]. Strong correlation effects on the electronic states near the Fermi energy (E_F) are incorporated by adding additional self-energy corrections to the one-particle electron and hole propagators. We concentrate in this initial study on the overdoped system because the cuprates are in a paramagnetic state in this doping range. Consequently the treatment of correlations effects is simpler, due to the absence of the pseudogap in the electronic spectrum. In LSCO, the pseudogap is found to vanish near $x = 0.20$ [46]. We start with a generic plasmon-pole self-energy and then dress our calculations with a doping dependent paramagnetic self-energy Σ obtained within the self-consistent quasiparticle-GW (QP-GW) scheme [46, 54]. Here GW refers to the Hedin approximation to the self energy $\Sigma = iGW$, where G is the one-particle Green's func-

tion and W the screened Coulomb interaction [10]. This self-energy has been shown to capture key features of strong electronic correlations in various cuprate spectroscopies including ARPES [55], RIXS [92], optical [46] and neutron scattering [89], in good agreement with experiments in both electron and hole doped systems.

Many key properties of cuprates, including the physics of superconductivity, involve hybridized Cu $d_{x^2-y^2}$ and O $p_{x,y,z}$ orbitals near the Fermi energy E_F. Thus the natural choices for the probe atoms in which the incoming x-ray excites a core-hole are Cu and O. Since dipole selection rules do not allow K-edge excitations in Cu atoms to couple to d-bands, we focus here mainly on the O K-edge XANES. This edge may be expected to reflect doping dependent changes in the near E_F spectrum through its sensitivity to the O-p states. In O K-edge XANES experiments on LSCO [93–95], two 'pre-peaks' have been observed to vary with Sr concentration. Our analysis indicates that the energy separation between these two peaks, which is comparable to the optical gap in the insulating phase [46], is associated with the Mott gap [3]. In particular, the upper XANES peak corresponds to the empty states of the upper Hubbard band, and the lower peak to empty states in the lower Hubbard band resulting from hole doping. With increasing doping, the lower peak, which is absent for x = 0.00, starts to grow while the upper peak loses intensity. In the overdoped regime, the lower peak reaches a plateau [88], while the intensity of the upper peak is substantially suppressed.

In order to assess effects of core-hole screening, we have also calculated the Cu K-edge XANES, again using the same RSGF approach [76, 91]. In this connection, two different core-hole models were considered: (i) Full screening, i.e., without a core-hole as in the "initial state rule" (ISR) [96], and (ii) RPA screening as is typically used in Bethe-Salpeter equation (BSE) calculations [97]. Both of these core-hole models reasonably reproduce the experimental XANES of the O K-edge in the pre-peak region in overdoped LSCO.

The remainder of this article is organized as follows. Introductory remarks in section I are followed by a brief account of the methodological details of the RSGF formalism in section IIA, and of the QP-GW self-energy computations in section IIB. XANES results based on the plasmon-pole self-energy are discussed in section IIIA, while results based on doping dependent QP-GW self-energies are taken up in section IIIB. Finally section IV contains a summary and conclusion.

4.2 Fermi-liquid description of $La_{2-x}Sr_xCuO_4$

4.2.1 Real-space Green's function formulation for High T_c cuprates

Here we briefly outline the real-space Green's function multiple-scattering formalism underlying the FEFF code. More detailed accounts are given elsewhere [76, 91]. The quasi-particle Green's function for the excited electron at energy E is defined as

$$G(E) = [E - H - \Sigma(E)]^{-1}. \tag{4.1}$$

Here H is the independent particle (i.e., Kohn-Sham) Hamiltonian,

$$H = \frac{p^2}{2} + V, \tag{4.2}$$

with V being the Hartree potential plus a ground state exchange-correlation density functional, which in FEFF9 is taken to be the von Barth-Hedin functional [30]. Here Hartree atomic units ($e = \hbar = m = 1$) are implicit. This Hamiltonian together with the Fermi-energy E_F are calculated self-consistently using the RSGF approach outlined below. In Eq. (1) the quantity $\Sigma(E)$ is the energy-dependent one-electron self-energy. In this work we use a GW self-energy designed to incorporate the strong-coupling effects in cuprates, as discussed further in section IIB below.

In the RSGF approach it is useful to decompose the total Green's function $G(E)$ as

$$G(E) = G^c(E) + G^{sc}(E), \tag{4.3}$$

where $G^c(E)$ is the contribution from the central atom where the x-ray is absorbed and $G^{sc}(E)$ is the scattering part. For points within a sphere surrounding the absorbing atom the angular dependence of the real space Green's function can be expressed using spherical harmonics as

$$G(\mathbf{r}, \mathbf{r}', E) = \sum_{L,L'} Y_L(\hat{\mathbf{r}})\, G_{L,L'}(r, r', E)\, Y^*_{L'}(\hat{\mathbf{r}}'). \tag{4.4}$$

Here, Y_L is a spherical harmonic with $L = (l, m)$ denotes both orbital and azimuthal quantum numbers. The physical quantity measured in XANES for x-ray photons of polarization $\hat{\boldsymbol{\varepsilon}}$ and energy $\hbar\omega = E - E_c$ is the x-ray absorption coefficient $\mu(\omega)$, where E_c is the core electron energy, and E is the energy of the excited electron. The absolute edge energy is given by $E_F - E_c$, where E_F is the Fermi level. The FEFF code calculates both $\mu(\omega)$, the site- and l-projected DOS $\rho_l^{(n)}(E)$ at site

n and the Fermi energy (E_F) self-consistently. These quantities can be expressed in terms of the Green's function in Eq. (4) as

$$\mu(\omega) \propto -\frac{2}{\pi}\mathrm{Im}\left\langle\phi_0|\hat{\varepsilon}.\mathbf{r}G(\mathbf{r},\mathbf{r}',\omega)\hat{\varepsilon}.\mathbf{r}'|\phi_0\right\rangle, \tag{4.5}$$

and

$$\rho_l^{(n)}(E) = -\frac{2}{\pi}\mathrm{Im}\sum_m\int_0^{R_n} G_{L,L}(r,r,E)\,r^2\,dr\,, \tag{4.6}$$

respectively. Here $|\phi_0\rangle$ is the initial state of the absorbing atom and R_n is the Norman radius [29] around the nth atom, which is analogous to the Wigner-Seitz radius of neutral spheres, and the factor 2 accounts for spin degeneracy.

4.3 Doping dependent self-energy in single-band Hubbard model

In the optimal or overdoped regime of present interest, cuprates do not exhibit any signature of a symmetry-breaking order parameter, and thus the quasiparticle dispersion can be well-described with a paramagnon-renormalized one band Hubbard model [46]. The details of the related self-energy are given in Markiewicz *et al.* [54] and are summarized here for completeness.

In our QP-GW approach, we start with a tight-binding single band bare dispersion $\xi_{\mathbf{k}}$ where the parameters are obtained by fitting to the first-principles LDA dispersion [98]. The values of the tight-binding parameters used in LSCO are from Das *et al.* [46] The LDA dispersion is then self-consistently dressed by the full spectrum of spin and charge fluctuations treated at the RPA level. The susceptibility can be written in terms of the bare susceptibility $\chi_0(\mathbf{q},\omega)$ as

$$\chi(\mathbf{q},\omega) = \frac{\chi_0(\mathbf{q},\omega)}{1-\bar{U}\chi_0(\mathbf{q},\omega)}. \tag{4.7}$$

Here $\bar{U}$ is the renormalized Hubbard U value. The imaginary part of the RPA susceptibility provides the dominant fluctuation interaction to the electronic system, which can be represented by $W(\mathbf{q},\omega) = (3/2)\bar{U}^2\chi''(\mathbf{q},\omega)$. The resulting self-energy correction to the LDA dispersion within the GW approximation is

$$\begin{aligned}\Sigma(\mathbf{k},\omega) &= Z\sum_{\mathbf{q}} W(\mathbf{q},\omega')\Gamma(\mathbf{k},\mathbf{q},\omega,\omega') \\ &\times \left[\frac{f(\bar{\xi}_{\mathbf{k}-\mathbf{q}})}{\omega+\omega'+i\delta-\xi_{\mathbf{k}-\mathbf{q}}} + \frac{1-f(\bar{\xi}_{\mathbf{k}-\mathbf{q}})}{\omega-\omega'+i\delta-\xi_{\mathbf{k}-\mathbf{q}}}\right],\end{aligned} \tag{4.8}$$

where $f(\xi)$ is the Fermi function and Γ is the vertex correction defined below.

Different levels of self-consistency within the GW scheme involve different choices for χ_0 and dispersion $\bar{\xi}_{\mathbf{k}}$. Within our QP-GW scheme, the Green's function entering into the χ_0 bubble is renormalized by an approximate renormalization factor Z which is evaluated self-consistently. The corresponding vertex correction is taken within the Ward identity $\Gamma = 1/Z$, and $\bar{\xi}_{\mathbf{k}} = Z(\xi_{\mathbf{k}} - \mu)$ is the renormalized dispersion where μ is the chemical potential. The renormalized band is employed to calculate the full spectrum of spin susceptibility:

$$\chi_0(\mathbf{q},\omega) = -Z\sum_{\mathbf{k}} \frac{f(\bar{\xi}_{\mathbf{k}}) - f(\bar{\xi}_{\mathbf{k}+\mathbf{q}})}{\omega + i\delta + \xi_{\mathbf{k}} - \xi_{\mathbf{k}+\mathbf{q}}}. \tag{4.9}$$

The doping dependence of U is discussed in Das *et al.* [46] and Ankudinov *et al.* [89] A single, universal function $\bar{U}(x)$ is found to reasonably describe a number of different spectroscopies including photoemission, optical spectra [46] and the present XANES. This doping

4.4 X-ray spectroscopy of overdoped LSCO

In subsection IIIA below, we discuss O and Cu K-edge XANES using a generic GW plasmon-pole self-energy and RPA core-hole screening, but without the self-energy correction arising from strong correlation effects. Subsection IIIB examines doping-dependent effects of self-energy corrections on the O K-edge XANES.

4.4.1 XANES without self-energy corrections

Since K-edge XANES probes the site-dependent p density of states (p-DOS), we consider first the projected p-DOS from O and Cu sites near E_F as obtained using the FEFF code. The low-temperature orthorhombic crystal structure with space group Bmab was used [100]. It is important to note that the structure involves two inequivalent O-atoms with different chemical environments, namely, the O-atoms in the cuprate planes (O_{pl}), and the apical O-atoms (O_{ap}) which lie in the La-O planes. The projected densities of states on the two distinct O-atoms and the Cu-atoms are shown in Fig. 4.1. Also shown for reference is the projected d-DOS from Cu-sites, even though as already pointed out K-edge excitations do not couple with the d angular momentum channel. The p-DOS from the O-atoms in the cuprate planes (middle curve) is seen to display the structure marked by arrows, arising from the hybridization of localized Cu d and O p orbitals, which is related

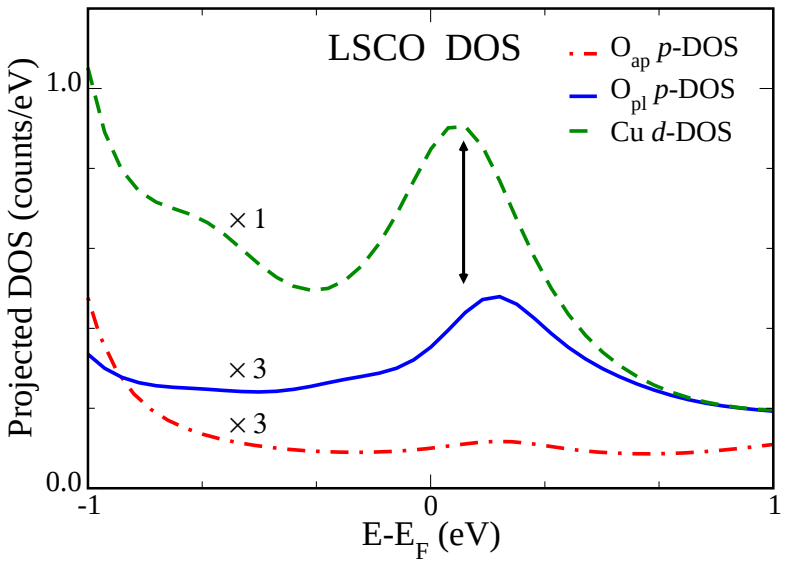

Figure 4.1: (color online) Site- and *l*-projected DOS in doped LSCO, $x = 0.30$. Cu-*d* (green dashed line), O_{pl}-*p* (blue solid line) and O_{ap}-*p* (red dashed-dotted line) DOS are shown. Note scaling of the lower two curves by a factor of 3. Arrows mark the structure related to the van Hove singularity in the hybridized Cu-O bands discussed in the text.

to the van Hove singularity (VHS) near E_F in the band structure of LSCO. The O_{ap} contribution is seen to be quite small and structureless within a ± 0.75 eV energy range of E_F, although a weak replica of the VHS peak suggests a small hybridization of the apical and in-plane oxygens. This implies that O K-edge XANES pre-peak is mainly associated with unoccupied electronic states from atoms lying in the Cu-O planes. Notably, the Cu-*p* DOS (not shown) in the near E_F energy window of Fig. 4.1 is also quite small and structureless and becomes significant only several eV above E_F. The experimental evidence for the aforementioned features of XANES spectra has been discussed previously by several authors [93–95]. The treatment of core-hole screening in the O K-edge spectrum is addressed in Fig. 4.2, where we compare the experimental results from overdoped LSCO with computations using two different core-hole screening models. The computed XANES spectrum using a fully screened hole (blue solid curve) is seen to be in good accord with the results

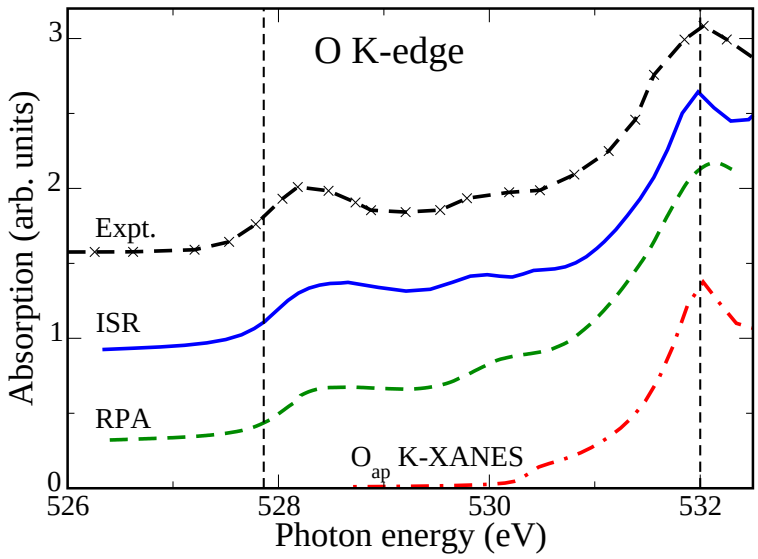

Figure 4.2: (color online) Theoretical and experimental [99] O K-edge XANES spectra in overdoped LSCO (x=0.30). Computations where the core-hole is fully screened, i.e. using the initial state rule (ISR) (blue solid line) are compared with results based on RPA screened core-hole (green dashed line) and experiments (dashed crossed line). The vertical dashed line at 527.8 eV marks the approximate edge energy (i.e., Fermi level) which is sensitive to doping. A vertical dashed line is also drawn through the feature at 532 eV. This feature is due to the apical O, as shown by the red dashed-dotted line, calculated with the ISR.

of the RPA screened hole (green dashed curve), although the intensity of the feature at 532 eV differs somewhat in the ISR and RPA results. All three curves in Fig. 4.2 show the presence of the pre-edge peak around 528.5 eV, a weaker pre-edge feature around 530 eV, and the prominent peak at 532 eV, which is due to the apical oxygen, as demonstrated by the calculated partial absorption, red (dashed-dotted) curve. Fig. 4.3 presents results along the preceding lines for the Cu K-edge XANES in undoped LSCO. Since the Cu K-edge probes p-states which are only weakly correlated, it provides a useful check of our theoretical method for the case of weak-correlation. The results in Fig. 4.2 and Fig. 4.3 clearly indicate that the K-edge spectra are not sensitive to the core-hole screening model, as both the RPA and the ISR give results in reasonable agreement with experiment.

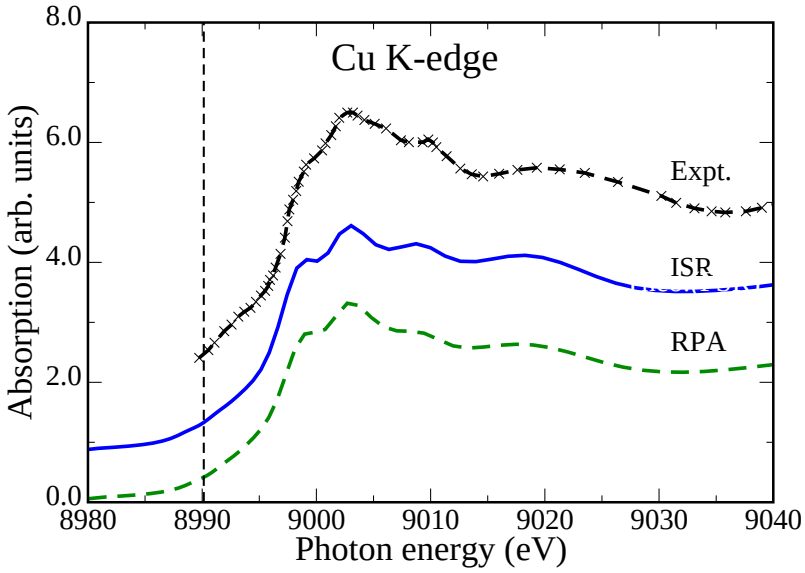

Figure 4.3: (color online) Theoretical and experimental [21] Cu K-edge XANES spectra in undoped LSCO (x=0.00). Curves have same meaning as in Fig. 4.2. Vertical dashed line at 8990 eV marks the edge energy (i.e., Fermi level) as in Fig. 4.2.

4.4.2 Strong correlation effects and doping dependence

We emphasize that the conventional LDA-based formalism is fundamentally limited in its ability to describe the full doping dependence of the electronic structure of the cuprates, because the LDA yields a metallic instead of an insulating state in the undoped system. Therefore, strong correlation effects must be added to properly model the doping evolution of electronic states. Fig. **??** compares recent experimental results [88] with the theoretical O K-edge XANES spectra in overdoped LSCO, where the self-energy correction Σ along the lines of section IIB is included in the computations. Representative real and imaginary parts of Σ are shown in Das *et al.* [46] Focusing first on the overdoped regime for hole doping concentration between x = 0.20 to x = 0.30, both theory and experiment display a small, systematic shift of the edge to lower energies with increasing doping. The low energy peak at 528.5 eV in Fig. 4.4 shows the experimental and theoretical edge regimes, showing that both display a similar shift of the Fermi level with doping. Otherwise, the XANES

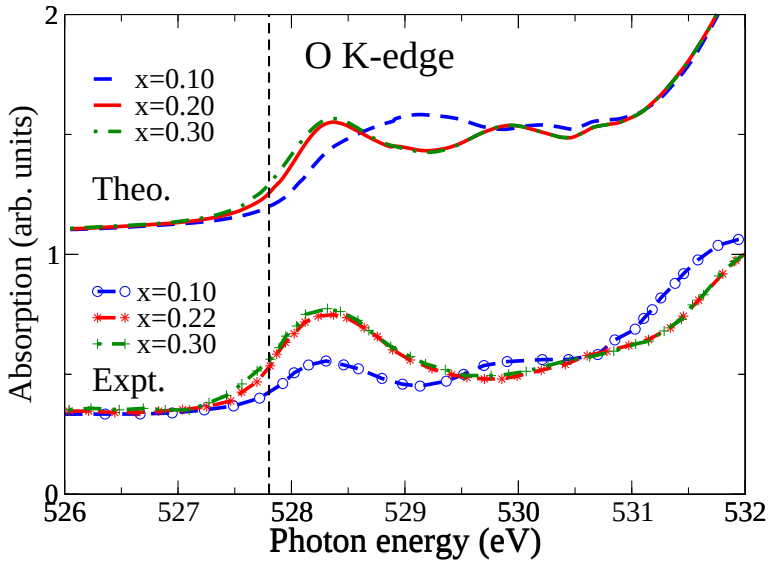

Figure 4.4: (color online) Doping-dependent theoretical (upper curves) and experimental [88] (lower curves) O K-edge XANES spectra in LSCO. Computations include the effect of self-energy corrections of Eq. (8) resulting from strong correlation effects. Different doping with different concentrations of x are shown by lines of various colors (see legend). Vertical line marks the edge energy (i.e., Fermi level) as in Fig. 4.2.

spectra undergo relatively little change in the overdoped system. As the doping is further reduced, the intensity of the 528.5 eV peak decreases while a new peak appears near 530 eV and rapidly grows with underdoping until at x = 0.00, the 528.5 eV peak is completely gone. The remaining 530 eV peak represents the upper Hubbard band, and its shift in energy from the Fermi level is consistent with optical measurements [46]. Turning to the x = 0.10 spectra in Fig. 4.4, we see that, as expected, now theory differs substantially from experimental results. Although theory correctly reproduces the reduced intensity of the 528.5 eV peak, it does not show the observed enhanced intensity of the upper peak at 530 eV. Instead, the spectral weight is shifted halfway between the lower and upper peaks. In Fig. 4.5, the experimental results indicate the opening of a gap in the spectrum which is not captured in our modeling. However, we were able to reproduce the experimental doping dependence [88] in a simpler calculation in which the XANES spectrum is modeled via the empty density-of-states, but in

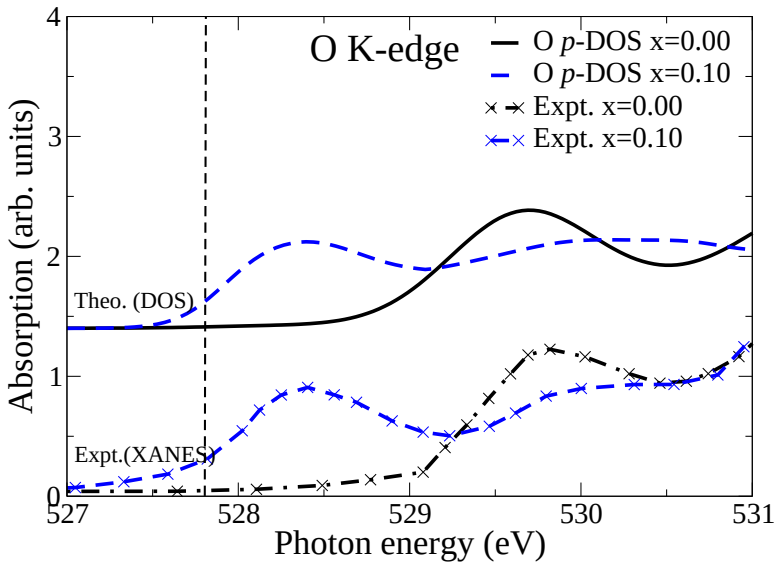

Figure 4.5: (color online) O K-edge XANES from experiment [101] (lower set of broken curves) for x = 0.00 and x = 0.10, compared with theoretical single-band *p*-DOS (upper curves) for O_{pl} for x = 0.00 and x = 0.10 [89]. The vertical line marks the edge energy (i.e., Fermi level) as in Fig. 4.4.

which self-energy corrections including the magnetic gap are incorporated [89]. Fig. 4.5 compares the experimental XANES spectrum with this DOS approximation at x = 0.10. The splitting of the spectrum into two peaks with the appropriate gap is well reproduced. It should be noted that this same self energy reproduced the optical and RIXS gaps as a function of doping [46, 90, 92]. Interestingly, the good agreement between theory and experiment in the overdoped case implies that the upper peak at 530 eV possesses little weight in the overdoped system. In particular, we find a saturation of the lower energy feature (528eV) in the O K-edge spectra [Fig. 4.4] as the doping value is increased beyond the optimal doping, except for the Fermi edge shift. This saturation is in good agreement with the experiment by Peets *et al.* [88], but is inconsistent with model calculations by Liebsch[102] and Wang *et al.* [103]. This effect requires a transfer of spectral weight from the upper to the lower peak, which is much larger than that predicted by *t-J* models of the cuprates [89]. A similar conclusion was arrived at by Peets *et al.* [88]. Such anomalous spectral weight transfer

has been discussed in several spectroscopies of cuprates [46, 104, 105]. The present intermediate coupling calculations can provide a satisfactory explanation of these results.

4.5 Conclusion

We have carried out a realistic calculation of the XANES of the cuprate superconductor LSCO. Our focus in this first such attempt is on the O K-edge XANES in overdoped LSCO over the hole doping range x = 0.20 to x = 0.30. For this purpose, we have incorporated doping dependent self-energy corrections due to strong electron correlations into a real space Green's function formalism, which is implemented in the FEFF9 code. Good agreement is found between theoretical and experimental doping evolution of the XANES in overdoped LSCO. Although LSCO has two chemically distinct O-atoms, the O K-edge XANES is dominated by the contribution of O-atoms in the cuprate planes. Apical O-atoms only begin to make a significant contribution to the spectrum at higher energies, $>$531 eV. In examining effects of the core-hole screening, we find that the spectra are insensitive to the core-hole screening model at least in the overdoped regime. In the underdoped case, as expected, our self-energy corrections, which are appropriate for the overdoped paramagnetic system, fail to correctly describe salient features of the spectra. A simple calculation suggests that correcting this will require a more comprehensive modeling of XANES including effects of pseudogap physics on the self-energies in the underdoped regime.

Chapter 5

CHARGE TRANSFER SATELLITES IN STRONGLY CORRELATED SYSTEMS

Many strongly correlated systems such as transition and rare-earth compounds, chemisorption systems, and high-T_c compounds have charge transfer or 'shake-down' between the more localized outer level (*d*) and less localized level (L). Following a three electron level model prescribed by Lee *et al.* [20] a perturbative construction of a spectral function is described in this chapter. Our real-space multiple scattering calculation for the Cu K-edge XANES of $La_{2-x}CuO_4$ and $Nd_{2-x}CuO_4$ was compared with the experimental result by Kosugi *et al.* [21]. A convolution of our calculated XANES with the Lee-Hedin spectral function took the missing many-body charge transfer effects into account, and was found to be in good accord with experiment.

5.0.1 Outline of this chapter

In this chapter we summarize the perturbative approach proposed by Lee *et al.* [20] to get the charge transfer satellites in Cu compounds. Section 5.2 discusses a short introduction of the nature of this problem, while section 5.3 is dedicated to our summary of the perturbative technique prescribed in the PRB paper by Lee and Hedin [20]. In section 5.4 we discuss our prescription of constructing a charge-transfer spectral function using the 'main peak to satellite' ratio from Lee *al.* We apply this spectral function in our RSGF calculation for Cu K-edge in LSCO and NCCO in section 5.5.

5.0.2 Key observation

Our RSGF calculated Cu K XANES convoluted with the charge-transfer spectral function gives good agreement with the experiment by reproducing the satellites in LSCO and NCCO.

5.1 Introduction

For many strongly correlated systems the core-level spectroscopy is effected by collective excitations and show satellite like features such as 'shake-down' or 'shake-up'. For example Cu com-

pounds often show such features. In one of the early experiments, Kosugi *et al.* [21] measured such satellites in the Cu K-edge XANES of NCCO and LSCO and identified them as the ligand-to-metal charge transfer satellites (LMCT). In the ground state, Cu has $3d^9$ configuration while all the ligand orbitals are filled. In the core-level x-ray experiment a core-hole in Cu can be created and it becomes energetically favorable for an electron to transfer from the ligand ($4s$) to the Cu site ending with $3d^{10}$ configuration. In the latter case the core-hole will be strongly screened. Due to hybridization between the d^9 and d^{10} configurations, the final states will be a mixture of the two configurations as indicated in Fig. 5.1. In the sudden approximation limit, when the photo-electron kinetic energy is high and extrinsic and intrinsic losses decouple, this satellite feature caused by the screening strength of the two configurations is usually observed in the photo-emission experiments. Within the sudden approximation one can then construct a spectral function by extracting two parameters from the photo-emission spectrum which are the the ratio of the peak intensity $r_0(\omega)$ and energy split δE between the main and the satellite peak. About 10 eV above the edge energy, such satellites were also observed in some of the Cu K-edge XANES of the high-T_c cuprates. But obtaining a spectral function for such spectrum is not straightforward since this energy range falls within the adiabatic limit where the extrinsic and intrinsic losses don't decouple. In this chapter we closely follow the three electron model prescribed by Lee and Hedin [11] where we considered r_{00} ($= r_0(\omega)|_{\omega\to\infty}$), and δE as parameters.

5.2 Lee-Hedin charge transfer satellite model

The Lee-Hedin model as proposed by Lee *et al.* [20] is a three electronic level model that starts with a Hamiltonian,

$$H_0 = \varepsilon_a n_a + \varepsilon_L n_L + \varepsilon_c n_c + U_a n_c n_a + U_b n_c n_b + t(c_a^\dagger c_L + c_L^\dagger c_a). \tag{5.1}$$

The first two terms give the eigenvalues of the localized state (e.g. $3d$) and delocalized ligand state L. The last term is the hybridization between them. The remaining terms give the energy(ε_c) and occupation(n_c) of the core state. In x-ray absorption or photoemission spectroscopy, a core electron is excited leaving behind an empty core state c. So $n_c = 1 \to 0$. In Cu compounds, for example, c may represent the Cu $1s$ core level, a the localized Cu $3d$ valence level and L a ligand state (e.g., hybridized state between Cu $4s$ and O $2p$). With x-ray excitation the total Hamiltonian can be

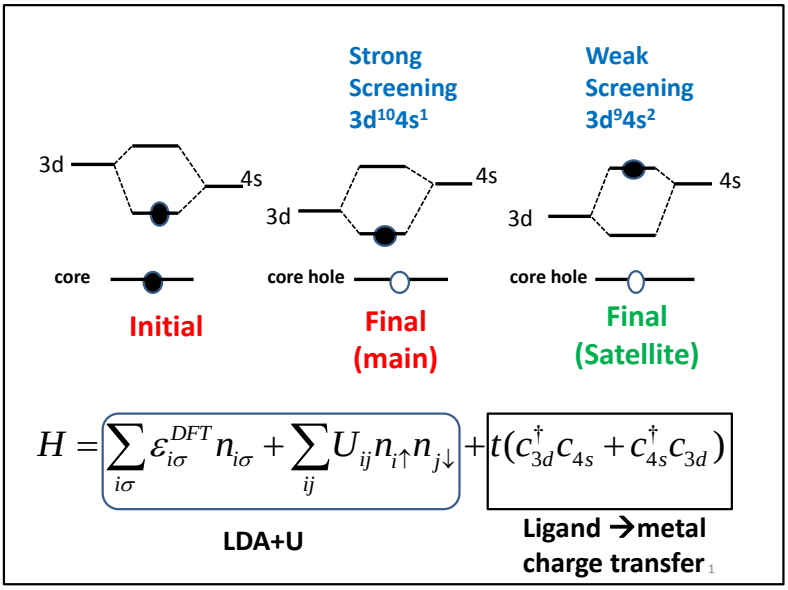

Figure 5.1: Spectral function of the electron-doped high T_c cuprate $Nd_{2-x}Ce_xCuO_4$ using the separable potential approach of Lee-Hedin model

written as,

$$H = H_0 + T + V + \Delta. \tag{5.2}$$

Here T is the sum of one-electron kinetic energies of continuum state,

$$T = \sum_k \varepsilon_k n_k \tag{5.3}$$

with energies $\varepsilon_{\mathbf{k}} = k^2/2$, and wave functions $\psi_{\mathbf{k}}$ obtained from a one-electron potential in the presence of core-hole ($n_c = 0$). The perturbation causing photoemission is

$$\Delta = \sum_{\mathbf{k}c} (M_{\mathbf{k}} c_{\mathbf{k}}^{\dagger} c_c + h.c.), \tag{5.4}$$

where $M_{\mathbf{k}}$ is the transition matrix element. Now the interaction between the photo-electrons are taken as,

$$V = \sum_{\mathbf{k}\mathbf{k}'} [n_a V_{\mathbf{k}\mathbf{k}'}^{(a)} + n_b V_{\mathbf{k}\mathbf{k}'}^{(b)} - V_{\mathbf{k}\mathbf{k}'}^{(c)}] c_{\mathbf{k}}^{\dagger} c_{\mathbf{k}'}. \tag{5.5}$$

Here $V_{\mathbf{kk'}}$ is a matrix element of the Coulomb potential $V^{(\nu)}(\mathbf{r})$ from the charge density of the orbital ν

$$V^{\nu}_{\mathbf{kk'}} = \int \psi^{*}_{\mathbf{k}}(\mathbf{r}) \frac{\rho_{\nu}(\mathbf{r'})}{|\mathbf{r}-\mathbf{r'}|} \psi_{\mathbf{k'}}(\mathbf{r}) d\mathbf{r} d\mathbf{r'} \tag{5.6}$$

To obtain charge transfer satellites these matrix elements $M_{\mathbf{k}}$ and $V_{\mathbf{kk'}}$ can in principle be calculated using the real-space multiple scattering code FEFF. But in this chapter we take a simplistic approach to calculate the spectral function and closely follow the prescription by Lee *et al.* [20]. In their model with three electron levels the valence wave functions were calculated using muffin tin potentials with radius R, and then the calculated matrix elements were fitted to get an analytical expression for $M_{\mathbf{k}}$ and $V_{\mathbf{kk'}}$.

$$M_k = \frac{\varepsilon_k / E_d}{1 + \varepsilon_k / E_d}, \tag{5.7}$$

where $\varepsilon_k = k^2/2$, $E_d = 1/2R_d^2$, and for 1s core state R_d is a length scale taken as $R_d x \approx 0.5$ a.u. And,

$$V_{kk'} = \frac{VR_s}{R} \frac{1}{1 + R_{sd}^2 (k-k')^2}. \tag{5.8}$$

Here R_s is the length scale of the interaction $V_{\mathbf{kk'}}$ and $R_s = 1.77$ a.u., and R is the muffin tin radius. More detail of these derivations can be found in [20].

5.2.1 Three Level System without interaction, $V = 0$:

Initially when $n_c = 1$, the ground state of H_0 is given by

$$|\Psi_0\rangle = -\sin\theta\,|\psi_c\rangle\,|\psi_a\rangle + \cos\theta\,|\psi_c\rangle\,|\psi_L\rangle\,, \tag{5.9}$$

with eigen energy,

$$E_0 = \varepsilon_c + \frac{1}{2}(\varepsilon_a + U + \varepsilon_L) - \frac{1}{2}\sqrt{(\varepsilon_a + U - \varepsilon_L) + 4t^2}, \tag{5.10}$$

where

$$\tan 2\theta = \frac{2t}{(\varepsilon_a + U - \varepsilon_L)}. \tag{5.11}$$

In the final state when $n_c = 0$, the two possible states (due to charge transfer between ligand and 3d states) are

$$\begin{aligned} |\psi_1\rangle &= \cos\phi\,|\psi_a\rangle - \sin\phi\,|\psi_L\rangle \\ |\psi_2\rangle &= \sin\phi\,|\psi_a\rangle + \cos\phi\,|\psi_L\rangle\,, \end{aligned} \tag{5.12}$$

with eigenenergies

$$E_2^1 = \frac{1}{2}(\varepsilon_a + \varepsilon_L) \mp \frac{1}{2}\sqrt{(\varepsilon_a - \varepsilon_L)^2 + 4t^2}, \tag{5.13}$$

and

$$\tan 2\phi = \frac{2t}{(\varepsilon_L - \varepsilon_a)}. \tag{5.14}$$

Here δE can be defined as the energy separation between the main and satellite peaks,

$$\delta E = \sqrt{(\varepsilon_a - \varepsilon_L) + 4t^2}. \tag{5.15}$$

The photocurrents for main(s=1) and satellite(s=2) are given [20] by

$$J_k^s(\omega) = \left| \left\langle \Psi_f^{sk} \right| \Delta \left| \Psi_0 \right\rangle \right|^2 \delta(\omega - \varepsilon_k + E_0 - E_s), \tag{5.16}$$

where $\left|\Psi_f^{sk}\right\rangle$ is a final state. In the sudden approximation the final state can be written as $\left|\Psi_f^{sk}\right\rangle = |\psi_s\rangle\,|\psi_k\rangle$. Now, summing over $\mathbf{k}$ one obtains absorption spectra $J_s(\omega)$,

$$J_s(\omega) = \sum_k J_k^s(\omega). \tag{5.17}$$

In the sudden approximation, the kinetic energy of photoelectrons is large, and we can take $k_1 = k_2$. The ratio r_{00} of the satellite to the main peak intensity then is,

$$r_{00} = lim_{\omega\to\infty} \frac{J_2(\omega)}{J_1(\omega)} = \cot^2(\phi + \theta). \tag{5.18}$$

Taking the k dependence of M_k we obtain,

$$r_0(\omega) = r_{00}\left[\frac{\Delta\omega}{\Delta\omega + \delta E}\right] \times \left[\frac{1 + (\Delta\omega + \delta E)/E_d}{1 + \Delta\omega/E_d}\right] \Theta(\Delta\omega). \tag{5.19}$$

Here $\Delta\omega = \omega = \omega_{th}$ and $\omega_{th} = E_2 - E_0$. From Eqs.5.13 to 5.19 we see that r_{00} and δE equivalently describes the two parameters U and t used by Lee-Hedin model. In this chapter, these are the two parameters we used to construct the spectral function in order to convolute the absorption spectra obtained from FEFF code for the case of Cu K-edge in LSCO and NCCO.

5.2.2 Three Level System with interaction, $V \neq 0$

Now turning on the interaction between the photoelectrons in the continuum state the Hamiltonian is,

$$H = H_0 + T + V. \tag{5.20}$$

The exact, final photoelectron state is

$$\left|\Psi_f^{sk}\right\rangle = \left[1+\frac{1}{E-H_0-T-V-i\eta}V\right]|\psi_s\rangle\,|\psi_k\rangle\,, \tag{5.21}$$

where $|\psi_s\rangle$ (s=1,2) are the eigenstates of H_0 with the core-hole, and $E=\varepsilon_k+E_s$ is the energy of the final state. Now, the dipole transition matrix element $M(s,k)=\left\langle\Psi_f^{sk}\right|\Delta|\Psi_0\rangle$ can be written as

$$M(s,k)=\langle\psi_k|\,\langle\psi_s|\left[1+V\frac{1}{\varepsilon_k+E_s-H_0-T-V+i\eta}\right]\Delta|\Psi_O\rangle\,. \tag{5.22}$$

At this point instead of exact treatments we will use the first order perturbation in $V_{kk'}$ to obtain the transition matrix elements as prescribed by Lee *et al*. To the lowest order in V one ignores the V term in the denominator of Eq .5.22. Inserting the completeness relation $\sum_i|i\rangle\langle i|$ in terms of the eigenstate $|i\rangle=|k\rangle\,|s\rangle$ we obtain

$$M(s,k)=\langle s|\,\langle k|\,\Delta\,|\Psi_0\rangle+\sum_{k's'}V_{ks,k's'}[(E-H_0-T+i\eta)^{-1}]_{k's',k's'}\left\langle s'\right|\left\langle k'\right|\Delta\,\langle\Psi_0\rangle\,. \tag{5.23}$$

For $s=1,2$ one obtains

$$\begin{aligned}M(1,k)=&-\sin(\phi+\theta)M_k-\sin^2\phi\,\sin(\phi+\theta)\sum_{k'}\left[\frac{V_{kk'}M_{k'}}{E-E_1-\varepsilon_{k'}+i\eta}\right]\\&-\frac{\sin 2\phi\,\cos(\phi+\theta)}{2}\sum_{k'}\left[\frac{V_{kk'}M_{k'}}{E-E_2-\varepsilon_{k'}+i\eta}\right],\end{aligned} \tag{5.24}$$

and

$$\begin{aligned}M(2,k)=&\cos(\phi+\theta)\,M_k+\cos^2\phi\,\cos(\phi+\theta)\sum_{k'}\left[\frac{V_{kk'}M_{k'}}{E-E_2-\varepsilon_{k'}+i\eta}\right]\\&+\frac{\sin 2\phi\,\sin(\phi+\theta)}{2}\sum_{k'}\left[\frac{V_{kk'}M_{k'}}{E-E_1-\varepsilon_{k'}+i\eta}\right].\end{aligned} \tag{5.25}$$

In the above two equations we used

$$V_{ij}=V_{ks,k's'}=V_{kk'}v_sv_{s'} \tag{5.26}$$

where $v_s=-\sin\phi$ if $s=1$, and $v_s=\cos\phi$ if $s=2$.

Now considering $R_k=R_s=R$, Lee *et al.* [20] defined a function F_k by

$$\sum_{k'}\frac{V_{kk'}m_{k'}}{\varepsilon-\varepsilon_{k'}+i\eta}=-\frac{V}{E}M_kF_k(\varepsilon/E), \tag{5.27}$$

using the simple analytical form of $V_{kk'}$ and M_k from Eq .5.7 and Eq .5.8. Thus,

$$F_k(\varepsilon) = \frac{1}{\pi}\int_0^\infty \frac{x^4 dx}{[1+x^2]^2\,[1+(Rk-x)]^2\,[x^2-\varepsilon-i\eta]}. \tag{5.28}$$

From Eq.5.24 and Eq.5.25 one obtains

$$\frac{r(\omega)}{r_0(\omega)} = \left| \frac{1-\cos^2\phi\,\frac{V}{E}F_{k_2}(\frac{\omega}{E}) - \frac{\sin 2\phi\,\sin(\phi+\theta)}{2\cos(\phi+\theta)}\,\frac{V}{E}F_{k_2}(\frac{\omega+\delta E}{E})}{1-\sin^2\phi\,\frac{V}{E}F_{k_1}(\frac{\omega+\delta E}{E}) - \frac{\sin 2\phi\,\cos(\phi+\theta)}{2sin(\phi+\theta)}\,\frac{V}{E}F_{k_1}(\frac{\omega}{E})} \right|^2, \tag{5.29}$$

where r/r_0 depends only on V/E, $\delta E/E$, and $\Delta\omega/E$. Using the above equation along with Eqs.5.18 and 5.19 we get $r(\omega)$ and finally construct the charge transfer spectral function.

5.3 Spectral function

In order to construct the spectral function to account for charge transfer effects we start with a spectral function of the following form,

$$A(\Delta\omega) = C_1(\Delta\omega)\delta(\Delta\omega) + C_2(\Delta\omega - \delta E). \tag{5.30}$$

For notational simplicity and to avoid confusion, from here on we will denote $\Delta\omega = \omega$. Now the coefficients of the normalized spectral function

$$A(\omega) = C_1(\omega)\delta(\omega) + C_2(\omega - \delta E) \tag{5.31}$$

has the following two conditions;

$$\begin{aligned} C_1(\omega) + C_2(\omega) &= 1 \\ \frac{C_1(\omega)}{C_2(\omega)} &= r(\omega). \end{aligned} \tag{5.32}$$

Here we used δE and r_{00} as parameters which are equivalent and obtainable from t and U used in the Lee-Hedin model. Such spectral functions can be used to convolute the calculated spectra to account for the charge transfer effects.

$$\mu(\omega) = \mu^{FEFF}(\omega,\omega') * A(\omega') \tag{5.33}$$

For high-T_c $Nd_{2-x}CuO_4$ we used $\delta E \sim 8$ eV from the satellite peak position in Cu K-edge XANES experiments and $r_{00} = 2.3$ is taken as the best fitted value.

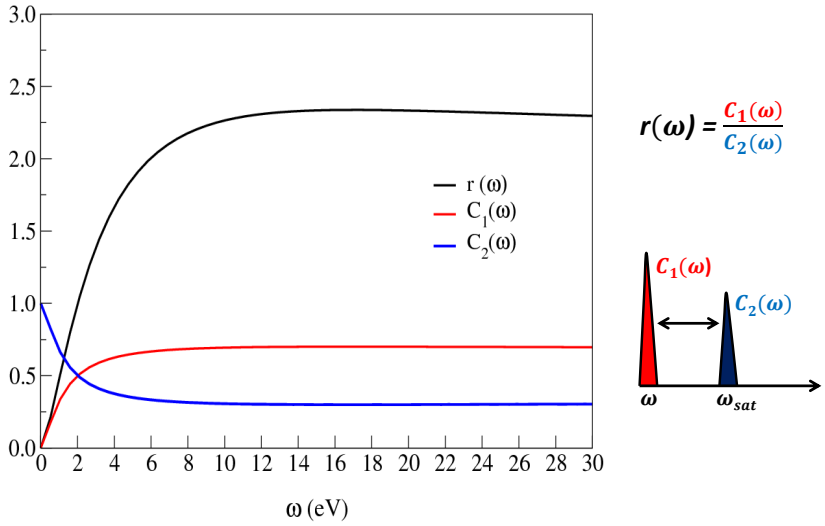

Figure 5.2: Spectral function of the electron doped high T_c cuprate $Nd_{2-x}Ce_xCuO_4$ using the separable potential approach of Lee and Hedin model

5.4 X-ray spectroscopy of High T_c materials

Both in NCCO and LSCO, Cu K-edge XANES show the remarkable satellite feature 7 or 8 eV apart from the main peak. We see the presence of such peaks in the experiment (dashed green) curve of Figs. 5.4 and Fig. **??** at 22 eV, and again at around 38 eV.

We calculated the Cu K-edge XANES using the real-space multiple scattering code FEFF (solid red curve) and (see in Fig. 5.4 and Fig. **??**). Being a single configuration code, FEFF fails to account for any charge transfer effects and misses the satellite structure. Significant improvement was achieved by convoluting the FEFF calculated spectra with the spectral function obtained from the Lee and Hedin model. The post-convoluted XANES is plotted in the solid blue curve in Fig. 5.4 and Fig. **??**. For LSCO in Fig. 5.4 we see a shoulder like feature at 22 eV before the convolution which is caused by the structure of the system mainly due the presence of the apical oxygen atoms. This feature is completely absent in the spectrum of NCCO in Fig. **??** (solid red line) which does

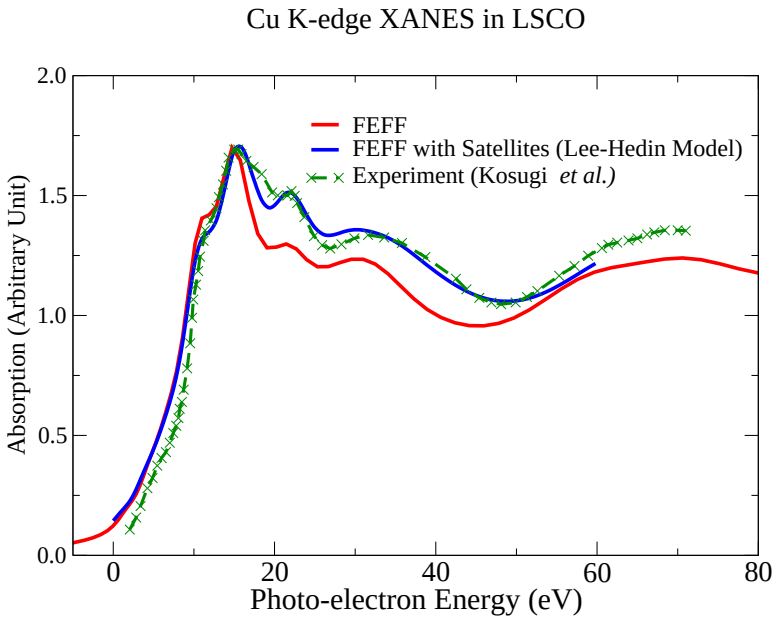

Figure 5.3: Cu K-Edge XANES of $La_{2-x}Sr_xCuO_4$ with and without charge transfer satellite correction

not have any apical oxygen. We have confirmed this by calculating the spectrum of structures with longer distance between the apical oxygen atoms and Cu in LSCO which tends to wash this peak out at 22eV. Spectral convolution enhances the satellite peaks for both these materials.

5.5 Conclusion

Following Lee and Hedin's three level model and using two parameters extracted from experiment we have constructed a spectral function which in principle can account for the charge transfer from delocalized to localized orbitals in correlated systems. FEFF calculated XANES convoluted with this spectral function correctly reproduce the charge transfer satellites observed in the Cu K-edge XANES of high-T_c cuprates Nd_2CuO_4 and La_2CuO_4 [21]. The construction of the spectral function employed the analytical formulation of potential and dipole transition matrix elements as prescribed by Lee *et al.* [20]. Although this simple formalism improves the spectral features significantly, a

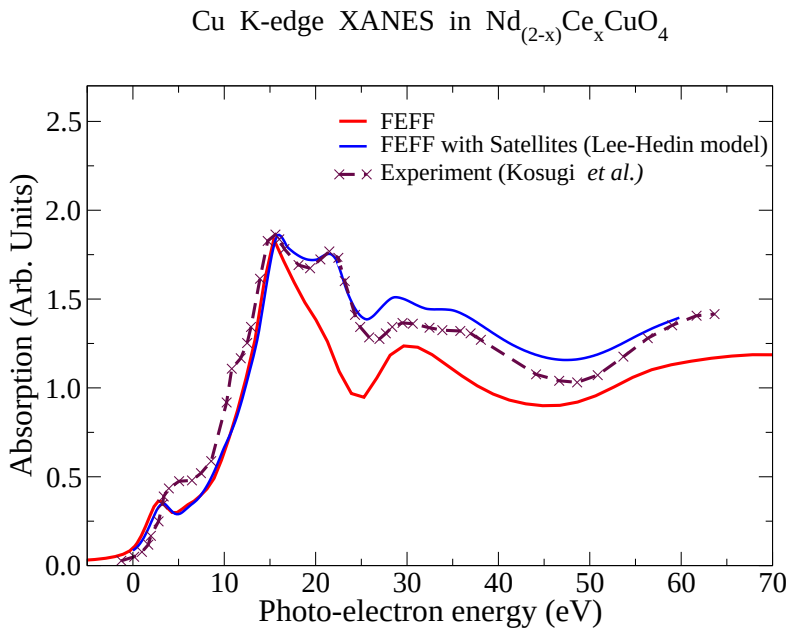

Figure 5.4: Cu K-Edge XANES of $Nd_{2-x}Ce_xCuO_4$ with and without our charge transfer satellite correction

more robust calculation of $V_{kk'}$ and M_k can be done within the real-space multiple-scattering framework is in progress.

Chapter 6

OTHER ELECTRONIC STRUCTURES: DNA-GRAPHENE HYBRIDS

We calculate the electronic local density of states (LDOS) of DNA nucleotide bases (A,C,G,T) deposited on graphene. We observe significant base-dependent features in the LDOS in an energy range within a few eV of the Fermi level. These features can serve as electronic fingerprints for the identification of individual bases in scanning tunneling spectroscopy (STS) experiments that perform image and site dependent spectroscopy on biomolecules. Thus fingerprinting of DNA-graphene hybrid structures using STS may provide an alternative route to DNA sequencing.

Additionally we calculate the conductance current through Graphene nano ribbon with DNA nucleotide bases (A,C,G,T) inside a pore. We observe significant base-dependent features in the transmission and its first derivative in an energy range within a few eV of the Fermi level. These features can serve as electronic fingerprints for the identification of individual bases in nano-pore experiments in vacuum. Thus the fingerprints of DNA in graphene nano-pore may provide a guideline and alternative route to DNA sequencing.

6.1 Electronic Fingerprints of DNA bases on Graphene

The determination of the precise sequences of the four nucleotides [adenine (A), cytosine (C), guanine (G) and thymine(T)] in DNA molecules is an important goal for both fundamental research interests as well as a large number of applications in biomedical research [106], bio-technology [107, 108], drug delivery [109], and biomaterial growth [110]. However, conventional approaches are generally complex and expensive [111]. Numerous experimental and theoretical [112–114] attempts have been made to improve such determinations. For example, efforts have been made to develop efficient techniques based on high-resolution microscopic [115, 116] and spectroscopic [117] probes that can yield direct fingerprints of these biomolecules. However, these techniques require the biomolecules to be deposited on a host substrate in an ultra-high vacuum environment. Difficulties in preparing high-quality samples and in obtaining reproducible measurements have lim-

ited the utility of these approaches [118]. For example, the electronic fingerprints of a given DNA base can vary dramatically even for subtle changes in the relative angle of a base with respect the substrate [119]. On the other hand, a recent scanning tunneling microscopy/spectroscopy (STM/S) study [117] by Tanaka *et al*. has shown that the guanine base of DNA on a Cu(111) surface always exhibits a strong tunneling peak around a fixed bias voltage of -1.6 eV, thus providing a reliable marker in tunneling measurements. This observation has led to a significant advance in the field, since it opens an opportunity for electronic identifications of all bases via tunneling conductance from a local probe. However, the localized *d* states and the dangling bonds near the surface of the bulk Cu are among the many effects that can complicate the implementation of this approach, thus suggesting the importance of finding a more suitable substrate.

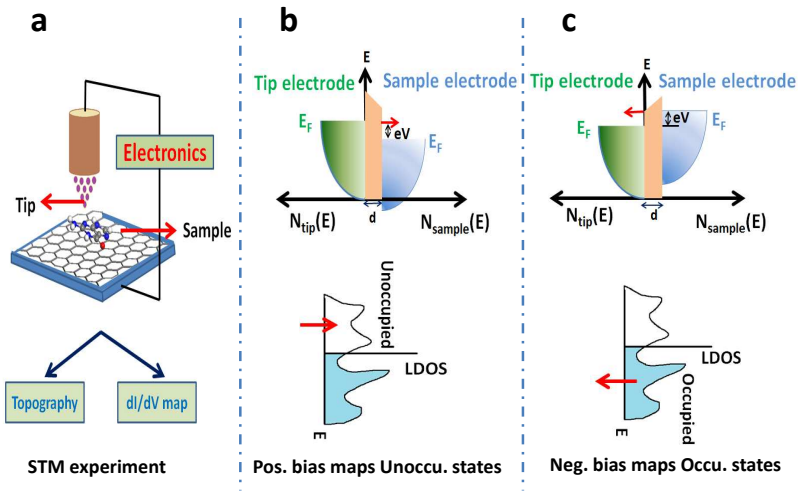

Figure 6.1: **a** Schematic illustration of STM experiment which can extract topographical image and dI/dV information of a sample lying on graphene plane; **b** and **c** schematically demonstrate tunneling between the tip and sample. Based on positive (**b**) or negative (**c**) bias voltage, electrons can transmit to or from the graphene and map the unoccupied or occupied local density of states (LDOS) correspondingly of the sample lying on the plane.

We show that an attractive substrate to consider is graphene, a purely two-dimensional sheet of carbon atoms arranged in a honeycomb lattice [120]. Among its unique properties, graphene possesses linearly dispersed Dirac quasiparticles with a semimetal density of states near the Fermi level [120, 121]. Additionally, graphene combines a conducting surface with remarkable mechanical strength. Also strong $\pi - \pi$ interactions between DNA bases and conjugated carbons in graphene should favor mostly plane orientations of DNA bases with respect to the surface [122] and, thus, results in relatively homogenous orientations of bases in the DNA strands when it adsorbs on graphene

and offers optimal conditions for STM measurements. These characteristics make this novel material an excellent surface for studying adsorbates of various organic macro-molecules. Several successful implementations of graphene have already been reported recently in electronic devices and biomedical and bioassay applications [123–125]. We aim to develop a detailed understanding of the interaction and adsorption between graphene and biomolecules such as the DNA bases including local electronic structure, using an approach that goes beyond the structural analysis of such hybrid systems.

To achieve this goal, we have carried out extensive DFT-based, first-principles, numerical simulations of the electronic local densities of states (LDOS) of all four DNA bases on graphene. Considering only the short range interaction between the DNA bases and graphene, the van der Waals interaction was not included in our calculation. It was previously demonstrated that on distances of 2 to 3 Å, the long range dispersion interaction correction becomes negligible [119, 126, 127]. We find that the electronic LDOS of the nitrogen atom can serve as an electronic fingerprint of a particular DNA base. That is, we find several distinguishing and dominant features in the LDOS that can identify each base. This finding can be used in conjunction with STM/S measurements of atomic resolution that image and probe the local density of states(LDOS) of surfaces, as illustrated in Fig. 6.1. In particular, i) we deduce that the local chemical environment and the graphene base leads to new electronic states and additional features in the local density of state (LDOS) inside the parent highest occupied molecular orbital (HOMO) and lowest unoccupied molecular orbital (LUMO) insulating gap. ii) For each base the peak positions and peak heights exhibit a characteristic evolution as a function of their orientation with respect to the graphene sheet; iii) We also investigate the similarities and differences of the LDOS of DNA bases by placing the graphene on the commonly used SiC substrate. The STM topography simulations also add important insights into the characterization of charge distributions and hybridization of states between bases as well between base and graphene. Taken together, we demonstrate that all four bases of DNA adsorbed on a graphene substrate can be differentiated quantitatively. This suggests the possibility of an efficient and cost-effective sequencing approach.

In an STS experiment, measurements are done in two steps. First, the tip scans over the surface to search for the locations of the maximum transmission currents at a fixed voltage (6.1(a)) and constructs the topographic image. In the next step, the voltage is varied over an energy range

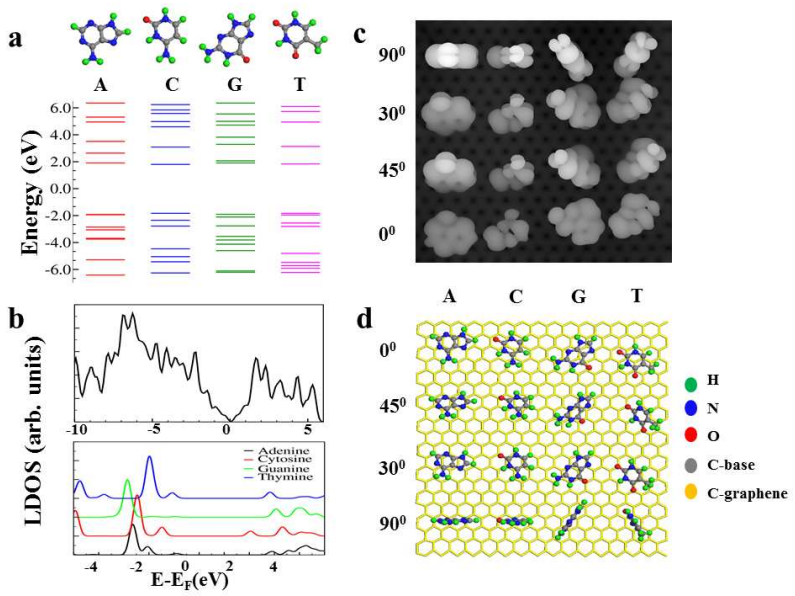

Figure 6.2: **(a)** Molecular energy levels of each isolated DNA base molecule; **(b)** Upper panel shows LDOS of carbon atom in pure graphene and lower panel shows nitrogen peak LDOS in isolated DNA bases. **(c)** Integrated (-3.0 eV to E_F = 0) partial charge density of DNA bases on graphene plane. Base types are organized in columns and angles between base-ring and graphene plane are varied along rows as indicated. This simulation of STM topography is done using HIVE-STM [128] code. **(d)** Molecular orientations of DNA bases corresponding to the images in **c** are displayed.

by keeping the tip position fixed, and the differential current dI/dV which determines the local electronic structure (LDOS) of the sample is then measured. A schematic illustration is presented in 6.1(b) and (c).

We first considered the behavior of isolated DNA base molecules using DFT calculations. In 6.2(a), the molecular energy levels of each base are reproduced, in agreement with previous calculations [119]. These results confirm that all nucleo-bases have a large HOMO-LUMO gap ($E_g \approx$ 5 eV). Near the energy gap, all electronic features are qualitatively similar for all four bases. Such small variations in the electronic structure of DNA bases might bring in to question whether STM is able to resolve fingerprints features of DNA bases. On the other hand, the presence of a substrate and subsequent interactions significantly affect the alignment of electronic levels of bases compared to the isolated molecules as was theoretically predicted for adsorbed DNA bases on the Cu surface [119]. We have considered an experimental setup with freeze-dried conditions, that will result in significantly diminished noise due to the changes of molecular configuration and due to low temperature.

To investigate the effect of graphene on the DNA bases, we first calculate the LDOS of nitrogen

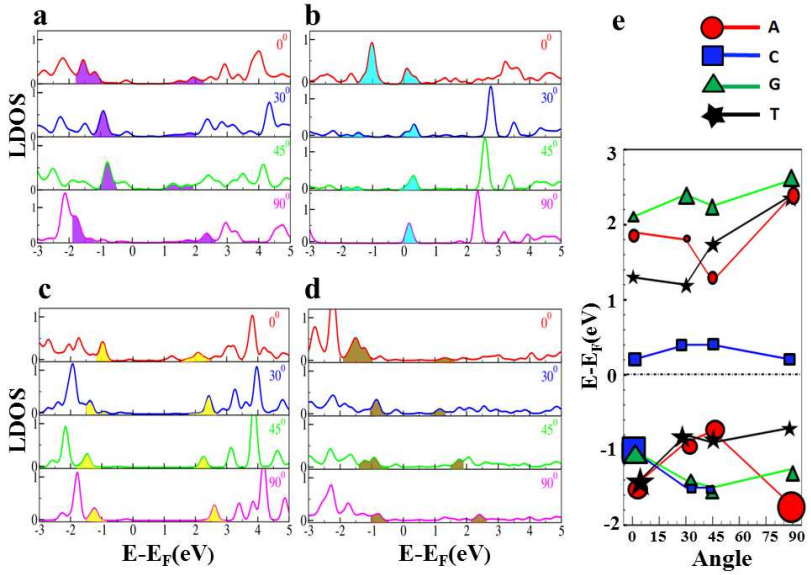

Figure 6.3: **a** Solid lines are nitrogen LDOS in adenine adsorbed on graphene with different angles, and the shaded regions show the dominant peak features near E_F on both positive and negative energy side, 0 eV corresponds to Fermi energy; **b**, **c**, and **d** shows similar LDOS curves for cytosine, guanine and thymine correspondingly; **e** Dominant peak positions near E_F for different angles and bases. Positions of the peaks are plotted along y-axis and angles along x-axis. The relative size of the symbols reflects the relative peak intensity for each case.

atoms in the isolated DNA bases and the LDOS of carbon atoms in the bare graphene as shown in 6.2(b). For the bare graphene, our calculation reproduces the well-known and distinct electronic feature of graphene at E_F – the presence of a Dirac cone [129] – as can be seen in 6.2(b).

STM topographical images also provide important geometric information. This is particularly important in systems where molecules of interest can interact with the surface at many different orientations. Depending on the backbone configuration, DNA bases in a single stranded (ssDNA) can be adsorbed onto the graphene surface at different angular orientations and further complicate the electronic identification. Thus, we constructed supercells where each DNA base lies on the graphene surface with four possible angles (6.2(d)). In order to simulate a STM topographic image theoretically, we integrated our DFT based partial charge density from -3.0 eV to E_F using HIVE-STM [128] (6.2(c)). The average distance between the DNA bases and graphene plane was fixed at 3.0 Å.

In the remainder of this study, we primarily focus on the dI/dV (or LDOS) of DNA bases on graphene. Since nitrogen is a common constituent of all four bases with the most diffuse orbitals, we analyze the dependence of the LDOS on both the DNA base and its spacial orientation when a

featureless tip is placed directly above a nitrogen atom. The calculated LDOS is shown for isolated DNA bases (6.2(b)) and adsorbed bases (6.3). For the adsorbed bases, we identify the behavior of the dominant peak features within the range of -3.0 to 3.0 eV, and their dependence on the angle between the base-ring plane and graphene plane. These peaks are marked by the colored shaded regions in the curves of 6.3(a)-(d). In 6.3(e), we summarize these angle dependent results for the positive and negative bias energies for all four bases.

By examining 6.3, one can recognize the dominant STS peak features, except for a few cases where the experimental resolution can play a critical role. For example, simulated LDOS (6.3(e)) shows distinctive features in the positive low energy region (unoccupied states) for cytosine (the lowest among all) and guanine (the highest among all), independent of the base orientation.

Consequently, if several LDOS peaks are compared (for example, both occupied and unoccupied states close to the Fermi energy), the identification of the bases can be achieved. For the above example the supercell consisted of a set of ~ 130 atoms, and a full geometry optimization on such systems is computationally expensive. To asses the interaction between the graphene and the bases, we reduced the supercell and performed a full geometry optimization using VASP [14, 130, 131] software package.

Our calculations reveal the dependence of the binding energies on the angular orientation for a given base. For example, the 0° configuration of adenine is more bound than the 45° one. The preference in plane alignments of bases with respect to the graphene is expected, since parallel orientation of bases along the graphene surface allows better overlap in π orbitals between the aromatic rings of DNA bases and aromatic carbons in graphene increasing the $\pi - \pi$ stacking. This interaction results in relatively homogeneous and planar orientations of bases in the DNA strand adsorbed on the graphene, which offers favorable conditions for STM experiment and better resolution of dI/dV features. At small angles ($<$15 degrees), the highest occupied states of cytosine and guanine (below Fermi energy) are well distinct from adenine and thymine, as can be seen in 6.3(e). In addition, at plane configurations, the peaks corresponding to the highest occupied states of adenine and thymine have closely lying satellite peaks, while guanine and cytosine have well-separated sharp peaks. Thus, comparing several peaks (occupied and unoccupied) and their shapes will provide necessary fingerprints to differentiate DNA bases.

In STM experiments, graphene is often supported by another substrate, such as silicon carbide.

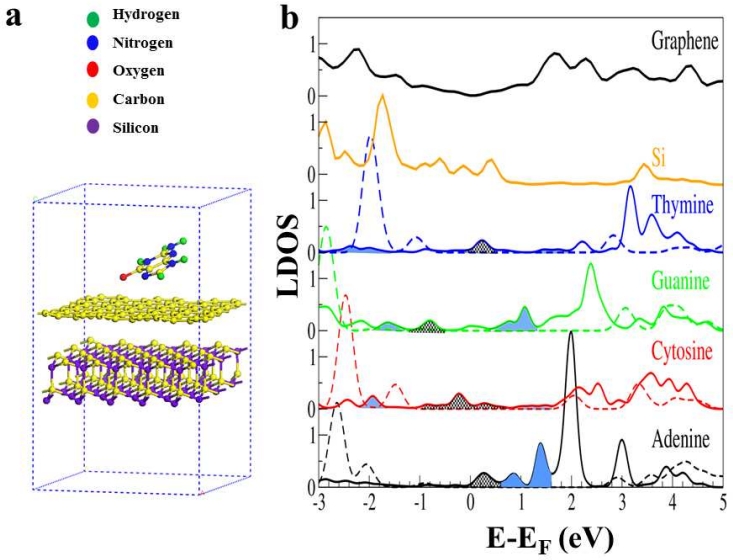

Figure 6.4: **a** Supercell that includes single layered SiC crystal under the 2D graphene plane. **b** nitrogen LDOS of four DNA bases (adenine (black), cytosine (red), guanine (green), and thymine (blue). Solid lines are for the bases adsorbed on graphene+SiC substrate; the dashed lines are the nitrogen LDOS for isolated bases. The LDOS curve for the nearest neighbor Si atom is displayed in orange solid curve, and the topmost curve is for carbon LDOS in pure graphene. The shaded colored (blue) regions are the dominant peak positions due to hybridization between N and C (graphene) atoms, and shaded dark regions are due to hybridization between N and underlying nearest Si atom.

To better simulate real systems we added a single layered silicon carbide (SiC) crystal under the graphene sheet. Fig. 6.4 presents our calculated nitrogen LDOS for each base, where the base-ring plane and graphene plane are parallel to each other. The LDOS of the Si atom nearest to the base molecules is shown by the orange solid line in 6.4. Surprisingly, the orbitals of the DNA bases are spread over the SiC despite the separating layer of graphene. Such a "see through effect" is pronounced for Si states close to E_F resulting in the hybridized peaks of nitrogen LDOS indicated by the black shaded regions.

We see this effect only in close proximity to E_F, and the STS resolvable dominant features around $\pm$ 2.0 eV remain identifiable. These latter peaks originate from the hybridized states between the DNA bases and graphene and are shown by the blue shaded regions in 6.4. The dominate peak features near 1.0-2.0 eV are well-pronounced for guanine and adenine. The largest peak features of adenine and guanine at 2.0-2.5 eV also have potential as electronic fingerprints for STS

experiment.

6.2 Identifying DNA bases with Transport Current

A major goal in medical research is to develop a fast, accurate and low cost DNA sequencing technique that can sequence a diploid mammalian genome for $1000 within 24 hours. The nanopore-based devices provide a highly confined space that can identify the presence of a single DNA nucleotide passing through the pore using a variety of ways of creating identifiable signals [132]. Some of the recent table top experiments [133] show promising and potentially useful results using protein nanopores. But none of these methods are error free due to high noise to signal ratio in the ion channeling method through complex pores.

In this section we propose a simple nanopore device constructed with a punctured graphene mono-layer ribbon which is suspended between two gold electrodes. We use 2 eV bias voltage between the electrodes. Using DFT and NEGF techniques implemented in 'TranSiesta' version of the code 'SIESTA' [134, 135], we calculate the transmission current between the electrodes, while placing Adenine (A), Guanine (G), Cytosine (C), and Thymine (T) inside the pore. This simple device geometry is schematically shown in Fig. 6.5

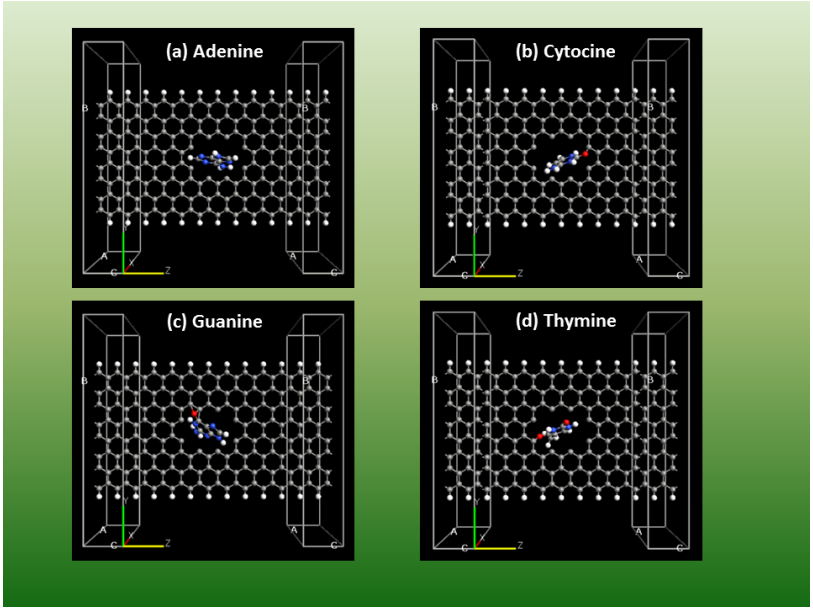

Figure 6.5: Schematic illustration of nano-pore experiment which can extract dI/dV information of a sample passing through the graphene nano-pore; **a** Adenine, **b** Cytosine **c** Guanine, and **d** Thymine; Based on the positive (**b**) or negative (**c**) bias voltage between the electrodes, electrons can transport through the graphene nano-ribbon , and map the conductance of the sample lying inside the pore.

Our calculations are limited to identifying only the single nucleotides one at a time, and ignoring

the phosphate back-bone structure of sDNA. Assuming the back bone will only contribute to a consistent shift in the transmission signal, we here focus on the detection of distinct features in the transmission current due to different isolated DNA bases inside the pore.

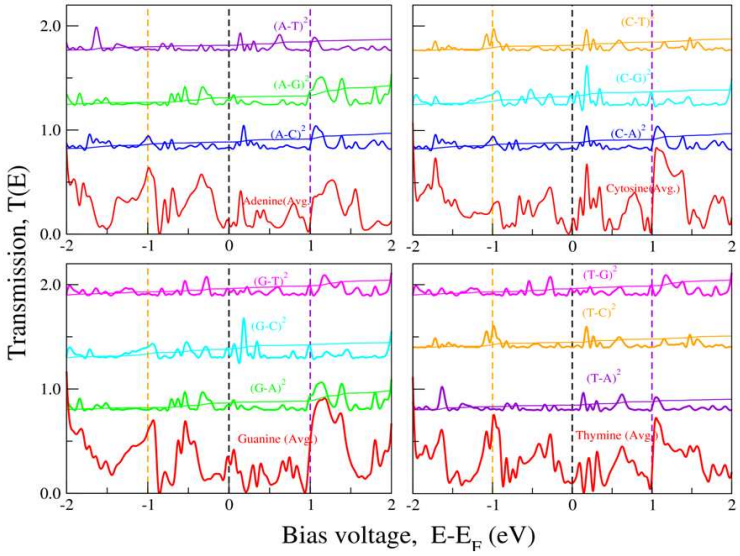

Figure 6.6: Difference curve of the average conductance of isolated DNA bases inside nanopore. Average is taken over angular configuration. **(a)** Adenine, **(b)** Cytosine, **(c)** Guanine, and **(d)** Thymine. The fermi energy is at 0 eV and difference curve shows distinguishing features for each of the DNA bases. the solid curve on each difference curve shows the integrated conductance or current.

In our calculation we have taken random angular orientation of the isolated bases inside the pore, and calculate the average transmission. The transmission dI/dV and its first derivative d^2I/dV^2 show identifiable features near zero volt for each of these bases as shown in Fig. 6.6 and Fig. 6.7. Fig. 6.6 shows the differential curves between A, C, G, and T.

Our calculations are carried out for the configuration averaged transmission currents and their derivatives with respect to the voltage. This is in contrast with the flat orientation of DNA nucleotides inside the pore as reported by Nelson*et al.* [136]. Here we take the diameter of the punctured hole on graphene as 15 $\AA$, and the carbon atoms inside the pore are not capped with Hydrogen. Hydrogen capping and the size of the nanpores can affect signal significantly, and thus call for a more systematic study. As we see in Fig. 6.6, our theoretical results are not completely free from noise. The proposal for better noise reduction techniques along with a more convenient device geometry is currently under progress and will be carried as a future direction of this project.

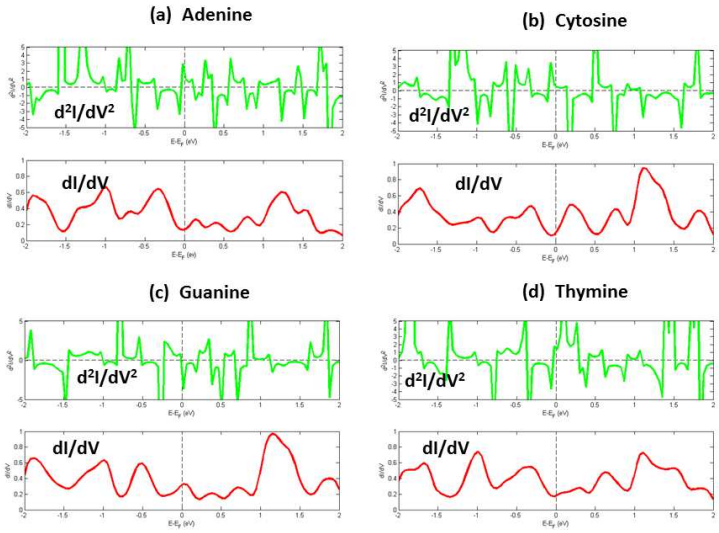

Figure 6.7: Average conductance dI/dV (solid red) and d^2I/dV^2 (solid green) of **a** Adenine, **a** Cytosine, **a** Guanine, and **a** Thymine through a graphene nanopore. Vertical dashed line is at the Fermi energy at 0 eV. Dominant features near Fermi energy in d^2/dV^2 distinguishes DNA bases passing through the nano-pore.

6.3 Conclusion

In conclusion, we propose the use of graphene as a deposition substrate for macromolecular sequencing. Both the Dirac linear dispersion of electronic states in graphene and its robust mechanical properties serve to make it a superior substrate compared to metals. We have calculated the tunneling conductance and LDOS for the specific case of single DNA bases at various orientations on the surface, and shown that the different nucleotides have significantly different LDOS peaks (fingerprints), allowing differentiation via local tunneling conductance. The calculated nitrogen atom LDOS for A,T,C, and G bases show distinct peaks that vary depending on configuration. We find that Guanine provides the largest peak at a negative bias at -1.3 eV, i.e., a slightly higher energy than guanine on copper [117]. Nonetheless, peaks for the other bases at higher energies have features at positive and negative STM bias, and provide fingerprints that allow unique identification. The calculated LDOS fingerprints can help guide STS as an approach to identify DNA bases, and likely other biomolecules on graphene surfaces.

Chapter 7

CONCLUSION

Studying the x-ray spectroscopy of correlated systems within RSGF framework and Hubbard model has been the primary focus of this thesis. Three different developments in this direction are discussed in chapters 3, 4, and 5. Many spectral features near the Fermi energy call for theoretical development beyond the single particle approximation. This is equally true for the conventional DFT and Green's function based approaches. To achieve a computationally cheap and efficient scheme, one often relies on some combination of model Hamiltonian and first-principle approaches. Chapter 3 is primarily dedicated to the implementation of a rotationally invariant LDA+U in the first-principles RSGF code FEFF. A combination of doping dependent single band Hubbard model based self energy and RSGF approach is discussed in chapter 4. Chapter 5 discusses charge transfer satellites present in the x-ray spectra of many strongly correlated systems. Such satellites can be incorporated in a spectral function by the Lee-Hedin model analogous to the Hubbard model. Finally, an additional chapter on the electronic structures of DNA-graphene hybrids stemmed out as a side project and some very interesting results eventually lead us to further investigate tunneling spectroscopy and electronic transport through graphene nano-pores from first principles. Our effort in this direction is presented in chapter 6.

Chapter 3 focuses on our effort to incorporate strong correlation in the real-space multiple scattering code FEFF in order to study the x-ray spectroscopy of Mott-Hubbard insulators. For implementation, we followed Anisimov's prescription of LDA+U and modified our code to adapt a rotationally invariant formalism. Our approach also builds in a model GW many-pole self-energy. The Hubbard parameter U can be fitt with the gap from experiments or can be calculated within the existing capability of the RSGF code with the constrained RPA method. Both the static limit of the Hubbard model and the energy-dependent many-pole self-energy effects are incorporated in an effective self-energy correction $\Delta\Sigma^U$. This effort leads to an RSGF/$\Delta\Sigma^U$ approach for an efficient way to study the x-ray spectra of complex correlated materials. Being a real-space based approach, it is

advantageous for aperiodic systems since it does not rely on symmetry or periodicity. We have tested our method on several correlated systems and found reasonable agreement for the observed experimental band gap as well as the XAS and XES of MnO and NiO. The less quantitative agreement for complex high-T_c cuprate LSCO suggests a more comprehensive treatment of superconducting and pseudo-gap physics that incorporates doping dependence in the strong-correlation regime. Overall the presented work and results in chapter 3 explains the key features of the excited-state electronic structure and spectra of many strongly correlated systems and in particular the correlation gap.

In chapter 4 we present our approach to explain the doping dependent spectral features in the over doped high-T_c LSCO. In this chapter we have carried out calculations of the O K-edge XANES of LSCO over the hole doping range x=0.20 to x=0.30. A doping dependent single-band Hubbard model based self-energy was derived by Bansil Group at the Northeastern University. This self-energy correction due to strong electron correlations was then incorporated into our RSGF code FEFF. Good agreement is found between the theoretical and experimental doping evolution of the XANES in overdoped LSCO.

Chapter 5 is dedicated to the charge transfer excitations and the related 'shake down/up' satellites present in the x-ray spectroscopy of many strongly correlated systems including the high-T_c cuprates. Such satellites were incorporated in our RSGF calculation by convoluting with a spectral function constructed from Lee-Hedin's charge transfer model. This model, which is closely analogous to the Hubbard model, is parameter dependent in its current form. Incorporating this model with first-principles calculation of Cu K-edge XANES of LSCO and NCCO was found to yield good agreement with experiment.

The above three chapters thus discuss the development of theoretical tools for x-ray spectroscopy of complex systems. With the emergence of newer and more exciting materials, there is a growing need for a better understanding of the long standing problem of strong correlation. The primary motivation of this thesis is to contribute to such efforts by extending many-body techniques of the excited state electronic structure code FEFF.

As a secondary goal and a subtopic of this thesis, we also focus on the electronic structure calculations of DNA graphene hybrids. A first-principles study of DNA bases and graphene is presented in chapter 6. Based on our ground-state electronic structure calculation we propose the use of graphene as a deposition substrate for macromolecular sequencing. We have calculated the

tunneling conductance and local density of states (LDOS) for the specific case of single DNA bases at various orientations on the surface and shown that the different nucleotides have significantly different LDOS peaks, allowing differentiations via local tunneling conductance. The calculated LDOS fingerprints can help guide STS as an approach to identify DNA bases and likely other biomolecules on graphene surfaces. Using Landauer-Buttiker formalism as implemented in the Trans-Siesta and ATK code, we have also calculated the transmission current through a graphene nano-ribbon as the DNA bases pass through a nano-pore. Our calculated transmittance and its first derivative shows distinctive features in the transverse current around Fermi energy based on the type of DNA base passing through the pore and thus provides guideline for similar experimental set up for DNA sequencing. Despite the large noise-to-signal ratio in these calculations such first-principles approaches are highly desirable for providing efficient and cheaper guidelines in order to design next generation nano-pore sequencing device.

7.0.1 Future Goals

For the immediate future our goals regarding the work presented in this thesis are:

- **Extension of LDA+*U***

  Our implementation of LDA+*U* in FEFF9 code is currently limited to *d* electron systems and K-edge x-ray spectroscopy. As more experimental data on f electron systems are becoming available, there is an increasing demand on the calculation ability of excited state spectroscopy in these systems. The extension from *d* to f systems is practical and straightforward within the scope of our RSGF code FEFF9. Another natural extension of our current implementation will be from K to L2/L3 and higher edges.

- **Implementation of charge-Transfer Satellites in FEFF**

  In our current effort we have constructed the charge transfer spectral function taking the analytical expression of the first-order perturbation from the Lee-Hedin model. A complete construction is possible using the transition matrix element and potentials which are calcu-

lated within the scope of FEFF9. An effort to do this is currently underway.

- **Transmission Current of graphene nano-pore for DNA fingerprinting** Our calculation of transmission current through graphene nano-ribbon is currently in an early stage with a simple device geometry. We believe that a construction of a more realistic device with practical noise reduction techniques, the calculation of transport current will provide a useful theoretical tool in guiding the DNA sequencing nanopore experiments. As an immediate goal we want to proceed with an updated device geometry and fine tune our calculation to enhance the theoretical ‘signal to noise’ ratio.

BIBLIOGRAPHY

[1] H. Jiang, R. I. Gomez-Abal, P. Rinke, and M. Scheffler, Phys. Rev. B **82**, 045108 (2010).

[2] J. de Boer and E. Verwey, Proc.Phys.Soc. **A49**, 59 (1937).

[3] N. F. Mott, Proc. Phys. Soc. **47**, 571 (1935).

[4] N. F. Mott, Proc. Phys. Soc. **A62**, 416 (1949).

[5] L. H. Thomas, Mathematical Proceedings of the Cambridge Philosophical Society **23**, 542 (1926).

[6] J. C. Slater, Phys. Rev. **49**, 537 (1936).

[7] J. C. Slater, Phys. Rev. **82**, 538 (1951).

[8] J. Hubbard, Proc. R. Soc. Lond. **A227**, 237 (1964).

[9] J. Hubbard, Proc. R. Soc. Lond. **281**, 401 (1964).

[10] L. Hedin and S. Lundqvist, Solid State Phys. **23**, 1 (1969).

[11] L. Hedin, Journal of Physics: Condensed Matter **11**, R489 (1999).

[12] V. I. Anisimov, J. Zaanen, and O. K. Andersen, Phys. Rev. B **44**, 943 (1991).

[13] V. I. Anisimov, I. V. Solovyev, M. A. Korotin, M. T. Czyżyk, and G. A. Sawatzky, Phys. Rev. B **48**, 16929 (1993).

[14] J. P. Perdew and A. Zunger, Phys. Rev. B **23**, 5048 (1981).

[15] B. G. Janesko, T. M. Henderson, and G. E. Scuseria, Phys. Chem. Chem. Phys. **11**, 443 (2009).

[16] E. Runge and E. K. U. Gross, Phys. Rev. Lett. **52**, 997 (1984).

[17] C. D. Sherrill and H. F. Schaefer, Advances in Quantum Chemistry **34**, 143 (1999).

[18] A. I. Lichtenstein, M. I. Katsnelson, and G. Kotliar, Phys. Rev. Lett. **87**, 067205 (2001).

[19] T. Das, R. S. Markiewicz, and A. Bansil (2008).

[20] J. D. Lee, O. Gunnarsson, and L. Hedin, Phys. Rev. B **60**, 8034 (1999).

[21] N. Kosugi, Y. Tokura, H. Takagi, and S. Uchida, Phys. Rev. B **41**, 131 (1990).

[22] T. Ahmed, T. Das, J. J. Kas, H. Lin, B. Barbiellini, F. D. Vila, R. S. Markiewicz, A. Bansil, and J. J. Rehr, Phys. Rev. B **83**, 115117 (2011).

[23] T. Ahmed, J. J. Kas, and J. J. Rehr, Phys. Rev. B **85**, 165123 (2012).

[24] L. Campbell, L. Hedin, J. J. Rehr, and W. Bardyszewski, Phys. Rev. B **65**, 064107 (2002).

[25] A. L. Fetter and J. D. Walecka, *Quantum Theory of Many-Particle Systems* (Dover, 2003), 3rd ed.

[26] C. Friedrich and A. Schindlmayr, many-Body Perturbation Theory: The GW Approximation, published in Computational Nanoscience: Do It Yourself!, J. Grotendorst, S. Bl′ugel, D. Marx (Eds.), John von Neumann Institute for Computing, J′ulich, NIC Series, Vol. 31, pp. 335-355 (2006).

[27] R. D. Mattuck, *A Guide to Feynman Diagrams in the Many-Body Problem* (Dover, 1974), 2nd ed.

[28] A. Gonis and W. H. Butler, *Multiple Scattering in Solids* (Springer-Verlag New York, Inc., 2000), 1st ed.

[29] A. Ankudinov and J. Rehr, Phys. Rev. B **62**, 2437 (2000).

[30] U. von Barth and L. Hedin, J. Phys. C: Solid State Phys. **5**, 1629 (1972).

[31] J. J. Rehr and R. C. Albers, Rev. Mod. Phys. **72**, 621 (2000).

[32] P. W. Anderson, Phys. Rev. **124**, 41 (1961).

[33] W. Kohn and L. J. Sham, Phys. Rev. **140**, A1133 (1965).

[34] P. Hohenberg and W. Kohn, Phys. Rev. **136**, B864 (1964).

[35] N. D. Mermin and H. Wagner, Phys. Rev. Lett. **17**, 1133 (1966).

[36] N. F. Mott, *Meta-Insulator Transition* (Taylor and Francis, 1990), 2nd ed.

[37] D. M. Ceperley and B. J. Alder, Phys. Rev. Lett. **45**, 566 (1980).

[38] A. Svane and O. Gunnarsson, Phys. Rev. Lett. **65**, 1148 (1990).

[39] M. Lüders, A. Ernst, M. Däne, Z. Szotek, A. Svane, D. Ködderitzsch, W. Hergert, B. L. Györffy, and W. M. Temmerman, Phys. Rev. B **71**, 205109 (2005).

[40] F. Aryasetiawan and O. Gunnarsson, Reports on Progress in Physics **61**, 237 (1998).

[41] A. Svane and O. Gunnarsson, Phys. Rev. B **37**, 9919 (1988).

[42] P. Limelette, A. Georges, D. Jerome, P. Wzietek, P. Metcalf, and J. M. Honig, Science **302**, 89 (2003).

[43] A. Altland and B. Simons, *Condensed Matter Field Theory* (Cambridge University Press, 2010), 2nd ed.

[44] R. S. Markiewicz, T. Das, and A. Bansil, Phys. Rev. B **82**, 224501 (2010).

[45] T. Das, R. S. Markiewicz, and A.Bansil, Phys. Rev. B **81**, 184515 (2010).

[46] T. Das, R. S. Markiewicz, and A.Bansil, Phys. Rev. B **81**, 174504 (2010).

[47] A. L. Ankudinov, Y. Takimoto, and J. J. Rehr, Phys. Rev. B **71**, 165110 (2005).

[48] F. Aryasetiawan, K. Karlsson, O. Jepsen, and U. Schönberger, Phys. Rev. B **74**, 125106 (2006).

[49] V. I. Anisimov, F. Aryasetiawan, and A. I. Lichtenstein, J. Phys.: Condens. Matter **9**, 767 (1997).

[50] G. Onida, L. Reining, and A. Rubio, Rev. Mod. Phys. **74**, 601 (2002).

[51] A. I. Liechtenstein, V. I. Anisimov, and J. Zaanen, Phys. Rev. B **52**, R5467 (1995).

[52] H. Jiang, R. I. Gomez-Abal, P. Rinke, and M. Scheffler, Phys. Rev. Lett. **102**, 126403 (2009).

[53] T. Das, R. S. Markiewicz, and A. Bansil, Phys. Rev. B **81**, 174504 (2010).

[54] R. S. Markiewicz, S. Sahrakorpi, and A. Bansil, Phys. Rev. B **76**, 174514 (2007).

[55] S. Basak, T. Das, H. Lin, J. Nieminen, M. Lindroos, R. S. Markiewicz, and A. Bansil, Phys. Rev. B **80**, 214520 (2009).

[56] O. Bengone, M. Alouani, P. Blöchl, and J. Hugel, Phys. Rev. B **62**, 16392 (2000).

[57] H. Ebert, A. Perlov, and S. Mankovsky, Solid State Communications **127**, 443 (2003).

[58] A. Juhin, F. de Groot, G. Vankó, M. Calandra, and C. Brouder, prb **81**, 115115 (2010).

[59] O. Gunnarsson, Phys. Rev. B **41**, 514 (1990).

[60] A. K. McMahan, R. M. Martin, and S. Satpathy, Phys. Rev. B **38**, 6650 (1988).

[61] M. S. Hybertsen, M. Schlüter, and N. E. Christensen, Phys. Rev. B **39**, 9028 (1989).

[62] I. V. Solovyev and M. Imada, Phys. Rev. B **71**, 045103 (2005).

[63] M. Cococcioni and S. de Gironcoli, Phys. Rev. B **71**, 035105 (2005).

[64] K. Nakamura, R. Arita, Y. Yoshimoto, and S. Tsuneyuki, Phys. Rev. B **74**, 235113 (2006).

[65] M. Springer and F. Aryasetiawan, Phys. Rev. B **57**, 4364 (1998).

[66] F. Aryasetiawan, M. Imada, A. Georges, G. Kotliar, S. Biermann, and A. I. Lichtenstein, Phys. Rev. B **70**, 195104 (2004).

[67] E. Z. Kurmaev, R. G. Wilks, A. Moewes, L. D. Finkelstein, S. N. Shamin, and J. Kuneš, Phys. Rev. B **77**, 165127 (2008).

[68] P. Krüger, Journal of Physics: Conference Series **190**, 012006 (2009).

[69] J. P. Perdew, R. G. Parr, M. Levy, and J. L. Balduz, Phys. Rev. Lett. **49**, 1691 (1982).

[70] K. Schönhammer, O. Gunnarsson, and R. M. Noack, Phys. Rev. B **52**, 2504 (1995).

[71] R. C. Albers, N. E. Christensen, and A. Svane, J. Phys.: Condens. Matter **21**, 343201 (2009).

[72] B. Fromme, *Electronic Structure of MnO, CoO, and NiO*, vol. 170 of *Springer Tracts in Modern Physics* (Springer Berlin Heidelberg, 2001).

[73] S. Liu and W. Langenaeker, Theoretical Chemistry Accounts: Theory, Computation, and Modeling (Theoretica Chimica Acta) **110**, 338 (2003).

[74] M. J. Stott and E. Zaremba, Phys. Rev. A **21**, 12 (1980).

[75] A. L. Ankudinov, Y. Takimoto, and J. J. Rehr, prb **71**, 165110 (2005).

[76] J. J. Rehr, J. J. Kas, F. D. Vila, M. P. Prange, and K. Jorissen, Phys. Chem. Chem. Phys. **12**, 5503 (2010).

[77] W. von der Linden and P. Horsch, Phys. Rev. B **37**, 8351 (1988).

[78] J. J. Kas, A. P. Sorini, M. P. Prange, L. W. Cambell, J. A. Soininen, and J. J. Rehr, Phys. Rev. B **76**, 195116 (pages 10) (2007).

[79] A. Georges, AIP Conference Proceedings **715**, 3 (2004).

[80] A. E. Berkowitz and K. Takano, Journal of Magnetism and Magnetic Materials **200**, 552 (1999).

[81] B. Morosin, Phys. Rev. B **1**, 236 (1970).

[82] J. Orenstein, G. A. Thomas, D. H. Rapkine, C. G. Bethea, B. F. Levine, R. J. Cava, E. A. Rietman, and D. W. Johnson, Phys. Rev. B **36**, 729 (1987).

[83] K. Nakahigashi, N. Fukuoka, and Y. Shimomura, J. Phys. Soc. Jpn. **38**, 1634 (1975).

[84] H. Kondoh and T. Takeda, J. Phys. Soc. Jpn. **19**, 2041 (1964).

[85] L. V. Dobysheva, P. L. Potapov, and D. Schryvers, Phys. Rev. B **69**, 184404 (2004).

[86] H. Kurata, E. Lefèvre, C. Colliex, and R. Brydson, Phys. Rev. B **47**, 13763 (1993).

[87] T. Kotani and M. van Schilfgaarde, J. Phys.: Condens. Matter **20**, 295214 (2008).

[88] D. C. Peets, D. G. Hawthorn, K. M. Shen, Y.-J. Kim, D. S. Ellis, H. Zhang, S. Komiya, Y. Ando, G. A. Sawatzky, R. Liang, et al., Phys. Rev. Lett. **103**, 087402 (2009).

[89] R. Markiewicz, T. Das, and A. Bansil, unpublished.

[90] R. S. Markiewicz and A. Bansil, Phys. Rev. Lett. **96**, 107005 (2006).

[91] J. J. Rehr, J. J. Kas, M. P. Prange, A. P. Sorini, Y. Takimoto, and F. Vila, Comptes Rendus Physique **10**, 548 (2009).

[92] S. Basak, T. Das, H. Lin, R. S. Markiewicz, and A.Bansil (2010), march meeting (APS).

[93] N. Nücker, J. Fink, J. C. Fuggle, P. J. Durham, and W. M. Temmerman, Phys. Rev. B **37**, 5158 (1988).

[94] M. Klauda, J. Markl, C. Fink, P. Lunz, G. Saemann-Ischenko, F. Rau, K.-J. Range, R. Seemann, and R. L. Johnson, Phys. Rev. B **48**, 1217 (1993).

[95] H. Romberg, M. Alexander, N. Nücker, P. Adelmann, and J. Fink, Phys. Rev. B **42**, 8768 (1990).

[96] J. J. Rehr and A. L. Ankudinov, Radiation Physics and Chemistry **70**, 453 (2004), ISSN 0969-806X, photoeffect: Theory and Experiment.

[97] J. A. Soininen, J. J. Rehr, and E. L. Shirley, Physica Scripta **T115**, 243 (2005).

[98] R. S. Markiewicz, S. Sahrakorpi, M. Lindroos, H. Lin, and A. Bansil, Phys. Rev. B **72**, 054519 (2005).

[99] E. Pellegrin, N. Nücker, J. Fink, S. L. Molodtsov, A. Gutiérrez, E. Navas, O. Strebel, Z. Hu, M. Domke, G. Kaindl, et al., Phys. Rev. B **47**, 3354 (1993).

[100] M. Braden, P. Schweiss, G. Heger, W. Reichardt, Z. Fisk, K. Gamayunov, I. Tanaka, and H. Kojima, Physica C: Superconductivity **223**, 396 (1994), ISSN 0921-4534.

[101] C. T. Chen, F. Sette, Y. Ma, M. S. Hybertsen, E. B. Stechel, W. M. C. Foulkes, M. Schulter, S.-W. Cheong, A. S. Cooper, L. W. Rupp, et al., Phys. Rev. Lett. **66**, 104 (1991).

[102] A. Liebsch, Phys. Rev. B **81**, 235133 (2010).

[103] X. Wang, L. de' Medici, and A. J. Millis, Phys. Rev. B **81**, 094522 (2010).

[104] H. Eskes, M. B. J. Meinders, and G. A. Sawatzky, Phys. Rev. Lett. **67**, 1035 (1991).

[105] M. C. A. Comanac, L de Medici and A. J. Millis, Nature Physics **4**, 287 (2008).

[106] E. R. Mardis, Nature **470**, 198 (2011).

[107] M. Tichoniuk, M. Ligaj, and M. Filipiak, Sensors **8**, 2118 (2008), ISSN 1424-8220.

[108] V. Savolainen, R. S. Cowan, A. P. Vogler, G. K. Roderick, and R. Lane, Philosophical Transactions of the Royal Society B: Biological Sciences **360**, 1805 (2005).

[109] Z. Liu, J. T. Robinson, X. Sun, and H. Dai, Journal of the American Chemical Society **130**, 10876 (2008), pMID: 18661992.

[110] J. G. Lorenz, W. E. Jackson, J. C. Beck, and R. Hanner, Philosophical Transactions of the Royal Society B: Biological Sciences **360**, 1869 (2005).

[111] V. J. Cook, C. Y. Turenne, J. Wolfe, R. Pauls, and A. Kabani, J. Clin. Microbiol. **41**, 1010 (2003).

[112] M. Zwolak and M. Di Ventra, Nano Letters **5**, 421 (2005).

[113] J. Lagerqvist, M. Zwolak, and M. Di Ventra, Nano Letters **6**, 779 (2006).

[114] S. K. Min, W. Y. Kim, Y. Cho, and K. S. Kim, Nature NanoPY **6**, 162 (2011).

[115] D. A. Yarotski, S. V. Kilina, A. A. Talin, S. Tretiak, O. V. Prezhdo, A. V. Balatsky, and A. J. Taylor, Nano Letters **9**, 12 (2009).

[116] G. H. Seong, T. Niimi, Y. Yanagida, E. Kobatake, and M. Aizawa, Analytical Chemistry **72**, 1288 (2000), pMID: 10740872.

[117] H. Tanaka and T. Kawai, Nat Nano **4**, 518 (2009).

[118] C. Clemmer and T. Beebe, Science **251**, 640 (1991).

[119] S. Kilina, S. Tretiak, D. A. Yarotski, J.-X. Zhu, N. Modine, A. Taylor, and A. V. Balatsky, The Journal of Physical Chemistry C **111**, 14541 (2007).

[120] A. H. Castro Neto, F. Guinea, N. M. R. Peres, K. S. Novoselov, and A. K. Geim, Rev. Mod. Phys. **81**, 109 (2009).

[121] A. Grüneis, C. Attaccalite, A. Rubio, D. V. Vyalikh, S. L. Molodtsov, J. Fink, R. Follath, W. Eberhardt, B. Büchner, and T. Pichler, Phys. Rev. B **80**, 075431 (2009).

[122] S. Akca, A. Foroughi, D. Frochtzwajg, and H. W. C. Postma, PLoS ONE **6**, e18442 (2011).

[123] A. K. Geim and K. S. Novoselov, Nat Mater **6**, 183 (2007).

[124] K. S. Novoselov, A. K. Geim, S. V. Morozov, D. Jiang, Y. Zhang, S. V. Dubonos, I. V. Grigorieva, and A. A. Firsov, Science **306**, 666 (2004).

[125] Q. Su, S. Pang, V. Alijani, C. Li, X. Feng, and K. Mllen, Advanced Materials **21**, 3191 (2009), ISSN 1521-4095.

[126] G. Henkelman and H. Jónsson, Phys. Rev. Lett. **86**, 664 (2001).

[127] P. Jurecka, J. Sponer, J. Cerny, and P. Hobza, Phys. Chem. Chem. Phys. **8**, 1985 (2006).

[128] D. E. Vanpoucke and G. Brocks, Physical Review B: Condensed matter and materials physics **77**, 241308 (2008).

[129] D. A. Siegel, C.-H. Park, C. Hwang, J. Deslippe, A. V. Fedorov, S. G. Louie, and A. Lanzara, Proceedings of the National Academy of Sciences (2011).

[130] G. Kresse and J. Furthmüller, Phys. Rev. B **54**, 11169 (1996).

[131] D. Vanderbilt, Phys. Rev. B **41**, 7892 (1990).

[132] D. Branton, D. W. Deamer, A. Marziali, H. Bayley, S. A. Benner, T. Butler, M. Di Ventra, S. Garaj, A. Hibbs, X. Huang, et al., Nature Biotechnology **26**, 1146 (2008).

[133] E. A. Manrao, I. M. Derrington, M. Pavlenok, M. Niederweis, and J. H. Gundlach, PLoS ONE **6**, e25723 (2011).

[134] D. Sanchez-Portal, P. Ordejin, E. Artacho, and J. M. Soler, International Journal of Quantum Chemistry **65**, 453 (1997), ISSN 1097-461X.

[135] P. Ordejón, E. Artacho, and J. M. Soler, Phys. Rev. B **53**, R10441 (1996).

[136] S. V. Kilina, C. F. Craig, D. S. Kilin, and O. V. Prezhdo, J. Phys. Chem, C **submitted**, October 2006 (2007).

[137] J. Tersoff and D. R. Hamann, Phys. Rev. B **31**, 805 (1985).

Appendix A

LDA+U EXTENSION OF FEFF: NEW AND MODIFIED CODE

In this appendix we describe the parts of the FEFF9 code which we modified to incorporate rotationally invariant Hubbard model. Here we list all the new routines and briefly describe their functions. We also describe the new input card HUBBARD in the feff.inp file as well as all the new outputs files. A few simple flow charts are also added to have better understanding of how the logic of the program flows. LDA+U was implemented by modifying all routines in LDOS module and hence renamed as LDOS-HUBB as an additional module in FEFF9.

A.1 Input: feff.inp

This implementation was performed following the 'minimal card usage policy'. Which means in 'feff.inp' file one only needs HUBBARD card along with LDOS card. HUBBARD card uses three parameters namely $< U >$, $< J >$, and $< fermi - shift >$. For parametric calculation these three values are real numbers. If one specify the first parameter as "cRPA" then constrained RPA calculation is performed, and $< U >$ is read from the output file called "crpa.dat".

- $< U >$ The value of U can be a real value or string "CRPA". In the latter case the CRPA program will run and U will be read from 'crpa.dat' file.

- $< J >$ At the current implementation level, exchange parameter J is not calculated. For most systems, this value doesn't vary a lot and stay within 0.6 to 1.0.

- $< fermi - shift >$ This option is just to add or subtract a small correction term from the Fermi energy. FEFF calculated Fermi energy is often not highly accurate while to correctly split the upper and lower Hubbard band one needs to know E_F very precisely. Thus this parameter is just to give a little more control to make any necessary correction to the Fermi energy.

A.2 Final output files

Once the Hubbard calculation is done the output files are:

- **lmdos0x.dat** - This file contains 33 columns. The first column is photoelectron energy in eV. From 2nd to 17th columns are spin up density of states for one *s*, three *p*, five *d* and seven *f* orbitals. From 18th to 33rd columns are density of states for similar orbitals but for down spin. 'x' stands for the particular atom or potential type, e.g., x = 0 for central atom

- **hubbard0x.dat** - This file contains diagonalized (α basis) spin-orbital occupancy $n_{l\alpha\sigma}$ and corresponding Hubbard correction potential $V_{l\alpha\sigma}$ for all l, α, and σ values.

A.3 Intermediate output files

There are a few other output files which are created and read at the various stages of Hubbard program run. These are:

- **hubbard.inp** - After feff.inp is read by FEFF's "rdinp" program, the file 'hubbard.inp' is created if it finds HUBBARD and LDOS cards simultaneously. This file only contains the values for "*U*" (parametric or CRPA generated), "*J*", and "fermi_shift".

- **transf.dat** - This file contains the unitary matrix which is used to diagonalize $n_{lmm'\sigma}$.

- **Invtransf.dat** - This file contains the inverse of the unitary matrix which is used to diagonalize $n_{lmm'\sigma}$.

- **gtr_off.dat** - This file contains the off-diagonal terms for gg matrix which is returned from 'fms' routine insidefms_pack.

- **gtr_m.dat** - This file contains the *m* dependent terms of the gg matrix which is returned from 'fms' routine insidefms_pack.

- **aphase_dos0x.dat** - 'x' stands for atom/pontetial type. This file contains the *m* dependent phases which is written in rhol_h.f90 and read in fmsdos_h.f90.

- **aphase_up.dat** - This file contains the l, m, and $\sigma = up$ dependent phase written in 'XSPH/phase.f90' and read in 'FMS/fmstot.f90'.

- **aphase_down.dat** - Same as above but for $\sigma = down$.

A.4 Modified routines in FEFF90 for LDA+U

A.4.1 RDINP

- **rdinp.f90**

  This routine is modified to read HUBBARD card (if 'itoken' is returned to be 98) and also reads parameters U, J and fermi_shift. It assigns 2 to mldos_hubb when HUBBARD card is present or else mldos_hubb = 1 and only regular LDOS is executed.

A.4.2 COMMON

- **itoken.f90**

  This modified routine reads 'feff.inp' and assigns itoken = 98 if HUBBARD card is present. 'itoken' is later read by 'rdinp.f90' routine.

- **rdxsph.f90**

A.4.3 LDOS_HUBB

- **ldos_h.f90**

  This is a new routine written following the existing ldos.f90 in FEFF90. This is run instead of ldos.f90 if mldos_hubb=2. The only other difference between these two routines is ldos_h.f90 reads spinph or the spin polarization specified in 'feff.inp' and calculates von Barth Hedin potential for both spins (up and down). Then ldossub_h routine is called. Dimensions of some of the variables are also extended accordingly to accommodate both spin states.

- **ldossub_h.f90**

  This routine is equivalent to original ldossub.f90 with few changes. This routine calls rhol_h routine but for both spins. This also calls 'fmsdos_h.f90' and 'ff2rho_h.f90'.

- **reldos_h.f90**

  This routine is equivalent to reldos.f90 but is modified to extend the dimension of some variables to accommodate both spins.

- **rhol_h.f90**

  This routine calculates 'dvovrg.f90' (Dirac solver) to calculate the components of dirac spinors and also calculate their phases both in "Vanilla" and "Hubbard" running stage.

- **fmsdos_h.f90**

  Now this is executed twice: without and with the Hubbard correction("Vanilla-FEFF" and "Hubbard-FEFF" as explained by the flow charts in the next section). In the first stage this routine calls 'fms' routine from 'FMS/fmspack.f90' but in the second stage it calls 'fms_h' in 'FMS/fmspack_h.f90' which returns 'gg_m.bin'.

- **ff2rho_h.f90**

  A handful of important tasks are done in this routine. This routine is called from ldossub_h.f90 at the end of the first stage ("Vanilla-FEFF"), and the main task of this routine is not only to print 'ldos0x.dat' (angular momentum l projected DOS) and 'lmdos0x.dat' (orbital and angular momentum projected DOS), but also using diagonalized spin-orbital occupation $n_{l\alpha\sigma}$, construct the Hubbard correction potential $V^{U}_{l\alpha\sigma}$. These results are then written in "habbard0x.dat" files which are read at the second stage of running ("Hubbard-FEFF')

A.4.4 FMS

- **fmspack_h.f90**

  This is a new additional routine which is primarily a modification of fmspack.f90 routine in FMS module. fmspack.f90 calculates t-matrix and free Green's function, and returns 'gg'.

- **gglu_h.f90**

  This program is an equivalent version of gglu.f90 for "Hubbard-FEFF" run. The only difference is it keeps track of the unitary transformation matrices.

A.4.5 MATH

- **seigen.f90**

  This routine is adapted from BLAS package and is able to diagonalize any finite symmetric matrix and provides the eigen values and eigen vectors. It contains the routine called SSYEV which was called from ff2rho_h.f90 in order to diagonalize $n_{lmm'\sigma}$. The eigen vectors are then used to construct the unitary transformation matrix.

A.4.6 LDOS

- **ldos.f90**

  This is a routine mostly used in "Vanilla-FEFF' running stage. There are two minor modifications in this routine. This s is executed only when mldos_hubb = 1 otherwise LDOS module will turn off all the routines from LDOS_HUBB module start to execute.

A.4.7 XSPH

- **phase.f90**

  In this routine the phases are calculated using the Hubbard corrected total potential.

A.5 Example input file

Here we give an example of feff.inp file with HUBBARD card.

A.6 Program running flow chart

In order to have a better understanding of how this is implemented in FEFF9, we present a few flow diagrams. For simplicity the diagram doesn't include all the detailed input, output or supporting files. Only the major input/outputs and functionalities are shown. As mentioned earlier the program runs in two stages (two major loops). In the first stage FEFF9 runs without Hubbard model but still within LDOS_HUBB module. We named this stage "Vanilla-FEFF"(see Fig.A-1). At the end of this stage one obtains the density matrix, and by integrating this one obtains diagonal and off-diagonal spin-orbital occupancies $n_{lmm'\sigma}$. This matrix is then diagonalized and one obtains occupation number $n_{l\alpha\sigma}$ in α basis. This new basis is assumed to correctly represent the true eigen

```
TITLE name:     NiO
TITLE refer1:   wyckoff 1,III,88

EDGE      K
S02       1.0

CONTROL   1      1     1     1     1      1

EXCHANGE  0  0.0  0

SCF       5.0

XANES     4.0
FMS        8.0000  0

HUBB   4.50 0.80  0.0

*         emin  emax   eimag
LDOS      -35    15     0.10

POTENTIALS
*    ipot   Z    element   l_scmt  l_fms   stoichiometry  spinph
       0    8      O         1       3       0.001        0
       1   28      Ni        2       3       4            2
       2    8      O         1       3       4            0

ATOMS                          * this list contains 461 atoms
*   x          y          z          ipot  tag           distance
   0.00000    0.00000    0.00000  1    Ni1           0.00000     0
   2.08420    0.00000    0.00000  0    O1            2.08420     1
```

Figure A.1:

states of the localized orbitals instead of the spherically symmetric $|m\rangle$ basis. The parametric or cRPA calculated U values along with $n_{l\alpha\sigma}$ are then used to construct Hubbard correction potential following Anisimov [12] prescription. This stage is described with the following flow chart in Fig.A-2. Finally the program runs in its second stage which we name as “Hubbard-FEFF” stage (see Fig.A-3). In each of these two stages the computation is looped over spin up and down. As a result the computation time can be estimated to be little more than four times the spin independent calculation of regular version of LDOS in FEFF9.

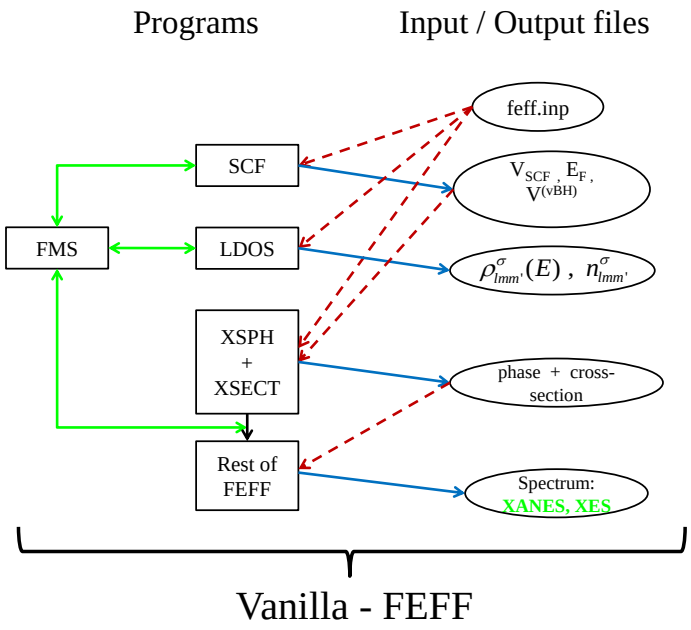

Figure A.2:

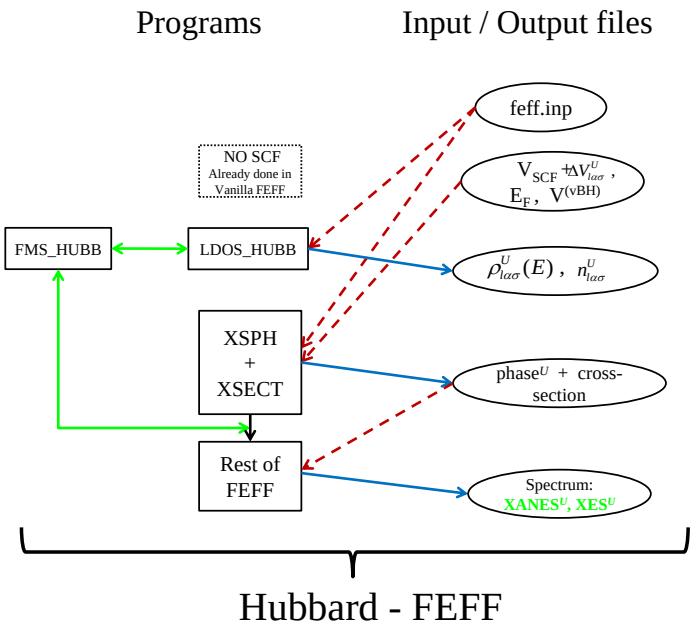

Figure A.3:

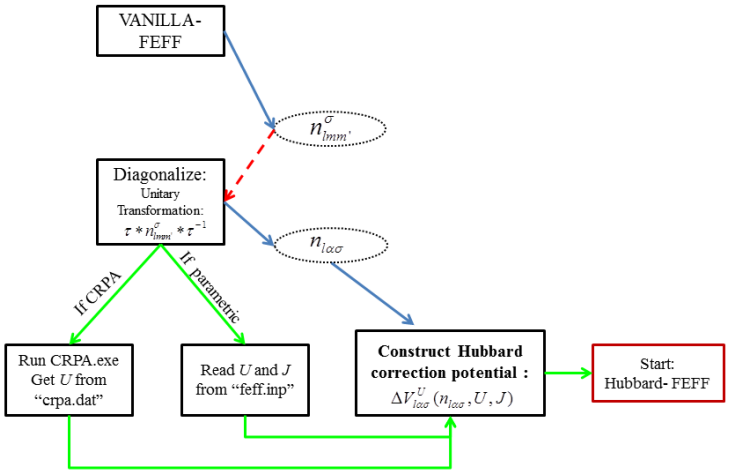
VANILLA-FEFF
$n^{\sigma}_{lmm'}$
Diagonalize:
Unitary Transformation:
$\tau * n^{\sigma}_{lmm'} * \tau^{-1}$
$n_{i\alpha\sigma}$
If CRPA
If parametric
Run CRPA.exe
Get U from "crpa.dat"
Read U and J from "feff.inp"
Construct Hubbard correction potential :
$\Delta V^{U}_{i\alpha\sigma}(n_{i\alpha\sigma}, U, J)$
Start: Hubbard- FEFF

Figure A.4:

Appendix B

SCANNING TUNNELING SPECTROSCOPY AND LOCAL DENSITY OF STATES

In the scanning tunneling spectroscopy (STS) one takes the advantage of scanning tunneling microscope (STM) in order to achieve tunneling current through the sample lying between a tip and a conducting substrate. By varying the bias voltage between the tip and substrate, one can probe the local electronic density of states (LDOS) of metals, semiconductors and thin insulators on a scale which has much higher precision than other currently available spectroscopies. Using Tersoff-Hamann theory [137], the tip is approximated to have featureless *s*-wave and the tunneling conductance is proportional to the LDOS $\rho(R_0, \varepsilon_F + V)$ at the tip position R_0 and energy $\varepsilon_F + V$,

$$\frac{dI}{dV}(V) \sim \rho(R_0, \varepsilon + V) = \sum_{i,k} |\psi_{ik}(R_0)|^2 \delta(\varepsilon_F + V - \varepsilon_{ik}) \tag{B.1}$$

where I is the current, ψ_{ik} and ε_{ik} are the i-th eigen state and eigen energy respectively, and k is the block wave vector index.

B.1 Interaction of Graphene and DNA base

In order to have a better assessment of the local electronic structure (LDOS) of the base atoms near the graphene plane, we performed a full geometry optimization of a supercell with approximately 75 atoms using VASP [14, 130, 131]-5.2 package. The binding energy between the bases and graphene is calculated using,

$$E_b = E_{total} - E_{iso-base} - E_{pure-graph}, \tag{B.2}$$

where E_b is the binding energy between the base and the graphene plane, E_{total} is the fully geometry optimized ground state energy of the graphene+base system, $E_{iso-base}$ and $E_{pure-graphene}$ are the geometry optimized total ground state energy of base molecule and graphene correspondingly. In Table-1 we also present the dependence of binding energy on the angular configuration of the base molecules on graphene surface.

Table B.1: Binding Energy (eV) between DNA bases and Graphene

Base	0^0	30^0	45^0	90^0
Adenine	-0.501	-0.202	-0.304	-0.292
Cytosine	-0.910	-0.843	-1.120	-0.930
Guanine	-0.678	-0.599	-0.510	-0.502
Thymine	-0.630	-0.473	-0.488	-0.451

By keeping similar geometric configurations of the bases but increasing the graphene size, we only assumed the order in binding energies to remain consistent and performed our self-consistent DFT calculations which are shown in the main text. The shifts in the LDOS peak as a function of angular orientation between the base and graphene planes are shown in Figure 6-3(a)-(d) of the main text.

B.2 3D Perspective

B.3 Calculation Method

Density functional theory (DFT) is well known for its accurate description of the ground state properties in the systems with mostly *s* and *p* electrons. In our calculations of the energy levels for isolated DNA-bases (Figure 6-2a), we used SIESTA-3.0 package [134, 135] which uses localized numerical basis sets and PW91 functional with LDA-PZ correlation. In the presence of the 2D graphene substrate, the plane-wave basis set becomes more preferable and we used VASP [14, 130, 131] code for the rest of our calculation. In all of our LDA calculations in this paper, core states are replaced by the standard ultrasoft Vanderbilt Pseudopotentials. For the pure graphene case in Figure 6-2b, we used $4 \times 4 \times 1$ k points in a supercell with dimension $12.3 \times 12.8 \times 16$ Å^3, where gamma-point self-consistent calculations were performed for the rest of the results presented in this paper. For the calculation presented in Figure 6-2b, we used a supercell with 880 atoms and dimension $43.0 \times 43.6 \times 30.0$ Å^3. For the results presented in Figure 6-3 for DNA bases on graphene

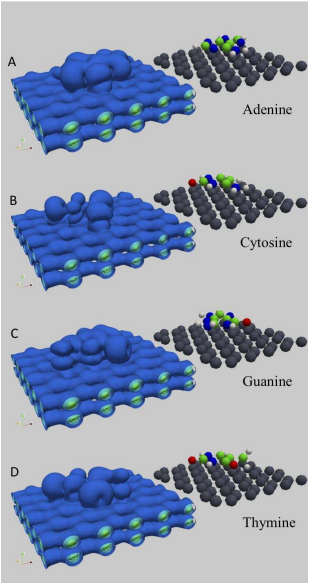

Figure B.1: Charge density and atomic structure for adenine (A), cytosine (B), guanine (C), and thymine (D) on graphene. The graphene carbons are in grey, while nucleobase carbons are in green.

only surface, the supercell($18.4 \times 18.6 \times 24.0$ Å^3) includes 128 atoms, and for the results with SiC substrate in Figure 6-4, the supercell ($14.4 \times 15.4 \times 30.0$ Å^3) contains 210 atoms.

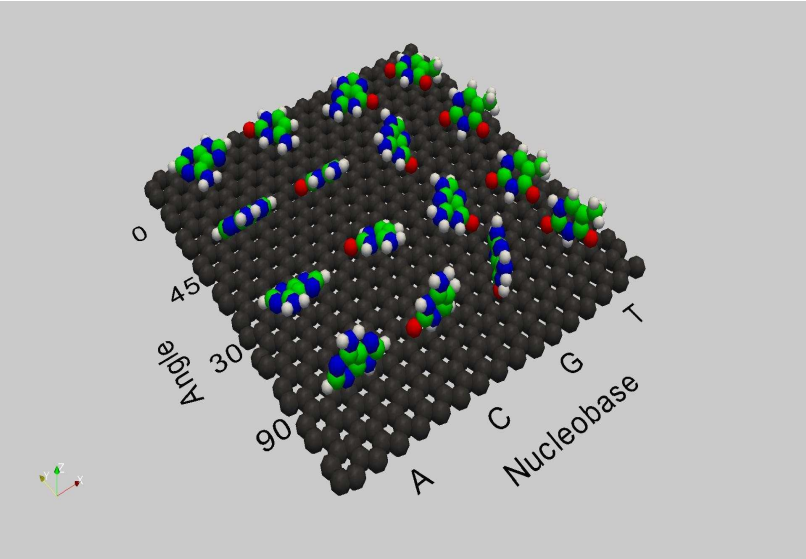

[Atomic structure of each nucleobase on graphene]

Figure B.2: Atomic structure of each nucleobase on graphene. The angle denotes the orientation of each nucleobase.

VITA

Towfiq Ahmed was born in Dhaka, Bangladesh and came to USA as an international student in 1998. He obtained BS in Physics and Math in 2002 and MS in Astrophysics in 2004 from University of Texas at Arlington. He joined the Ph.D. program at the University of Washington in 2004, and joined the condensed matter theory group of Prof. John J. Rehr in the summer of 2008. He received his Ph.D. in Physics in 2012.